RADIATION INDUCED MICROSTRUCTURAL EVOLUTION AND HARDENING INFLUENCED BY ALLOYING ELEMENTS IN FERRITIC IRON BASED BINARY MODEL ALLOYS

by

Patrick Henry Warren

A Dissertation

Submitted to the Faculty of Purdue University

In Partial Fulfillment of the Requirements for the degree of

Doctor of Philosophy

School of Materials Engineering

West Lafayette, Indiana

December 2022

THE PURDUE UNIVERSITY GRADUATE SCHOOL
STATEMENT OF COMMITTEE APPROVAL

Dr. Janelle Wharry, Chair
School of Materials Engineering

Dr. Anter El-Azab
School of Materials Engineering

Dr. Ernesto Marinero
School of Materials Engineering

Dr. Yaqiao Wu
Center for Advanced Energy Studies

Approved by:
Dr. David Bahr

To my wife and children,

Kelsey, Maddy, and Henry Warren, and the one on the way, AKA "Brown Holly" you make me laugh and smile every day.

You have shown me the meaning of life.

ACKNOWLEDGMENTS

I would like to start by saying thank you to Dr. Janelle Wharry. I consider myself extremely fortunate for having the opportunity to work with you. You have been fair and understanding throughout the entirety of my doctorate. You have continually offered guidance and support every step of the way. I considered quitting a few times along the way, but you pushed me and encouraged me. You taught me how to be a better researcher and communicator. I know that we will remain good friends as I continue on to the next step in my career.

I would like to thank my family. Mom and Dad, you have loved me and supported me unconditionally. you guys brought me up to work hard. Lee, George, and Candace, you are the best brothers and sister anyone could ask for. I love you guys and I couldn't have done this without you.

I would also like to thank my group members, Kayla, Priyam, Keyou, Amrita, Haozheng, Caleb and my brother George as well as the friends I have made while at Purdue. Every one of you were available when I needed you to help me collect and analyze data. We had good times and I know we will keep in touch and remain friends.

Most importantly I would like to thank my wife and children. Kelsey, you didn't flinch when I mentioned quitting my job at Micron and moving to Indiana to get my PhD. You said we're doing it and you have been supportive ever since. You have been an amazing mother to Henry and Maddy and you will be an amazing mother to our son on the way, who Maddy has named Brown Holly. They are all so lucky to have you as their mother. You have put up with me and loved me even when I was probably not the easiest to get along with. I love you even more every day. Henry and Maddy, you two have shown me the meaning of life. Before you three, I did not know this kind of happiness existed and I am so grateful.

I would like to thank the staff at the MaCS laboratory at CAES in Idaho Falls. Jeremy Bergener, Yu Lu, Yaqiao Wu, and Megha Dubey thank you for helping me learn to use the instruments at MaCS and always being available to answer questions. Thank you to Wei Ying Chen at Argonne National Lab for conducting my TEM *in situ* irradiation experiment.

Thank you to Dr. Ovidiu Toader, formerly of the Michigan Ion Beam Laboratory (MIBL) for conducting the *ex situ* ion irradiation, Dr. Wei Ying Chen of Argonne National Laboratory for conducting the *in situ* irradiation experiment, and Dr. Matthew Besser at Ames Laboratory

for help with alloy fabrication. This research was sponsored by the National Science Foundation award DMR-17-52636. The TEM *in situ* irradiation at the IVEM-Tandem Facility at Argonne National Laboratory was supported by the US DOE Office of Nuclear Energy through a Nuclear Science User Facilities (NSUF) rapid turnaround experiment.

TABLE OF CONTENTS

LIST OF TABLES

LIST OF FIGURES

NOMENCLATURE

A	Cross-sectional indenter area
α	Dispersed barrier strength factor
BCC	Body center cubic
BFSTEM	Brightfield scanning transmission electron microscopy
b	Burgers vector
c	Vickers indenter plastic zone radius
CAES	Center for Advanced Energy Studies
C_L	Concentration of defects
C_i	Interstitial concentration
C_v	Vacancy concentration
C_s	Sink concentration
DBTT	Ductile to brittle transition temperature
DPA	Displacements per atom
d	distance between obstacles
E	Ion energy
E_d	Displacement energy
E_I^m	Migration energy of SIA
ε	secondary atom knock-on energy charge unit
EBSD	Electron backscatter diffraction
EDM	Electrical discharge machining
EDS	Energy dispersive spectroscopy
FCC	face centered cubic
FIB	Focused ion beam
GB	Grain boundary
GIS	Gas injection system
γ	Energy transfer coefficient
Γ	Dislocation line tension
HCP	Hexagonal close packed
H_{Berk}	Berkovich Hardness
H_V	Vickers Hardness
h_c	Contact depth
I	Ion flux
IMCL	Irradiated Materials Characterization Laboratory
INL	Idaho National Laboratory
IVEM	Intermediate Voltage Electron Microscope
k	Boltzmann's constant
K_0	Defect production rate
K_{is}	Interstitial-sink reaction rate

K_{iv}	Vacancy-interstitial recombination rate
K_{is}	Vacancy-sink reaction rate
K-P	Kinchin-Pease model
l	Distance between obstacles
λ	Angle between applied stress and the slip direction
M	Mass of the target atom
M_i	Mass of incident ion
M_I	Mobility of SIAs
M_T	Taylor factor
μ	Shear modulus
N	Number density
N_{ob}	Obstacle number density
Ω_{sf}	Volume size factor of the interstitial atom
Ω_A	Atomic volume of the solvent
$\frac{\partial \Omega}{\partial c}$	Change in atomic volume of the solvent atom
Ω_B^*	Atomic volume of the substitutional atom
Ω_A	Atomic volume of the solvent atom
P	Production rate
P_{max}	Maximum indenter load
ϕ	Angle between the applied stress and the slip plane normal
RED	Radiation Enhanced Diffusion
RIS	Radiation induced segregation
R	Half distance between obstacles
R_{core}	Indentation core radius
r_c	Dislocation core radius
SAED	Selected area diffraction
SEM	Scanning electron microscopy
SFE	Stacking fault energy
SIA	Self-interstitial atom
STEM	Scanning transmission electron microscopy
σ	Applied stress
σ_s	Shear stress
σ_y	Yield stress
$\sigma(E,T)$	Collision cross section
$\Delta\sigma_y$	Dispersed barrier strengthening
TEM	Transmission electron microscopy
T	Temperature
τ_R	Resolved shear stress
ν	Lattice vibrational frequency
$\nu(T)$	Displacement function

ZA	Zone axis
Z_1	Incident ion atomic number
Z_2	Target atomic number
z_{ys}	Berkovich indenter plastic zone radius

ABSTRACT

The objective of this study is to evaluate the radiation induced microstructural and mechanical differences influenced by alloying elements including phosphorus, chromium, and nitrogen and crystal orientation in iron-based binary alloys. Fe-4.5at%P, Fe-9.5at%Cr, and Fe-2.3at%N binary model alloys were irradiated with 4.4 MeV Fe^{++} ions at 370 °C to 8.5 displacements per atom (DPA). Transmission electron microscopy (TEM) characterization including brightfield scanning electron microscopy (BFSTEM), diffraction, and TEM *in situ* irradiation, energy dispersive spectroscopy (EDS) compositional analysis, and nanoindentation were used to evaluate the radiation induced microstructural evolution and mechanical responses in these model alloys. Microstructure is of particular interest in irradiated nuclear structural materials because it plays an integral role in the mechanical integrity of these materials. Radiation induced defects present obstacles to dislocation motion and thus lead to hardening and embrittlement. P is highly undersized and forms a strong covalent bond with Fe which progresses to an Fe_3P beta phase in BCC iron when the solubility limit is reached. The covalent nature of the bonding as well as the smaller atomic volume of P leads to enhanced radiation induced defect nucleation, phosphorus segregation, and radiation induced precipitation. The high density of defects in the Fe-P alloy contributed to enhanced hardening of the irradiated Fe-P alloy in comparison to the Fe-Cr and Fe-N alloys. The density of these defects and depth of the ion irradiated damaged layer and thus the mechanical response is also heavily dependent on orientation and is made evident by nanoindentation and indentation cross section BFSTEM imaging.

1. INTRODUCTION

Generation IV nuclear reactors are currently being developed to meet global energy needs, but challenges associated with radiation damage of the reactor core structural materials are exacerbated by the extreme environments in these reactor cores. Ferritic iron alloys are particularly attractive candidate materials for nuclear structural applications in generation IV reactors because of their enhanced thermal properties such as high thermal conductivity and low thermal expansion. Furthermore, these alloys have enhanced swelling resistance, and reduced creep at elevated temperature [1–5], however these alloys become brittle under irradiation even at low damage levels [6].

It is well established that the radiation imparted on these alloys produces the accumulation of point defects that eventually form higher order defects as the irradiation damage increases. The dispersed barrier model describes how the microstructure of a material relates to the yield strength. This model suggests that the yield strength of a material increases with an increase in the defect density because as the density of defects increases, dislocations have more obstacles to overcome. In addition to defect density, defect type also plays an important role in the degree of hardening because the obstacle strength depends on the defect type. Thus, the irradiation induced microstructural evolution and the resulting mechanical response are of particular importance in the qualification of these alloys for next generation nuclear reactor structural purposes[7,8].

The improved radiation resistance of these alloys can be achieved through the addition of alloying elements and the optimization of alloy composition, however, may also have detrimental effects when not controlled. For instance, solutes have been shown to provide increased self-interstitial atom (SIA) trapping which increases the sink density in the alloy. The increased sink density may increase point defect recombination and reduce or prevent the growth of radiation induced defects such as dislocation loops, voids, and precipitates which can improve the radiation tolerance of the alloy, however this increased trapping capability may also lead to enhanced nucleation of defects, a higher defect density, and increased hardening and embrittlement [9–11]. Furthermore, solute addition may lead to radiation induced segregation (RIS) and the eventual formation of radiation induced precipitates [7,12,13]. The extent of these

effects is influenced by bond type and solute misfit therefore, solute selection is critical in improving the radiation tolerance of these alloys.

Chromium is used in ferritic alloys because of the improved resistance to void swelling and corrosion however, irradiation induced α' formation can occur when chromium content is not optimized [3,14–17]. Nitrogen is an element, often present as an impurity, that has shown mixed results. Studies have shown irradiation induced nitride formation and increased dislocation loop density which resulted in in the embrittlement of the alloys [18,19]. Other studies have shown a reduction in embrittlement and void swelling as a result of increased nitrogen content [20–22]. Phosphorus is another solute element that has been investigated in ferritic and nickel based alloys and has shown both positive and negative effects. P has been shown to reduce void swelling, dislocation loop growth, and secondary phase formation while other studies have demonstrated increased phosphide formation, increased defect density, and increased embrittlement with the presence of P [23–27]. The evaluation of these irradiation microstructures requires the availability of irradiated material. The use of neutron irradiated material presents several challenges. Months or years are required to produce high dpa neutron irradiated samples. Furthermore, neutron irradiated samples require special safety and handling protocols since they are radioactive and there is a limited number of facilities capable of handling these radioactive samples. Alternatively, ion irradiation produces high dpa samples in several hours instead of several months or years and does not require special handling or special facility capabilities. These advantages make ion irradiation an attractive alternative to neutron irradiation. Unfortunately, there are many challenges associated with ion irradiation as well. Ions have a large interaction cross section and only penetrate hundreds of nanometers to a few microns into the surface of the sample. Targeting this small region of interest for experimentation is difficult. Furthermore, the damage profile changes rapidly with depth resulting in a varying microstructure over hundreds of nanometers or less. This rapidly changing microstructure may make evaluating microstructure as it relates to dpa difficult.

The mechanical evaluation of a shallow ion irradiated layer which extends hundreds of nm to a few um into the surface of a sample requires a method capable of targeting small regions of interest with high load and displacement resolution. Nanoindentation has the capability to target small regions of interest with load and displacement resolution down to 1 nN and 100 nm respectively making it a powerful tool for evaluating the mechanical response in these thin ion

irradiated regions. TEM cross section imaging has been used in several studies along with nanoindentation to observe underlying deformation mechanisms [28–31]. This dissertation will investigate the influence of alloying elements; P, N, and Cr on the irradiation induced microstructure, irradiation induced mechanical responses, and the underlying fundamental deformation mechanisms in α iron binary model alloys.

2. BACKGROUND

2.1 Materials

2.1.1 Processing

The alloys used in this study, Fe – P, Fe – Cr, and Fe – N were plasma arc melted at AMES Laboratory Materials Processing center to incorporate alloying elements in high purity and to have greater control over the resulting microstructure. After arc melting the alloy ingots were cut down to 2mm x 2mm x 20 mm bars by wire electrical discharge machining (EDM). EDM is a highly precise machining method that involves the use of an electrical arc to cut a part into a desired shape [32–34].

2.1.2 Ferritic alloys

Ferritic alloys are commonly used as structural materials for a wide range of applications including vehicle frames and chassis, tanks, nuclear energy, and others. Alloying components such as carbon, chromium, aluminum, molybdenum and others have been used in these ferritic alloys to improve strength, corrosion resistance and radiation tolerance [35,36]. Ferritic alloys are iron-based alloys with a BCC crystal structure. The BCC crystal structure is a non-close packed crystal structure, so slip does not happen as easily. As such, these alloys tend to be stronger and less ductile than their austenitic counterparts. Furthermore, since the BCC slip systems are not close packed, some of them require thermal energy to be activated so these alloys behave ductile at high temperatures and brittle at low temperatures. The temperature at which these alloys transition from ductile to brittle behavior is the ductile to brittle transition temperature (DBTT). The DBTT in ferritic alloys increases under irradiation because of increased defect densities. The increased DBTT is a point of improvement in these alloys and the content of alloying elements have been used to mitigate this shift in DBTT [37–39]. These alloys also have low thermal expansion which make them ideal for applications which involve elevated operating temperatures and regular thermal cycling.

2.1.3 Iron – Phosphorus

Phosphorus is often present in a variety of alloys as an impurity however, it has also been used as an alloying element to produce desired effects such as high wear resistance in ferritic steels [40]. P has been investigated in a variety of alloys including Ni based alloys, austenitic Fe alloys, and ferritic Fe alloys and has shown both beneficial and detrimental effects. For instance, it is well known that P segregates quite easily to the grain boundaries (GBs) in many alloys and that this segregation can result in embrittlement, increased DBTT, and intergranular fracture but a specific cause has not been determined with several mechanisms of embrittlement at the grain boundaries suggested. One generally accepted mechanisms is decohesion by the directional bonding of the P atoms in the grain boundaries and [41–45]. However, it has also been reported that when content is optimized P can improve the cohesive properties of the grain boundaries in some alloys [46]. Other studies have reported the formation of phosphides in austenitic and ferritic steels which are also known to produce embrittlement. Both phosphide formation and grain boundary segregation can be exacerbated by RIS. The concept of RIS will be discussed in section 1.3 [47]. P, when content is optimized has also been shown to inhibit the formation of carbides and sulfides [48,49] and reduce swelling [50]. One study done on an RPV steel demonstrated an improvement to hot ductility by a reduction in GB sliding [51]. Another study demonstrated a reduction in DBTT and P grain boundary segregation in an irradiated Fe – P alloy with higher P contents [52] while another demonstrated an increase in DBTT as a result of increased P content [53]. The literature indicates that there is a level of uncertainty of the effects of P in a variety of alloys as well as a lack of experimental studies on the influence of P on the irradiation microstructure and resulting mechanical behavior in ferritic alloys specifically thus providing the impetus for investigating binary model Fe – P alloys

The ferritic Fe – 4.5at%P alloy has two equilibrium phases below 443 °C; a volume fraction of approximately 82% α Fe and 18% β Fe_3P. The binary Fe – P phase diagram is provided in Fig. 2.1. These Fe_3P β precipitates form between α Fe grains and have a body center tetragonal (BCT) crystal structure and covalent bonds between Fe and P atoms. Other phases that can form in the Fe – P binary system include, Fe_2P, and FeP phosphide phases as P concentration increases past ~33at%P and 50at%P respectively. All of these phosphide phases have been observed in ferritic and austenitic Fe alloys after irradiation [25,41,47,54]. Soluble P is an

undersized substitutional atom in α Fe which has a strong affinity to self-interstitial Fe atoms and tends to form a highly stable mixed di interstitial dumbbell with self-interstitials Fe atoms in the center atom location aligned along the <011> directions [55]. Since P is undersized it is expected to have a negative misfit and the surrounding lattice is expected to contract [56]. The undersized misfit of the P atom in α Fe results in strong trapping of SIAs. In addition to the undersized misfit P also tends to form a strong covalent bond with Fe which enhances the trapping capability of P in α Fe. Furthermore, since P is undersized in Fe, it is expected to segregate to defects under irradiation. This P segregation has been shown to result in P clustering and radiation induced phosphide formation [47,57,58]. The concepts of substitutional atoms and interstitials will be discussed in section 2.2 and the concepts of interstitial trapping and radiation induced di interstitial formation will be discussed in section 2.3. The grains in the Fe – 4.5at%P alloy are quite large, hundreds of μm in diameter with random orientation. An EBSD map of the unirradiated Fe – P bulk sample is provided in Fig. 2.2.

2.1.4 Iron – Nitrogen

Nitrogen is another element that is often present in Fe alloys as an impurity but has also been used as an alloying element to enhance various properties. N as an alloying element has been used in austenitic steels to improve the impact toughness and yield strength. N has also been used to improve corrosion resistance and to prevent the formation of undesirable secondary phases [59,60]. Studies have reported resistance to irradiation embrittlement and swelling. CJ Rietema et al reported that although increased N resulted in higher irradiation defect densities, the irradiation hardening was reduced because nitrides acted as sinks Ni clusters which resulted in the removal of these clusters from dislocations [20]. Another study by E Aydogan reported reduced irradiation hardening as a result of larger defect sizes, lower defect densities [21]. Alternatively, studies have also reported on the detrimental effects of N. Studies have reported embrittlement in Fe alloys through nitride formation as well as irradiation embrittlement. One study reported irradiation induced point defect trapping of nitrogen atoms which produced a finer defect structure and irradiation hardening [18,19,61]. N has also been shown to reduce the stacking fault energy and induce localized deformation and stress induced martensitic phase transformation [62]. The literature indicates that the irradiation microstructure and mechanical

results are mixed for N in steels. Furthermore, there are no studies that aim to isolate the effects of N by using binary model ferritic alloys thus presenting a gap in the literature.

The ferritic Fe – 3at%N alloy has two equilibrium phases, α Fe and Fe_4N. Fig 2.3 provides the Fe – N phase diagram. Fe_2N can also form in in the Fe – N binary alloy system as the concentration of N increases past ~30at%N. Austenitic Fe can also form in the Fe – N binary alloy system at temperatures above 590 °C and at N concentrations between 0 and ~11at%N. Soluble N typically occupies an octahedral interstitial site in α Fe [54,63,64]. Since N is an interstitial solute it is expected to produce a positive misfit strain and expand the surrounding lattice outward [65]. The grain structure of the Fe – 3at%N alloy was similar to that of the Fe – 4at%P alloy with large grains, hundreds of μm in diameter with no indication of grain orientation preference. The Fe – 3at%N EBSD grain map is provided in Fig. 2.4.

2.1.5 Iron – Chromium

Chromium is an alloying element commonly used in Fe based alloys to improve oxidation and corrosion resistance. The corrosion resistance is attributed to the passive layer that forms in these alloys. Alloys containing more than 11at% Cr are referred to as stainless steels. Sources have indicated that at least 11at% Cr is required for enhanced corrosion resistance however many of the Fe-Cr engineering alloys currently being investigated have 9at% Cr because they offer adequate resistance to oxidation and corrosion while providing better toughness and DBTT [66–70]. The high strength, stiffness, and adequate toughness of these alloys make them suitable for a wide variety of load bearing applications including automobiles, bridges, turbine blades, and others [35,71–73]. There are three primary classes of stainless steel including austenitic, ferritic and martensitic. Composition and processing parameters can be adjusted and optimized to produce austenitic-ferritic, ferritic-martensitic, and precipitate strengthened stainless steels. Ferritic stainless steels are attractive candidate materials for a wide range of applications because they are less expensive than their austenitic counterparts and will be the focus of this section [74]. Ferritic stainless steels are also widely used for nuclear reactor core structural materials because of the improved radiation tolerance. Cr in ferritic alloys has been shown to improve swelling resistance as well as corrosion and oxidation at high temperatures such as those encountered in next generation nuclear reactors [71].

Despite the enhanced resistance to oxidation, corrosion, and swelling, these Fe – Cr alloys are susceptible to irradiation induced α' precipitation which is detrimental to the mechanical behavior in these alloys. Several studies have shown enhanced Cr clustering and α' precipitation at lower dose rates. α' precipitation is not typically seen at high dose rates such as those produced in ion irradiation experiments [57,75,76]. In fact, only one study has demonstrated Cr clustering and α' precipitation in a Fe – Cr alloy under ion irradiation. Other studies have shown increased irradiation hardening and reduced local corrosion resistance as a result of Cr segregation and α' precipitation. The same study indicated that the Cr clustering was not a result of RIS because the Cr clustering was not associated with any defects while other studies reported Cr clustering around defect sinks that were stabilized by impurities. These conflicting conclusions as well as the inconsistencies in the relationship between dose rate and α' precipitation indicate that the mechanisms of Cr clustering and α' precipitation are not fully understood [77]. The gap in understanding of irradiation induced or assisted Cr clustering and α' precipitation provides for motivation for further investigation. Furthermore, much data exists for irradiation microstructure and mechanical behavior of ferritic Fe-Cr alloys more generally and these alloys are promising candidate materials for next generation nuclear structural applications, it serves as a good benchmark to compare the other two previously mentioned alloys against. A comparison of the irradiation microstructures of ferritic Fe-Cr, Fe-N, and Fe-P is missing from the literature and serves as the motivation for including Cr as an alloying element in this study.

The ferritic Fe – 9at%Cr alloy has two equilibrium phases, α Fe and a Cr rich α' phase which is reflected in the Fe – Cr binary phase diagram in Fig 2.5. Both phases are BCC however the α' phase exhibits increased embrittlement. Fe and Cr atoms are metallically bonded and Cr occupies a substitutional position in α Fe. Cr is slightly oversized in the α Fe lattice with a volume mismatch of 4.36% [65,78]. Since Cr is oversized in Fe it makes the di interstitial dumbbell arrangement less stable so Cr forms more stable crowdions with self-interstitial atoms. Crowdions will be discussed further in section 1.2 [79]. The grain structure in the Fe – Cr alloy was much finer than the grain structures of the Fe – P or Fe – N alloys. The Fe – Cr EBSD map is shown in Fig. 2.6.

2.2 Irradiation Damage in Metals

2.2.1 Quantifying Radiation Damage

Irradiation damage is introduced into metals and alloys when energetic particles such as neutrons, protons, electrons, or heavy ions impact atoms of the target metal. This document will focus on the damage produced by heavy ions. If these incident ions carry enough energy, E_i, the impacted atom in the target metal will be displaced from its lattice position by the incident ion. The displaced atom will be called the primary knock-on atom (PKA). Once the PKA is displaced from its lattice site, it too will carry some transferred energy, T, and it may impact other lattice atoms in the host material. If the transferred energy, T, is large enough, the PKA will produce more displaced atoms. The displaced atoms will eventually settle into interstitial sites and the result will be a self-interstitial atom (SIA) and a vacancy for each displaced atom in the host material known as Frenkel pairs, and a damage cascade. The damage produced in the target material is quantified by number of displaced atoms over some period of time which will be called the displacement rate, R_d which is given in Eq 2.1.

$$R_d(x) = NI \int_{E_d}^{\gamma E} \sigma(E,T)\nu(T)\, dT \qquad \text{Equation 2.1}$$

where $R_d(x)$ is depth dependent displacement rate, N is the number density of target atoms, I is the ion flux, γ is a dimensionless value that quantifies how much energy is transferred between colliding particles, E is ion energy, E_d is the displacement energy of the target atoms, $\sigma(E,T)$ is the collision cross section which defines the probability of collision between incident ions and target atoms, and $\nu(T)$ is the displacement function which quantifies the number of displacements resulting from an incident ion. If it is assumed that $\sigma(E,T)$ and $\nu(T)$ are defined by Rutherford scattering and the Kinchin-Pease model respectively, then the displacement rate can be rewritten as the following:

$$R_d = \frac{\pi Z_1^2 Z_2^2 \varepsilon^4}{4E_i E_d}\left(\frac{M_i}{M}\right)\ln\frac{\gamma E_i}{E_d}\frac{dpa}{ion/cm^2} \qquad \text{Equation 2.2}$$

where Z_1 and Z_2 are the atomic numbers of the incident ion and the target atom respectively, M_i and M are the mass of the ion and the mass of the target atom respectively, and ε is the secondary atom knock-on energy unit charge. Since heavy ions are more massive and the interaction cross section of the incident ions is much larger, these energetic particles produce more damage at a shorter depth into the target material. The

damage profile, which is the displacements per atom (dpa) as a function of target depth, increases rapidly over a small depth range before peaking and then dropping to zero. Fig. 2.7 shows the irradiation damage as a function of target depth for protons, ions, and neutrons. Although the damage profile produced by ion irradiation is significantly different than the damage profile of neutron irradiation, ion irradiation experiments serve as an attractive alternative to neutron irradiation because the resulting microstructure is largely comparable with some exceptions [80]. Irradiation damage in metals and alloys results in 1D defects such as vacancies and interstitials. These 1D defects interact with other defects in complex ways including interstitial / vacancy recombination which result in the annihilation of the interstitials and the vacancies and defect agglomeration which manifests as interstitial / vacancy clusters, dislocation loops, voids, bubbles and precipitates. The formation and the evolution of these defects are influenced by many parameters including the irradiating particle type, irradiation dose, dose rate, temperature, alloy composition and others. Radiation enhanced diffusion (RED) promotes the growth of these defects while RIS promotes the formation and growth of secondary phases. These concepts will be discussed in more detail in the following sectio[7,81].

2.2.2 Irradiation Induced Defects

Point Defects

Point defects are defects in a crystal lattice that have zero dimensions and produce a distortion of that lattice. These defects are thermodynamically inevitable in crystalline solids. Point defects include substitutions, interstitials and vacancies. Vacancies, which are the simplest of crystalline defects are empty lattice sites. Substitutional atoms are solute atoms that occupy the lattice sites of a host material. Interstitial atoms are atoms that occupy the sites in the spaces between the lattice sites in a crystalline solid [7,69].

Interstitial atoms can be solute atoms such as impurities or alloying elements or self-interstitial solvent atoms. In FCC and BCC crystal lattices interstitials will typically occupy tetrahedral or octahedral sites. In tetrahedral sites all surrounding solvent atoms are distanced $a\sqrt{5}/4$ from the interstitial atom. In the octahedral sites two of the solvent atoms are distanced $a/2$ from the interstitial atom. Since octahedral sites are smaller, more lattice distortion is

required to force an interstitial atom into one of these sites. Tetrahedral sites are larger than octahedral sites and they can accommodate larger interstitial atoms. Furthermore, there are more tetrahedral sites and tetrahedral impurities are more common than octahedral impurities. There are four octahedral sites and eight octahedral sites in the FCC. There are six octahedral sites and twelve tetrahedral sites in the BCC lattice. Self-interstitials can occupy these interstitial sites, but significant lattice distortion is usually required to form octahedral or tetrahedral self-interstitials since solvent atoms are typically much larger than the interstitial sites. Other interstitial configurations include di interstitial dumbbells and crowdions which are more commonly formed by self-interstitial and displaced substitutional atoms. Di interstitial dumbbells are solvent atom pairs that share one lattice site. The di interstitial dumbbells tend to align along a direction that minimizes the strain energy in the surrounding lattice. For BCC and FCC metals and alloys the lowest energy di interstitial dumbbell directions are the <011> the <001> directions respectively. SIAs can also arrange into crowdion configurations which are essentially a di interstitial dumbbells spread out over many lattice atoms aligned along the <111> direction.

During irradiation an excess number of point defects, vacancies and SIAs, are produced when incident particle displace lattice atoms from the target material. The SIAs become lodged in the lattice to form octahedral, tetrahedral, di interstitial dumbbells, or crowdion configurations. The lattice distortion produced by the di interstitial dumbbells, which are the most stable configuration for these SIAs, results in strong interactions with other defects including other SIAs, solute atoms, vacancies and dislocations and serve as nucleation sites for radiation induced defects such as vacancy and interstitial clusters and dislocation loops. The lattice distortion of crowdions is similar to that of di interstitial dumbbells as such, these defects also interact strongly with defects such as SIAs and serve as nucleation sites for interstitial clusters and dislocation loops [7,82]. Images of the tetrahedral and octahedral configurations for FCC and BCC are provided in Fig. 2.8, images for the various di interstitial dumbbell configurations and crowdion configurations for FCC and BCC are provided in Fig. 2.9.

Defect Nucleation

SIAs tend to be strongly attracted to di interstitial dumbbells and these defects can act as nucleation sites for interstitial or vacancy clusters and dislocation loops. Furthermore, since di interstitial dumbbells interact strongly with solute atoms, these defects can also act as locations

where solute segregation can occur. All interstitial atoms put a positive or compressional strain on the surrounding lattice. The interstitial volume size factor, which is provided in Eq. 2.3, is a measure of the interstitial misfit in the host material lattice.

$$\Omega_{sf} = \frac{1}{\Omega_A}\left(\frac{\partial \Omega}{\partial c}\right) \quad \text{Equation 2.3}$$

where Ω_{sf} is the volume size factor of the interstitial atom, Ω_A is the atomic volume of the solvent, and $\partial\Omega/\partial c$ is the change in the atomic volume of the solvent atom with a change in the concentration of the solute. The volume size factors for several interstitial Fe solutions were calculated using the data from [83] and are tabulated in [63].

Substitutional atoms also produce a strain on the surrounding lattice since these atoms are either smaller or larger than the solvent atoms. These substitutional atoms can produce an expansion or contraction of the surrounding lattice, which is known as the substitutional atom misfit. The volume size factor, provided in Eq. 2.4 and similar to that of interstitial atoms, is a measure of the misfit strain produced by the substitutional atom.

$$\Omega_{sf} = \frac{\Omega_B^* - \Omega_A}{\Omega_A} \quad \text{Equation 2.4}$$

where Ω_{sf} is the volume size factor of the substitutional atom, Ω_B^* is the atomic volume of the substitutional atom, and Ω_A is the atomic volume of the solvent atom. The volume size factor is essentially the percentage difference of the solvent atom and the substitutional atom. For undersized substitutional atoms, atoms which are smaller than the solvent atoms, the volume size factor will be negative and for oversized substitutional atoms the volume size factor will be positive. The volume size factors for many substitutional solid solutions are provided in [78].

These point defects contribute to the irradiation induced defect nucleation and the resulting defect microstructures of these materials. For instance, the misfit strain produced by undersized and oversized substitutional atoms results in interactions between the substitutional atoms and other migrating defects similar to the interactions between defects and di interstitial dumbbells and crowdions. The magnitude and sign of the misfit i.e., undersized or oversized substitutional atoms will influence the strength of the interaction, the stability of the resulting defect, and the type of defect that is formed. For instance, phosphorus, which is typically an undersized substitutional atom in α Fe, tends to interact strongly with and trap migrating SIAs because of its' magnitude and sign of volume size factor, -13.16% in the α Fe lattice. Furthermore, the excess space, which is provided by the undersized atom, allows for di

interstitial dumbbells to form. As such, the Fe-P mixed di interstitial dumbbell tends to be a dominant and highly stable defect configuration [7,55,57,84–87]. The enhanced SIA trapping formation of these di interstitial dumbbell defects by undersized solute atoms results in more cluster and dislocation loop nucleation and increased defect densities which is demonstrated in many studies [27,86,88]. Eq. 2.5 describes the increased defect density resulting from enhanced SIA trapping.

$$C_L = \left(\frac{P}{M_I}\right)^{\frac{1}{2}} \qquad \text{Equation 2.5}$$

where C_L is the concentration or density of dislocation loops or clusters, P is the production rate of point defects and M_I, which is provided in Eq. 2.6, is the mobility of SIAs.

$$M_I = \nu exp\left(\frac{-E_I^m}{kT}\right) \qquad \text{Equation 2.6}$$

where ν is the lattice vibrational frequency, E_I^m is the migration energy of SIAs, k is Boltzmann's constant, and T is the temperature. These two equations indicate that the density of defects increases as the mobility of SIAs decreases and that the mobility of SIAs increases with increasing temperature and decreases with increasing SIA migration energy. Stronger traps i.e. undersized substitutional atoms increase the SIA migration energy and more stable defect nucleation sites i.e. highly stable di interstitial mixed dumbbells configurations result in lower SIA migration and defect nucleation sites that remain stable over a range of temperatures.

Although the SIA trapping capability of oversized substitutional atoms is generally weaker, they interact with migrating SIAs in similar ways and can also result in increased defect densities, but the resulting defect types may be different [84]. For instance, since crowdion defects are essentially di interstitial dumbbells that have been spread over many lattice sites they don't require as much lattice space to form as simple di interstitial dumbbells do. Therefore, oversized substitutional atoms that occupy more lattice space can form crowdions. This explains why substitutional Cr in α Fe tends to interact with a form stable crowdions. Furthermore, SIAs migration is slowed by Cr in α Fe [89,90]. When the solute atoms become too large there is evidence that they will not form di interstitial dumbbells or crowdions or that the di interstitials that will form will be unstable [91]. Similarly, the space occupied by tetrahedral and octahedral interstitial atoms also limit the space available for di interstitial dumbbells and crowdions to form and thus inhibit the formation of these irradiation induced defect nucleation sites. The solute size

also plays an important role in the diffusion and segregation of point defects in irradiated alloys which will be discussed in the following section.

2.2.3 Radiation Enhanced Diffusion (RED)

Atoms and vacancies in a crystalline lattice diffuse through a material by making jumps from one position to a neighboring position. A diffusing atom can jump from a lattice site to a neighboring lattice site, from a lattice site to a neighboring interstitial site, from an interstitial site to a neighboring vacant lattice site, or from an interstitial site to a neighboring interstitial site. Vacancy diffusion is associated with atoms migrating by jumping to vacant lattice sites while interstitial diffusion occurs when atoms migrate by jumping to interstitial sites. The only requirements for a jump to occur is that the atom or vacancy has enough energy to make the jump and that the location the atom or vacancy is jumping to is available. These jumps occur randomly but macroscopically the direction of diffusion is always from a region of high concentration to a region of low concentration. During irradiation the concentration of interstitials and vacancies is increased beyond equilibrium levels, which will be discussed in the next section, and atoms get kinetic energy from the incident particles in addition to the thermal energy that already exists in the system. The high point defect concentration and the extra energy provided by the incident energetic particles results in higher interstitial and vacancy diffusion rates [7].

Defect Reactions

Under irradiation interstitials and vacancies are created by the displacement of lattice atoms. These interstitials and vacancies can build up in the system, they can be trapped at sinks, or they can annihilate each other. Sinks are point defect absorbing surfaces and include features in a crystalline solid such as the material surface, grain boundaries, dislocations, dislocation loops, clusters, and solute atoms etc. The point defect balance equations, given in Eq 2.7 and 2.8 describe how point defect concentration changes with time [7].

$$\frac{dC_v}{dt} = K_0 - K_{iv}C_iC_v - K_{vs}C_vC_s \qquad \text{Equation 2.7}$$

$$\frac{dC_i}{dt} = K_0 - K_{iv}C_iC_v - K_{is}C_iC_s \qquad \text{Equation 2.8}$$

where K_0 is the defect production rate, K_{iv} is the vacancy-interstitial recombination rate, C_i is the

interstitial concentration, C_v is the vacancy concentration, C_s is the sink concentration, and K_{vs} vacancy-sink reaction rate coefficient, and K_{is} is the interstitial-sink reaction coefficient. The second and third terms in Eq. 2.7 and 2.8 account for annihilation with opposite point defects and annihilation at sinks respectively. Four conditions are defined by the defect reaction rate model; the low temperature / low sink density condition, the low temperature / intermediate sink density condition, the low temperature / high sink density condition, and the high temperature condition. This section will focus the low temperature / intermediate sink density, and low temperature / high sink density conditions, shown graphically in Fig. 2.10 and 2.11 respectively, as these represent the irradiation conditions for this study since the irradiation temperature of 370 °C is too low to initiate substantial vacancy diffusion, well below $0.5T_m$ for Fe – 4.5%P, Fe – 9.5%Cr, or Fe – 2.3%N, and undersized oversized solute atoms are expected to produce a high sink density and intermediate sink density respectively for point defects [7].

In a low temperature / intermediate sink density condition, there are three regimes, the build up of interstitials and vacancies, interstitial annihilation by sinks, and annihilation of vacancies by sinks. In the build up regime, interstitials and vacancies have not reached opposite defects or sinks so annihilation doesn't occur and the second and third terms of Eq. 2.7 and 2.8 go to zero. Eventually, as point defects build up they begin to reach opposite defects where the defects annihilate with each other and the second terms of Eq. 2.7 and 2.8 contribute to the change in point defect concentration resulting in a slowing of the increasing concentration. This coincides with a transition from the build up regime to the annihilation of interstitials at sinks regime. During this transition interstitial concentration has reached saturation and vacancy concentration has reached a quasi saturation as interstitials and vacancies begin to interact with and annihilate each other. The second term that accounts for the annihilation of interstitials at vacancies in Eq. 2.8 balances with the production rate term and the increase of interstitials terminates. The third term that accounts for interstitial annihilation at sinks is still negligible since interstitials have not yet reached sinks. The second term in Eq 2.7 contributes to but does not completely balance with the production of vacancies so concentration of vacancies continues to increase at a slower rate. As interstitials begin to reach sinks while still being annihilated by vacancies, there is a combined contribution from the second and third term in Eq 2.8 and there is a decline in the interstitial concentration. As interstitials are lost to sinks they are no longer contributing as much to vacancy annihilation and vacancies are allowed to increase at a faster

rate. Finally, as the third regime is reached where vacancies also begin to reach sinks, vacancy concentration reaches a steady state. Furthermore, since the vacancies lost to sinks no longer contribute to interstitial annihilation, the decline of interstitials stops, and interstitial concentration reaches steady state [7].

In a low temperature / high sink density condition, there exists four regimes of point defect evolution; the buildup of vacancies and interstitials without reaction, the loss of interstitials at sinks, the mutual recombination of interstitials and vacancies which exceeds the loss of interstitials to sinks, and finally the loss of vacancies to sinks. In the buildup regime, interstitials and vacancies have not had time to reach each other or sinks so no annihilation occurs and the second and third terms in Eq. 2.7 and 2.8 are negligible. At lower temperatures, vacancy diffusion is negligible but interstitial diffusion still occurs, so vacancies will not reach sinks as quickly as interstitials. In the high sink density case, interstitials will reach sinks before they reach vacancies and interstitial concentration will saturate in the second regime, interstitial annihilation at sinks. In the second regime the third term in Eq 2.8, interstitial annihilation at sinks, contributes to interstitial concentration and balances with interstitial production. Vacancy interactions still do not occur and the second and third terms in Eq 2.7 are still negligible thus vacancy concentration continues to increase at the rate of vacancy production. As more time passes and vacancy concentration continues to increase, they begin to interact with interstitials and the increase in vacancy concentration slows which is associated with the third regime, annihilation at opposite defects. Furthermore, the interaction between interstitials with vacancies combined with the loss of interstitials to sinks, which is associated with the contributions of both the second and third term in Eq. 2.8, results in a decrease in interstitials concentration. In the third regime, the second term in Eq. 2.7, annihilation from interaction with opposite defects, contributes which is responsible for the decreasing rate of increase of vacancy concentration. Finally, in the fourth regime, vacancies also begin to reach sinks, the second and third terms in Eq. 2.7 contribute, and the vacancy concentration reaches steady state. The loss of vacancies at sinks results in less interactions between vacancies and interstitials so the decrease in interstitial concentration stops and interstitial concentration reaches steady state as well. In the fourth regime, the second and third terms in Eq. 2.7 and 2.8 balance the production of point defects. The concentration of sinks, interstitials, and vacancies also plays a significant role in the segregation of solutes at sinks which will be discussed in the following section.

2.2.4 Radiation Induced Segregation (RIS)

Radiation induced segregation involves the enrichment or depletion of solvents and solutes in a multicomponent alloy at defects such as grain boundaries, dislocations, dislocation loops and clusters. This section will focus on the RIS in binary alloys since binary alloys are being investigated in this study. When point defects are created during irradiation, as the concentrations of interstitials and vacancies build up in the alloy, they will eventually be attracted to and absorbed by defect sinks in the material which will produce a flux of these point defects to the sinks. These defect fluxes will be tied to the movement of atoms in the alloys. As such, the net flow of interstitials or vacancies to these sinks will coincide with a net flow of atoms to or from the sinks. For instance, when vacancies move toward a sink, there will be a net flux of atoms away from the sink. When interstitials move to sinks there will be a net flux of atoms to the sinks. In a binary alloy the solvent atoms and solute atoms will follow the defect fluxes differently. If solute atoms participate in vacancy flux more than do solvent atoms, there will be a net flow of solute atoms away from the sink and the sink will become depleted of the solute just as if a solvent atom more strongly follows interstitial flux to a sink there will be an enrichment of the solvent at the defect sink. The enrichment or depletion of either component in a binary alloy will lead to concentration gradients at and around the defect sink. The difference in size between the solute and solvent atoms will influence the enrichment or depletion and the degree of segregation at defect sinks. This is because vacancies and interstitials preferentially interact with undersized and oversized substitutional atoms in different ways. Self-interstitial atoms will preferentially change positions with undersized substitutional atoms. This preferential switch reduces the strain in the lattice because undersized substitutional atoms can more easily fit into the interstitial positions than self-interstitial atoms. The preferential switching of self-interstitial atoms in interstitial positions with undersized substitutional atoms results in a net movement of undersized substitutional atoms migrating as interstitials. As such, these undersized substitutional atoms will move toward interstitial sinks and enrichment of the undersized substitutional element will occur at the sink. Since self-interstitial solvent atoms will preferentially switch with undersized substitutional atoms to occupy lattice sites they will move in the opposite direction of interstitial migration and will deplete from interstitial sinks. Similarly, vacancies typically switch positions with oversized substitutional atoms to reduce the strain energy in the lattice which is associated with the vacancy component of the inverse

Kirkendall mechanism. As such, oversized substitutional atoms will move in the opposite direction of vacancies and away from vacancy sinks resulting in a depletion of oversized substitutional solutes at vacancy sinks [7,13,92].

RIS effects are heavily influenced by temperature and dose rate as seen in temperature dependent and dose rate dependent segregation studies. The temperature dependent RIS intensity for several dose rates is shown graphically in Fig. 2.12. At lower temperatures interstitial and vacancy diffusion is lower, migration toward sinks is reduced and there will be a higher concentration of interstitials and vacancies. Similarly, for a given temperature, when dose rate is high the concentration of point defects will also be high. With high point defect concentration, recombination dominates. Vacancies and interstitials are more likely to annihilate each other than they are to find sinks and the RIS effect is reduced. As temperature increases, interstitials and vacancies can increasingly find sinks, so solvents and solutes that migrate to and away from sinks via interstitial and vacancy mechanism will either enrich or deplete at sinks. When the temperature gets too high, back diffusion takes over and RIS intensity decreases. This is demonstrated in Fe – Cr irradiation induced α' precipitation studies that showed α' precipitation in Fe – Cr alloys under neutron irradiation and a lack of α' precipitation under heavy ion irradiation. The presence of irradiation induced α' precipitation in neutron irradiated Fe – Cr alloys and the lack of α' precipitation in heavy ion irradiated alloys is a result of the large differences in dose rates produced by neutron irradiation, ~10^{-7} dpa/s and heavy ion irradiation, between 10^{-4} and 10^{-3} dpa.

In a high sink density condition however, segregation of solutes that preferentially diffuse by interstitial diffusion may still show increased RIS at lower temperatures and high dose rates because, as shown in Fig. 2.10, interstitials will interact with sinks before they recombine with vacancies if the sink density is high enough. A study by C Pareige et al demonstrated the cluster development of Si, P, Ni, and Cr in ferritic Fe – 9%Cr and Fe – 12%Cr under neutron and ion irradiation at 100 °C, 300 °C, and 420 °C. During ion irradiation, clusters development and there was some enrichment of all alloying elements but the concentrations of Si and P increased as a percentage of their original concentration significantly more than did Cr or Ni concentrations. Since Si and P are undersized substitutional atoms, they are more likely to migrate by interstitial mechanism and find sinks more easily. If sink density is high than the interstitial absorption at sinks will contribute more and there will be more segregation of undersized solutes [7,57,92].

When the local solute composition of these enriched regions reaches the solubility limit, a solute cluster may serve as a nucleation site for a radiation induced precipitate.

2.2.5 Radiation Induced Precipitation, Disordering, and Dissolution

In the simplest binary alloy system, the binary eutectic system, an α phase with solutes completely soluble in a solvent matrix separates into two solid phases, α and β, with solvent content less and solute content more than the surrounding matrix. As the concentration of solute increases in the alloy, the content of solute in the β phase will increase and the content of α will decrease. In more complex binary alloy systems, more phases may exist simultaneously or by themselves at higher solute contents or at higher temperatures. The Fe – P and Fe – N systems are perfect examples of more complex binary alloy systems with several phases, see Fig. 2.1 and 2.4 respectively. During irradiation non-equilibrium defect concentrations exist which can lead to non-equilibrium compositions of solvents and solutes at sinks as discussed in section 2.3.4. If irradiation leads to the enrichment or depletion of a solutes and solvents. The enrichment of solutes or the depletion of solvents can lead to local compositions above the solubility limit, and a radiation induced precipitate can form [7]. As the non-enriched sink progresses toward a fully developed radiation induced separate phase, the clustering and enrichment of solutes at the sink will initially produce a GP zone. The GP zone is a cluster of solutes well above the equilibrium composition of the alloy and tens of atoms in diameter. As the local composition of solute increases and the GP zone grows, a coherent precipitate will form. A coherent precipitate is a precipitate that has a continuous lattice with the surrounding matrix lattice. Eventually, as the coherent precipitate continues to increase its' solute concentration it will develop into an incoherent precipitate which as a discontinuous lattice with the surrounding matrix lattice [7,69,93]. Images of a GP zone, coherent precipitate, and incoherent precipitate are shown in Fig. 2.13 (a), (b), and (c) respectively. Common radiation induced phases seen in ferritic alloys include M_6C, α', σ, Cr_2X, and MP, M_2P, and M_3P phosphides. These phases present as needles that align along specific directions, laths, and globular particles [47].

2.3 Mechanical properties

2.3.1 Plastic Deformation

As stress is applied to a metal or an alloy, the atomic bonds are stretched, and the metal deforms elastically. As the stress increases past the elastic limit known as the yield point or the yield strength of the metal, the bonds will be broken along lattice planes, leaving incomplete or half planes of atoms in the lattice called dislocations. The presence of the dislocation in the lattice will create inherent strain in the lattice because the extra half plane of atoms is essentially squeezed into the lattice. The amount of strain produced by the extra half plane of atoms is quantified by the Burgers vector. These newly formed dislocations will be pushed through the crystalline lattice as the stress continues to increase and new dislocations will continue to form as the metal plasticly deforms. As the stress continues to increase past the yield point, and more dislocations are formed in the crystalline lattice, the dislocations will begin to interact with each other, and these dislocations will act as obstacles to the other dislocations, impeding the motion of the dislocations and requiring even more stress to push the dislocations further. The increasing stress, past the yield point, resulting from the interacting dislocations is known as strain hardening.

The movement of these dislocations is called slip. Typically slip occurs along the most atomically dense plane, termed the slip plane, in the most atomically dense direction, termed the slip direction. A slip plane / slip direction combination is known as a slip system. The densest packed plane and direction in BCC metals, shown in Fig. 2.14, are the {011} and <111> respectively which make up 12 of the BCC slip systems. The other BCC slip systems which include the {211} / <111> slip systems and the {321} / <111> slip systems, are thermally activated and are typically only activated at elevated temperatures [69].

The activation of these slip systems is generally dictated by Schmid's law. Schmid's law holds that when an external stress is applied to a single crystal, there will be a shear stress felt by non-perpendicular and non-parallel planes known as the resolved shear stress. The resolved shear stress, provided in Eq. 2.9 will depend on the applied stress direction, the slip direction, and the normal of the slip plane.

$$\tau_R = \sigma \cos\phi \cos\lambda \qquad \text{Equation 2.9}$$

where τ_R is the resolved shear stress, σ is the applied stress, ϕ is the angle between the applied stress and the slip plane normal, and λ is the angle between the applied stress and the slip direction. A graphical representation of Schmid's law is provided in Fig. 2.15. The shear stress is maximized when both the angle between the applied stress and the slip plane normal and the angle between the applied stress and the slip direction are 45°. Each slip system will have a different shear stress imparted on to it which is dependent on the applied stress direction, and generally the slip system with the highest resolved shear stress will slip first, however, if a dislocation is impeded by an obstacle such as another dislocation or a solute atom, a slip system with a lower resolved shear stress may be activated which is associated with a deviation from Schmid's law. BCC metals are known to have non-Schmid deformation or "anomalous slip" which will be discussed further in section 2.3.2. As a result of Schmid's law, different crystal orientations may produce different mechanical responses because the slip systems will be oriented differently along the direction of applied stress with each crystal orientation [69,94].

There are two types of dislocations, edge dislocations and screw dislocations, displayed in Fig. 2.16 and 2.17 respectively, however, typically dislocations are not pure edge or pure screw. Instead, most dislocations are mixed dislocations, having both edge and screw components. Edge dislocations have a Burgers vector that is parallel to the shear stress direction and perpendicular to the dislocation line direction. The dislocation line direction of an edge dislocation is perpendicular to the shear stress direction. Screw dislocations have a Burgers vector, shear stress direction and dislocation line direction that are parallel to each other. Typically edge dislocations are more mobile than screw dislocations and require less stress to push through a crystalline lattice [94].

2.3.2 Deformation Mechanisms

The most basic deformation of a crystalline solid is associated with pure slip of dislocations in the crystalline lattice, which is associated with an adherence to Schmid's Law, however, there many mechanisms by which crystalline solids can deform. Pure slip was discussed in the previous section. The following will discuss the formation of partial dislocations, stress induced martensitic transformation, and cross slip.

2.3.2.1 Partial Dislocations

If we consider a dislocation, i.e. an extra half plane of atoms in a crystalline lattice, moving along the direction of the Burgers vector, b_1, which encounters an obstacle, the dislocation may overcome or avoid that obstacle by splitting into two partial half planes of atoms known as partial dislocations Partial dislocations form when a dislocation with Burgers vector, b_1, can slip along an easier path by splitting into partial dislocations with smaller Burgers vectors, b_2 and b_3, which, when added together will equal the original Burgers vector, b_1. For BCC materials the dislocation may split into up to six partial dislocations. Dislocations split into partial dislocations in order to lower the stacking fault energy, (SFE). The stacking fault energy is lowered when the combined magnitudes of the Burgers vectors, b_2 and b_3.. b_n is less than the magnitude of the original Burgers vector, b_1. For BCC materials, dislocations can split into partial dislocations by the reactions given in Eq. 2.10, 2.11, 2.12, and 2.13

$$\frac{1}{2}[111] = \frac{1}{8}[110] + \frac{1}{8}[112] + \frac{1}{8}[110] \qquad \text{Equation 2.10}$$

$$\frac{1}{2}[1\bar{1}1] = \frac{1}{8}[0\bar{1}1] + \frac{1}{4}[2\bar{1}1] + \frac{1}{8}[0\bar{1}1] \qquad \text{Equation 2.11}$$

$$\frac{1}{2}[111] = \frac{1}{8}[110] + \frac{1}{8}[101] + \frac{1}{8}[011] + \frac{1}{4}[111] \qquad \text{Equation 2.12}$$

$$\frac{1}{2}[111] = \frac{1}{8}[110] + \frac{1}{8}[110] + \frac{1}{8}[101] + \frac{1}{8}[101] + \frac{1}{8}[011] + \frac{1}{8}[011] \qquad \text{Equation 2.13}$$

Since the cumulative magnitudes of the Burgers vectors of the resulting partial dislocations in Eqs 2.10, 2.11, and 2.12 are less than the magnitude of the Burgers vector of the original dislocation, the splitting of BCC dislocations into partial dislocations is possible. When these partial dislocations form, they will move together and maintain a separation width from each other. This distance is dependent on the stacking fault energy of the material. A smaller stacking fault energy will result in a larger partial separation width while a larger stacking fault energy will result in a smaller partial separation width. The formation of partial dislocations is not common in BCC materials because of the high SFE and the small partial separation width. Before the splitting of the dislocation, the BCC crystal will have a ABABAB stacking sequence, but since the partial half plane takes a different slip path upon splitting, the stacking sequence of the partial half plane will subsequently be ABABA'B'A'B' and a stacking fault will be formed. The space between this new stacking sequence, or the interstices of the A'B'A'B' sequence will be larger than the interstices of the original ABABAB stacking sequence which can make the resulting stacking fault unstable. The addition of interstitial atoms such as C and N can stabilize

the stacking faults by filling the excess space created by the larger interstices in the A'B'A'B'A'B' sequence [7,95,96]. The formation of partial dislocations and the continued splitting of these partial dislocations plays a significant role in the resulting deformation of BCC metals and alloys. When partial dislocation formation is facilitated, deformation twinning and stress induced martensitic phase transformations can occur. When the stacking fault energy is high, the formation of partial dislocations is more difficult and cross slip of dislocations will be favored.

2.3.2.2 Stress induced Martensitic Phase Transformations in BCC Materials

Stress induced martensitic phase transformation in BCC alloys and metals is a deformation mechanism that involves the splitting of dislocations into partial dislocations, followed by the formation of stacking faults and finally the transformation from the BCC crystal structure to either the FCC or HCP crystal structures. Generally, BCC to FCC and BCC to HCP stress induced martensitic phase transformations are uncommon and there have been a hand full of experimental studies that have demonstrated these types of transformations [97,98]. The BCC to FCC martensitic transformation involves a group of $\frac{1}{2}[1\bar{1}1]_{bcc}$ dislocations situated on every other $(011)_{bcc}$ plane. The $\frac{1}{2}[1\bar{1}1]_{bcc}$ dislocations can separate into partial dislocations by the reaction in Eq. 2.11. According to G.B. Olsen et al. if a homogeneous shears stress is applied to the resulting $\frac{1}{8}[0\bar{1}1]$ partial dislocations, a $(111)_{fcc}$ is formed. The transformation is complete when a subsequent shear stress is applied to the resulting $\frac{1}{18}[\bar{1}2\bar{1}]_{fcc}$. This reaction is known as an inverse Bogers-Burgers reaction because it is simply the reverse of the Bogers-Burgers reaction which produces an FCC to BCC transformation. The stress induced BCC to HCP martensitic transformation is similar to the BCC to FCC transformation. The BCC to HCP transformation also involves the dissociation of several $\frac{1}{2}[1\bar{1}1]_{bcc}$ on alternating $(011)_{bcc}$ planes. G.B. Olson et al explains that during the BCC to HCP transformation, an intermediate FCC transformation will take place and close packed FCC planes will be formed. the $\frac{1}{4}[2\bar{1}1]_{bcc}$ partial dislocations formed by the reaction in Eq. 2.11 are equivalent to $\frac{1}{6}[112]_{fcc}$ partial dislocations. When these partial dislocations pass through every other FCC close packed plane, the transformation to the HCP crystal structure will be triggered. The BCC lattice and the

resulting HCP lattice will share a common plane. The BCC / HCP planar relationships are shown in Fig. 2.18. The BCC / HCP planar relationships are also listed in Table 2.1 These martensitic phase transformations require high stresses or high strain rates. Studies have reported stresses up to 13 GPa in ferritic alloys to produce stress induced BCC to HCP martensitic transformations [96–100].

2.3.2.3 Cross Slip in BCC Materials

Cross slip is a deformation mechanism by which screw dislocations overcome obstacles and reduce the internal stress of the system. Recall that dislocations are often mixed, having an edge component and a screw component. In BCC metals and alloys, screw dislocations are highly immobile. When stress is imparted on these mixed dislocations it is the edge components of these mixed dislocations that will slip. When those edge components encounter obstacles like other dislocations, the slip may be terminated. The edge component of the mixed dislocation must move on a specific plane because the Burgers vector must remain perpendicular to the edge dislocation line, thus the edge component cannot cross slip. As such, the movement of this mixed dislocation won't continue until the obstacle is overcome by the edge component of the dislocation or a stress high enough to operate the screw component of the dislocation is reached. Recall that the Burgers vector of the screw component in a mixed dislocation is parallel to the dislocation line so the screw component in the dislocation is capable of cross slip. The screw component of the mixed dislocation may then cross slip onto a neighboring geometrically favorable slip plane and the edge components of the mixed dislocation can begin moving on the slip plane until the dislocation reaches another obstacle that must be overcome by cross slip. This mechanism is particularly important in BCC metals and alloys because of the many available secondary slip systems for screw dislocations to slip on to including {110}, {112} and {123} [101]. When these dislocations cross slip onto neighboring planes, the dislocations will bow outward from pinning points at the planar intersection where the cross slipping occurred. Fig. 2.19 provides a diagram of cross slipping dislocations. In addition to the relatively high number of slip systems in BCC metals and alloys, the high stacking fault energy also contributes to the extensive cross slipping seen in these materials. Stacking fault energy plays an important role in the prominence of cross slip in BCC metals and alloys because partial dislocations must recombine to produce a cross slipping dislocation and the distance between those partial

dislocations is dependent on the stacking fault energy. Metals and alloys with high stacking fault energy such as BCC materials have shorter partial dislocation splitting width, and these partial dislocations can recombine more easily when they are closer together thus increasing the likelihood of cross slip in BCC materials [7,102,103].

2.3.3 Dispersed Barrier Hardening

The yield strength of a metal or alloy is largely influenced by microstructural defects in the material, including grain boundaries, vacancies, interstitials, dislocations, dislocation loops, nano clusters, precipitates and others because these defects act as obstacles to dislocation motion. The presence of these defects inhibit the movement of preexisting dislocations in the material which increases the yield of the material. The irradiation damage of metals and alloys results in irradiation induced defects which increases the defect densities in irradiated materials resulting in more obstacles to dislocation motion and irradiation hardening. The dispersed barrier model is generally used to predict the incremental increase in yield strength resulting from increased defect densities such as those resulting from irradiation damage. The defect separation distance, given in Eq. 2.14, accounts for the defect density in the dispersed barrier model.

$$l = (N_{ob} d)^{-\frac{1}{2}} \qquad \text{Equation 2.14}$$

Where l is the distance between obstacles, N_{ob} is the number density of obstacles, and d is the obstacle size. When a dislocation encounters an obstacle such as a precipitate or a dislocation loop, the obstacle exerts a force on the dislocation that opposes the dislocations motion. The dispersed barrier model assumes that the obstacles are uniformly dispersed and immovable. As the dislocation tries to overcome the obstacle, it can bow around the obstacle or break through the obstacle, as seen in Fig. 2.20. When a dislocation completely bows around an obstacle it will close in on itself and another dislocation will be released from the bowing dislocation site as well as an obstacle that is enclosed inside of a dislocation loop. This will result in a stronger obstacle for subsequent dislocations. Bowing around the obstacle results in a line tension of the dislocation line given in Eq. 2.15.

$$\Gamma = \frac{\mu b^2}{4\pi} \ln \frac{R}{r_c} \qquad \text{Equation 2.15}$$

where Γ is the line tension of the dislocation line, μ is the shear modulus of the material, b is the Burgers vector of the material, R is half of the distance between obstacles, l, from Eq. 2.14, and

r_c is the radius of the dislocation core. The shear stress can then be related to the dislocation line tension, Burgers vector, and the half distance between obstacles by Eq 2.16.

$$\sigma_s = \frac{\Gamma}{bR} \quad \text{Equation 2.16}$$

where σ_s is the shear stress. Eqs 2.14, 2.15, and 2.16 are then used to establish the equation for Orowan strengthening given in Eq 2.17.

$$\Delta\sigma_y = \alpha M_T \mu b\sqrt{Nd} \quad \text{Equation 2.17}$$

where $\Delta\sigma_y$ is the incremental change in yield strength, α is the strengthening coefficient, and M_T is the Taylor factor, ~3.06 for ferritic alloys [104]. In Eq. 2.17 α, which is given in Eq. 2.18, accounts for the strength of the defects.

$$\alpha = \frac{1}{2\pi}\ln\left(\frac{1}{2r_c}\right) \quad \text{Equation 2.18}$$

The value of α is usually estimated to be between 0 and 1 for ferritic alloys and studies have attempted to produce a more accurate values for alpha that consider defect type and shape. G.E. Lucas provides estimated values for α based on size and type defect. Voids and large precipitates were categorized as strong obstacles with an α value of 1. Frank loops and small precipitates were categorized as having intermediate strength with α values between 0.33 and 0.45 while small bubbles, small loops or clusters, and dislocations were categorized as weak obstacles with α values between 0.11 and 0.25 [105]. L. Tan et al estimated the strength factors for similar defects in 304 stainless steel and found that cavities tended to be the strongest obstacle type at larger sizes but were weakest at defect sizes below 2 nm. Spherical precipitates and frank loops had similar strength factors that tended to fall in the intermediate range which was consistent with G.E. Lucas's estimates. $\sqrt{Nd}$ accounts for the size and number density of the obstacles. The type of dislocation / obstacle interaction, i.e., bowing around or breaking through the obstacle, will depend on the size, shape, strength, and defect type of the obstacle [7].

2.3.4 Hardness and Nanoindentation

There are several advantages associated with nanoindentation that make it an attractive mechanical characterization technique. Arrays of many indentations can be made automatically and in a relatively short period of time allowing for the easy collection of large amounts of hardness and modulus data. Nanoindentation can also be used to target small features down to

hundreds of nm in size making this characterization technique ideal for characterizing the mechanical responses of small regions of interest such as grain boundaries and ion irradiated layers. Nanoindentation is also capable of fine measurements with displacement resolution down to 1nN and 100 nm [28].

Hardness is a measurement of a material's resistance to deformation. As such, it can be related to the yield strength of a material. The hardness of a material can be evaluated by indentation onto the surface of the material. An indentation is made when a load is applied to the surface of a material by an indenter to produce an indentation on the surface of the sample. As the displacement increases and the indenter is pushed further into the surface of the sample, more pressure is needed. At the indentation site a residual indent will be left and beneath that indent there will be a plastically deformed region called the plastic zone. The size of the plastic is zone is related to the yield strength of the material. A preset maximum load or displacement is assigned prior to the experiment. The load and the displacement are tracked as the test is carried out. Higher loads are required to push the indenter deeper into the surface of the material producing a load vs displacement profile. An example of a load vs displacement profile is provided in Fig. 2.21. The displacement and the corresponding load are then used to calculate a hardness and a Young's modulus using the Oliver and Pharr method. This method uses the relationship between displacement, or height, and cross-sectional indenter area. For Berkovich indenter geometry, the relationship is provided in Eq. 2.19. Fig. 2.22 provides a diagram of the Berkovich indenter tip geometry.

$$A = 3\sqrt{3}{h_c}^2 tan^2(65.3°) = 24.56{h_c}^2 \quad \text{Equation 2.19}$$

where A is the cross-sectional indenter area, which is a function of contact depth, h_c. The cross-sectional area, A, and the maximum load, P_{max}, can then be used to calculate the hardness of the materials by Eq. 2.20.

$$H_{Berk} = \frac{P_{max}}{A} \quad \text{Equation 2.20}$$

where H_{Berk} is hardness [106,107]. The Berkovich hardness can then be used to determine the Vickers hardness and the Vickers hardness can then be used to determine the yield strength of the material. These empirical relationships are provided in Eq. 2.21 and Eq 2.22 respectively.

$$H_{Berk} = \frac{H_V}{94.495} \quad \text{Equation 2.21}$$

$$H_V = \frac{\sigma_y}{3.03} \quad \text{Equation 2.22}$$

where H_V is Vickers hardness, and σ_y is yield strength [104,108].

2.3.5 Hard Film / Soft Substrate and Ion Irradiated Layers

As ion irradiation experiments have gained popularity because of the advantages over neutron irradiation, it has become increasingly important to understand how the hardness is influenced by both the rapidly changing dose profile of the ion irradiated layer and the harder thin ion irradiated layer and the softer substrate of the bulk. The plastic zone beneath the indentation makes testing the irradiated volume difficult in several ways. Shallower indents that would keep indentation plastic zone sizes small will result in elevated hardness results, known as size effects, that may not be representative of actual bulk mechanical properties. These size effects are the result of several potential causes including lack of defects at extremely small test volumes, residual stresses from sample preparation, indenter / sample friction, or inaccuracies in the indenter area function at shallow indentation depths. Deeper indentations will test the volumes of both the ion irradiated layer and the bulk material and irradiation hardening effects will be difficult to separate from the bulk hardness. Indentations perpendicular to the ion irradiation direction have also been used to mitigate these issues but the plastic zone size, which has been estimated by Eq. 2.23, will still be an issue if the indentation is too deep because it will still expand radially outside of the irradiated zone. Furthermore, this indentation method does little to account for the rapidly changing dose profile of the ion irradiated zone.

$$\frac{c}{R_{core}} = \frac{z_{ys}}{h_c} = \left(\frac{2E}{3\sigma_y}\right)^{\frac{1}{3}} \qquad \text{Equation 2.23}$$

where c is the radius of the plastic zone, R_{core} is the radius of the indentation core for a spherical indenter tip, z_{ys} is the radius of the plastic zone for a Berkovich indenter tip, h_c is the indentation depth, E is the elastic modulus, and σ_y is the yield strength. A study by R Kasada et al. estimated the irradiation hardening of two binary alloys as the difference between the hardness measured at the ion irradiated depth of interest and the hardness of the unirradiated counterpart measured at the same depth [109].

The hardening in the irradiated region is seen in the hardness vs depth profile as a broadening of the hardness vs depth peak, termed “the shoulder” by M. Saleh et al [110]. The drop off from this broadened peak is an indication that the plastic zone underneath the indentation tip has extended outside the ion irradiated zone. The change in hardness from the

unirradiated to irradiated conditions can be established by calculating the difference between the hardness of the irradiated sample in the shoulder region and the hardness of the unirradiated sample at the same depth. This method of establishing irradiation hardening is demonstrated by R Kasada et al [109].

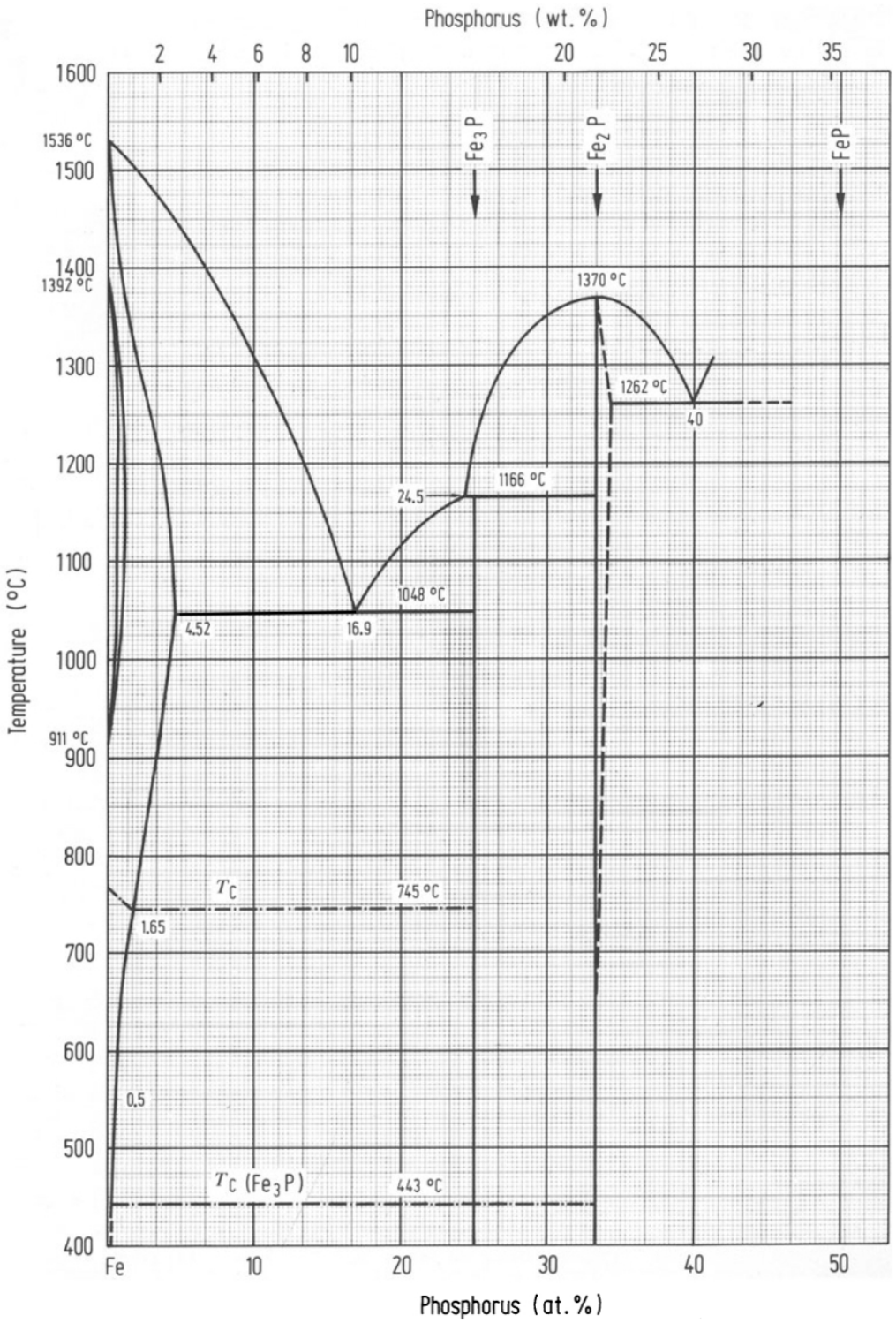

Figure 2.1: Iron – Phosphorus binary phase diagram – Adopted from [54]

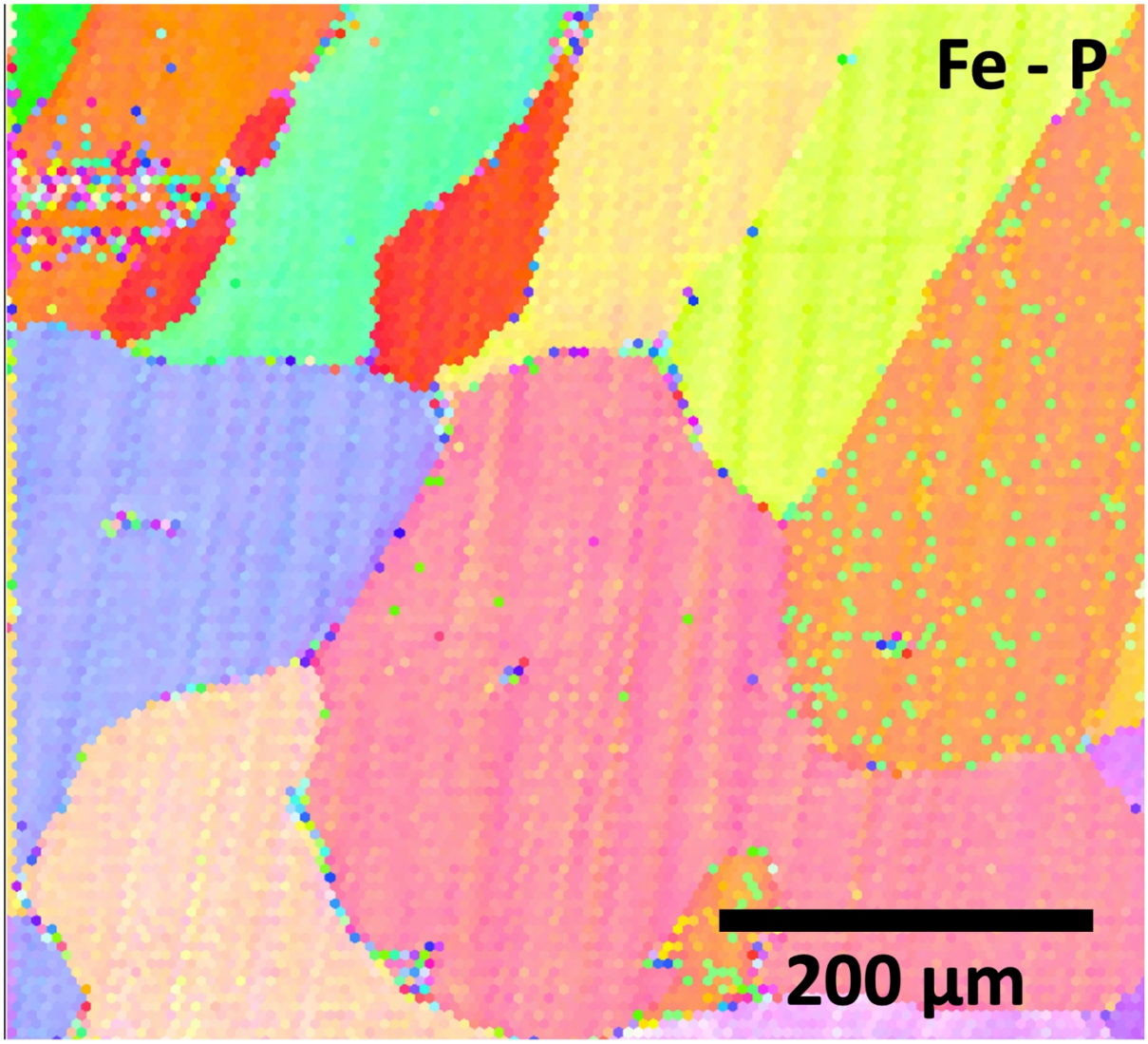

Figure 2.2: Unirradiated Fe – P EBSD grain orientation map

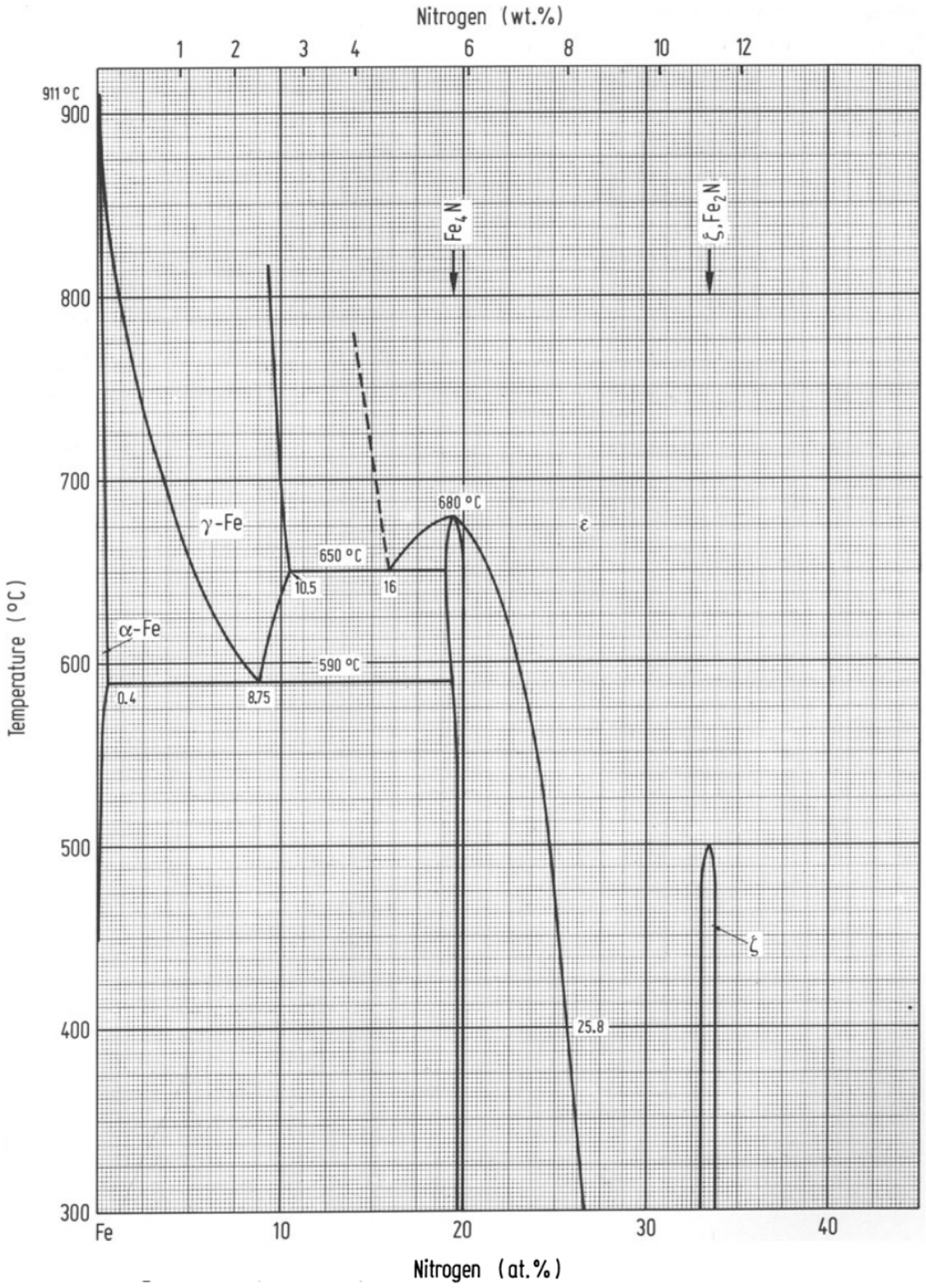

Figure 2.3: Iron – Nitrogen binary phase diagram – Adopted from [54]

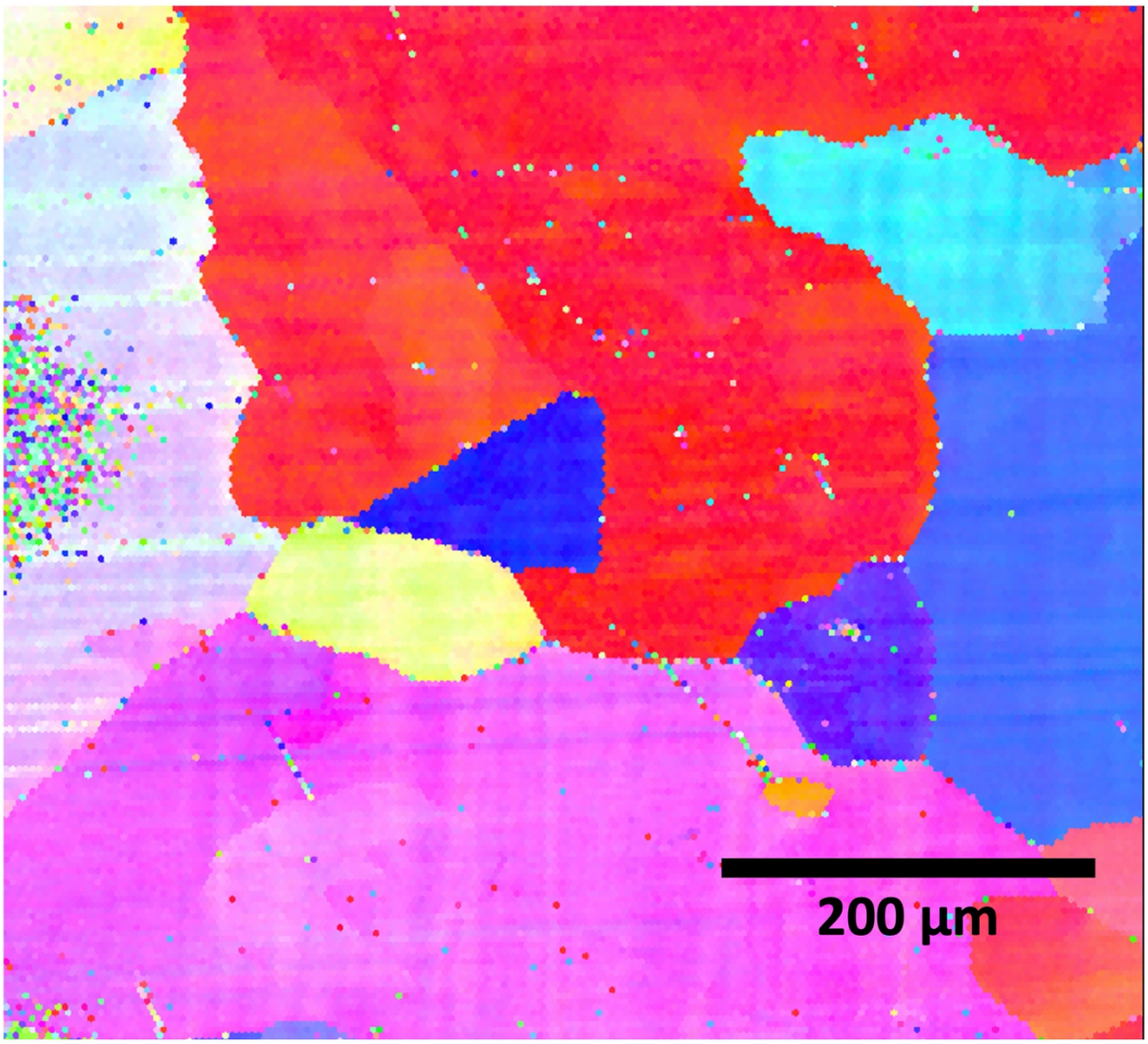

Figure 2.4: Unirradiated Fe – N EBSD grain orientation map

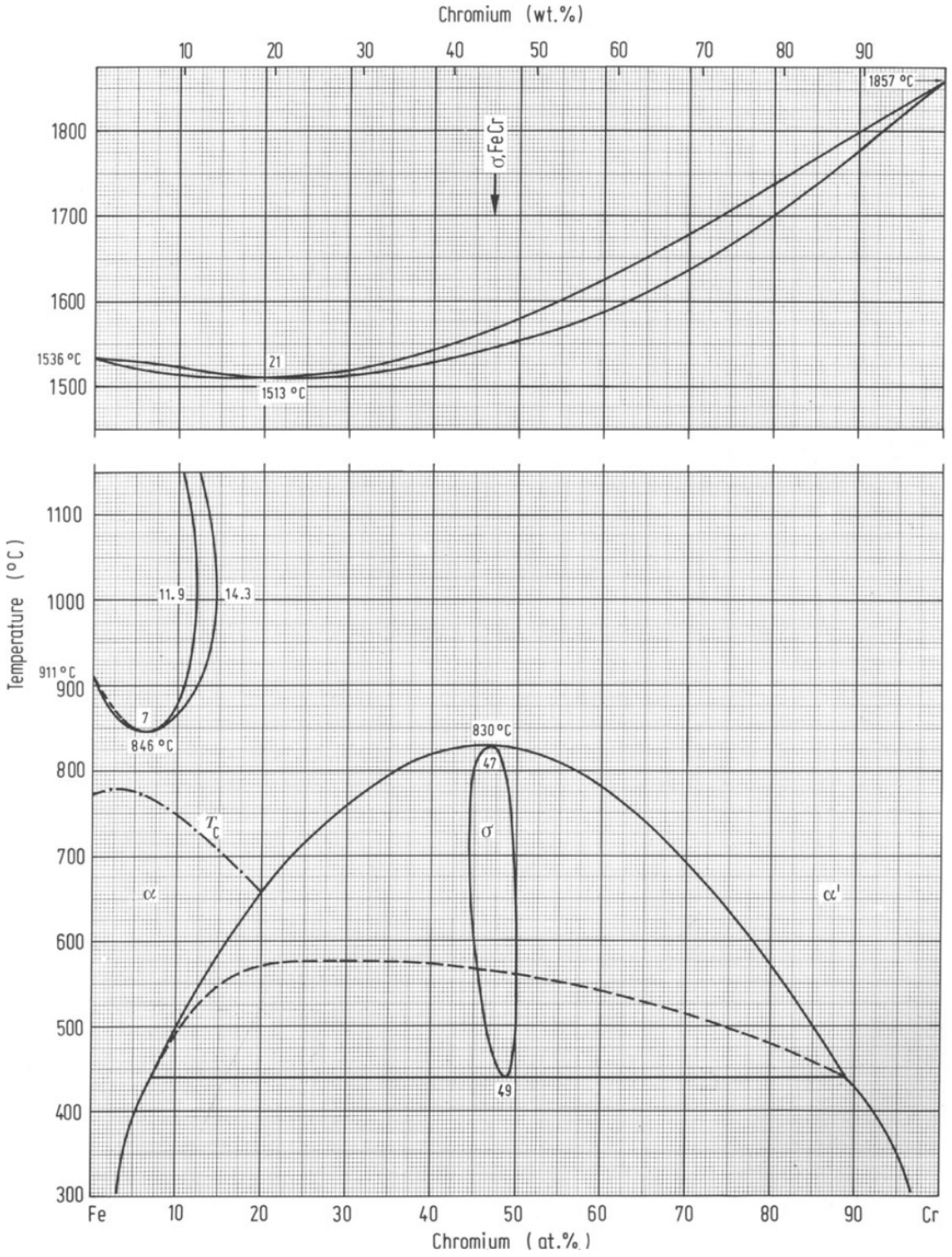
Chromium (wt.%)
10
20
30
40
50
60
70
80
90
1857 °C
σ,FeCr
1800
1700
1600
1536 °C
1500
21
1513 °C
Temperature (°C)
1100
1000
11.9
14.3
911 °C
900
7
846 °C
830 °C
800
47
T_C
σ
700
α
α'
600
500
49
400
300
Fe
10
20
30
40
50
60
70
80
90
Cr
Chromium (at.%)

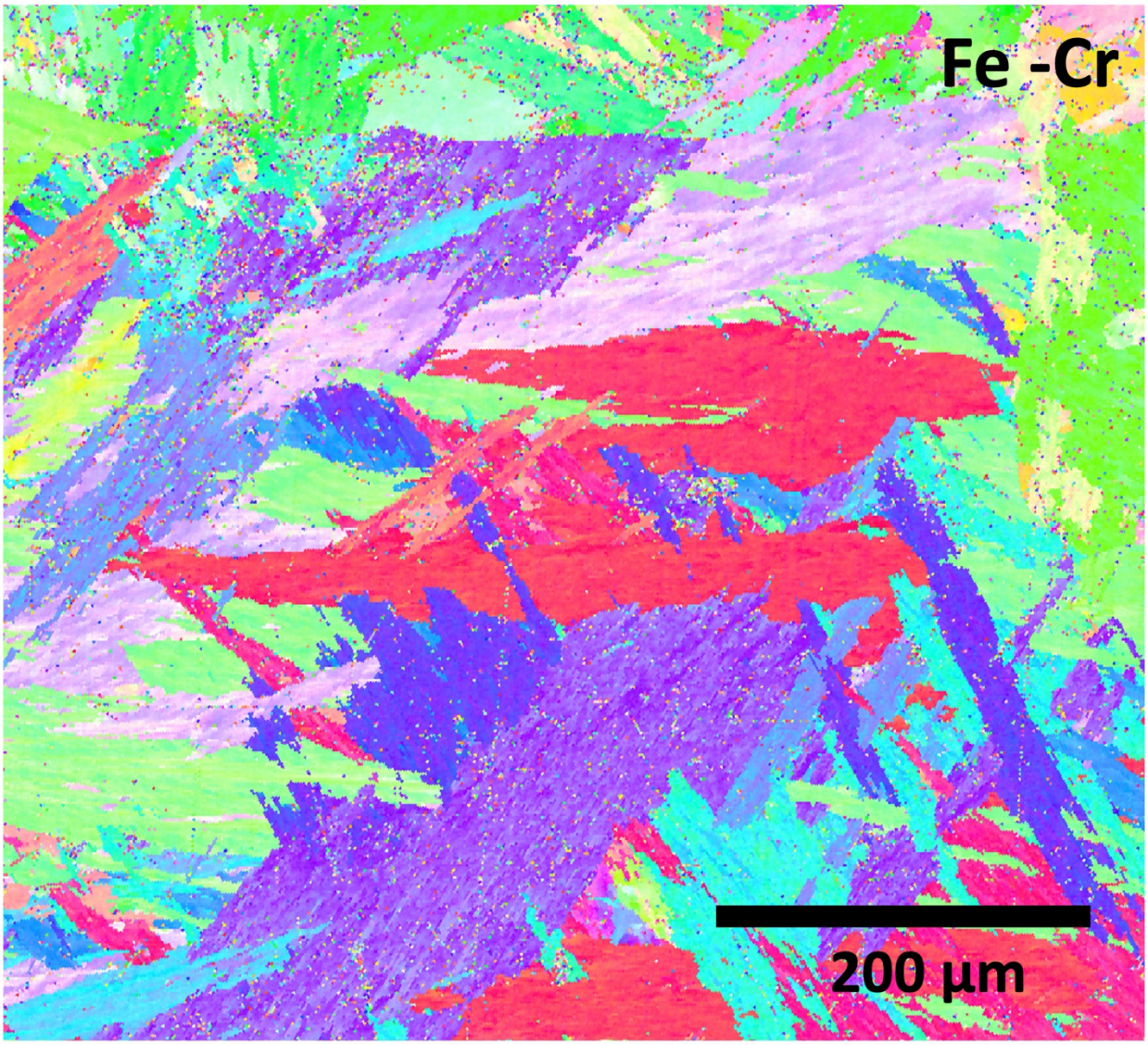

Figure 2.5: Unirradiated Fe – Cr EBSD grain orientation map

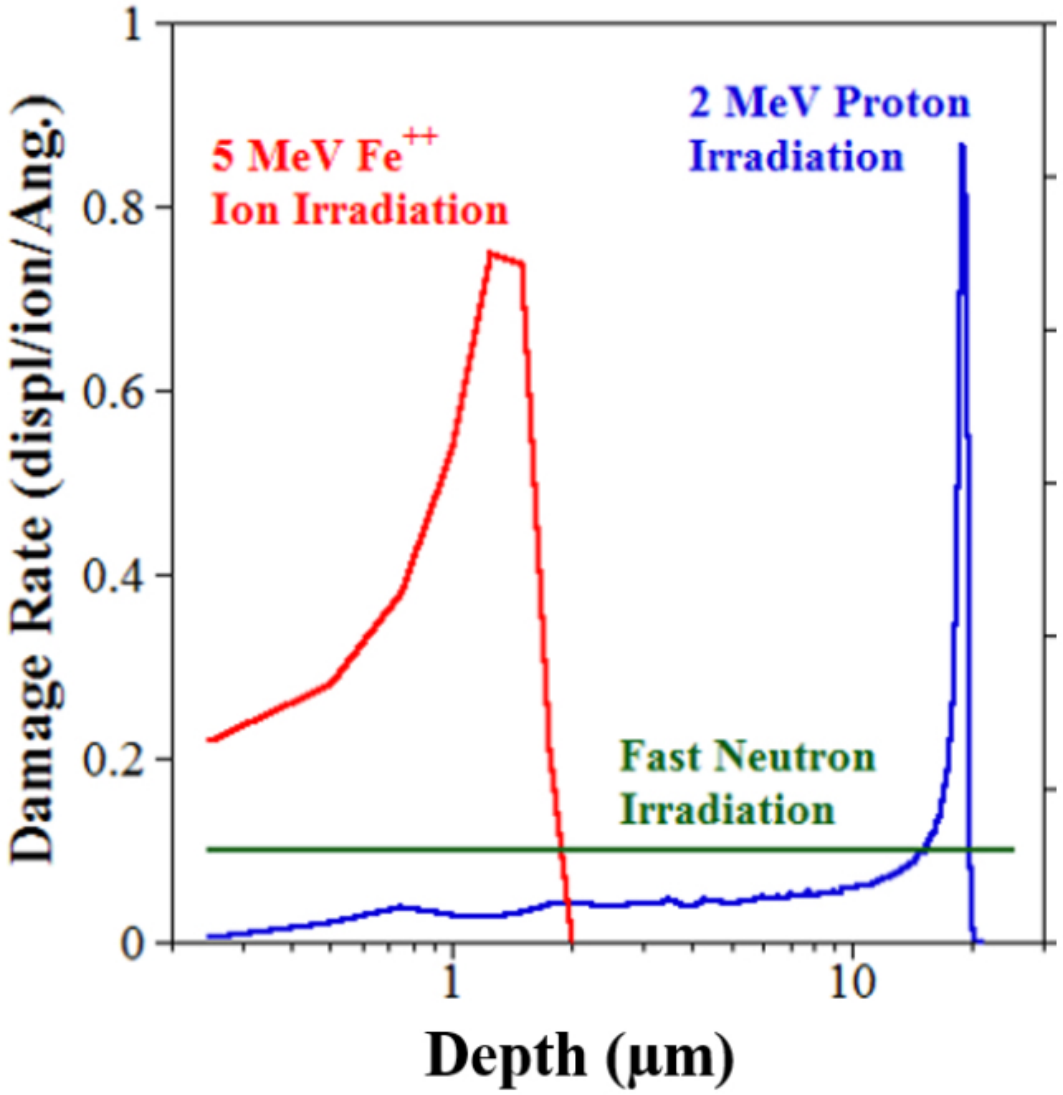

Figure 2.6: Damage Rate (displacements / ion / Å) vs Depth (μm) for 5 MeV Fe^{2+} ion irradiation (red), 2 MeV proton irradiation (blue), and fast neutron irradiation (green) – Adopted from [111]

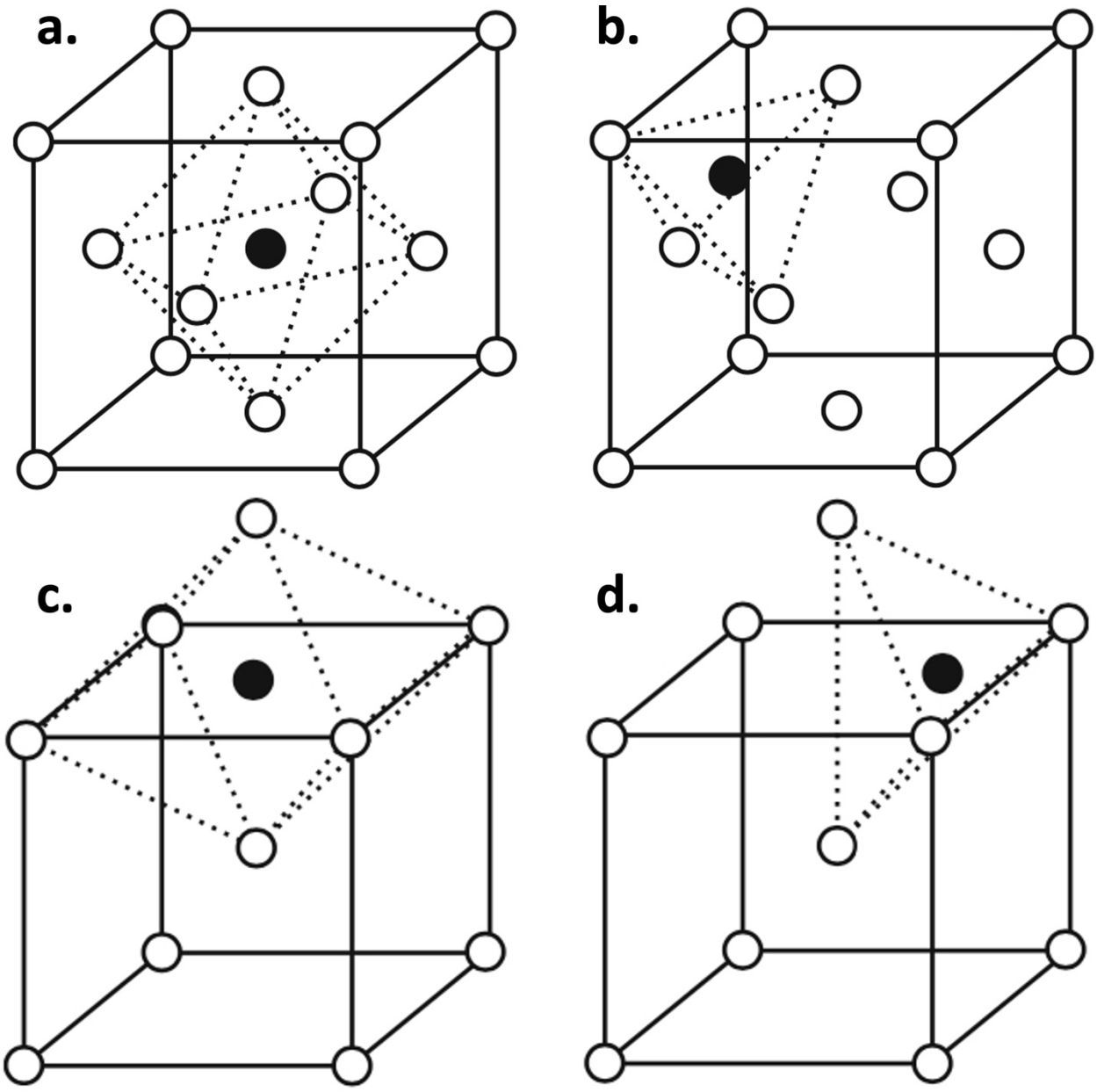

Figure 2.7: Octahedral and tetrahedral interstitial sites for a. and b. FCC, c. and d. BCC – Adopted from [7]

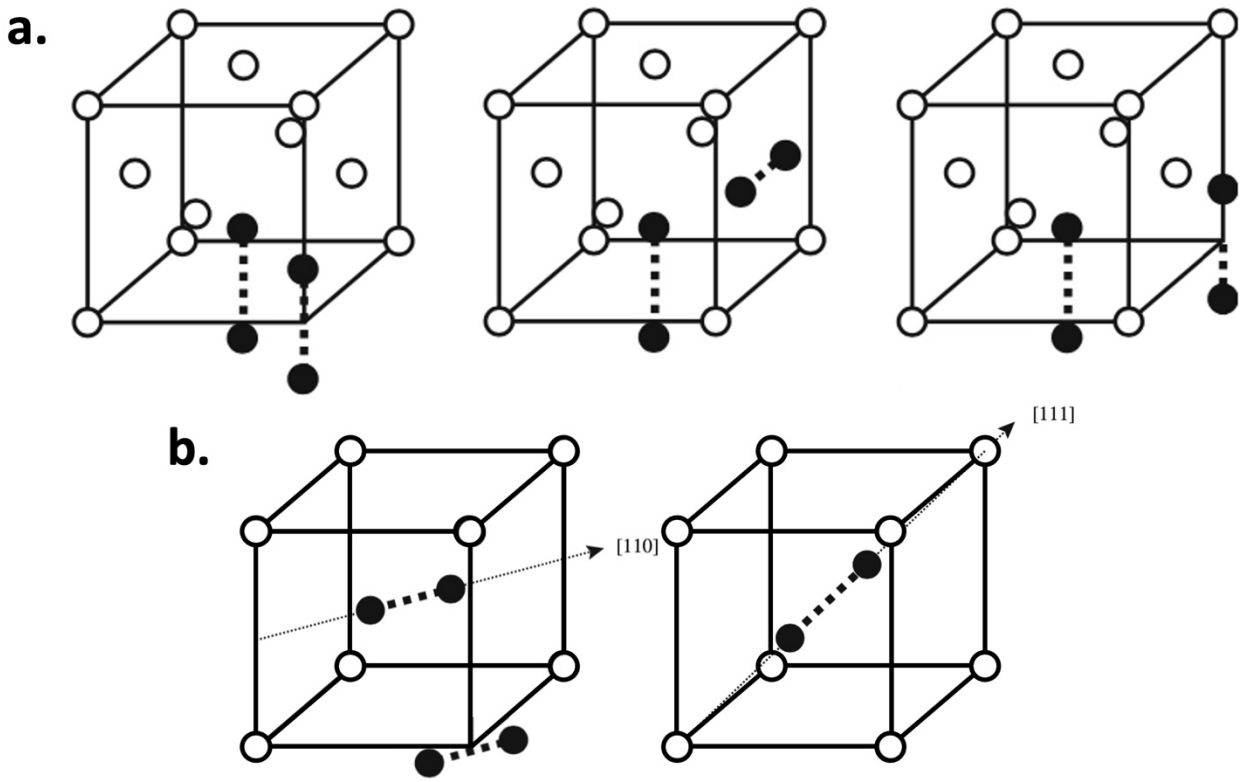

Figure 2.8: Di-interstitial configurations for a. FCC crystal structure and b. BCC crystal structure – Adopted from [7]

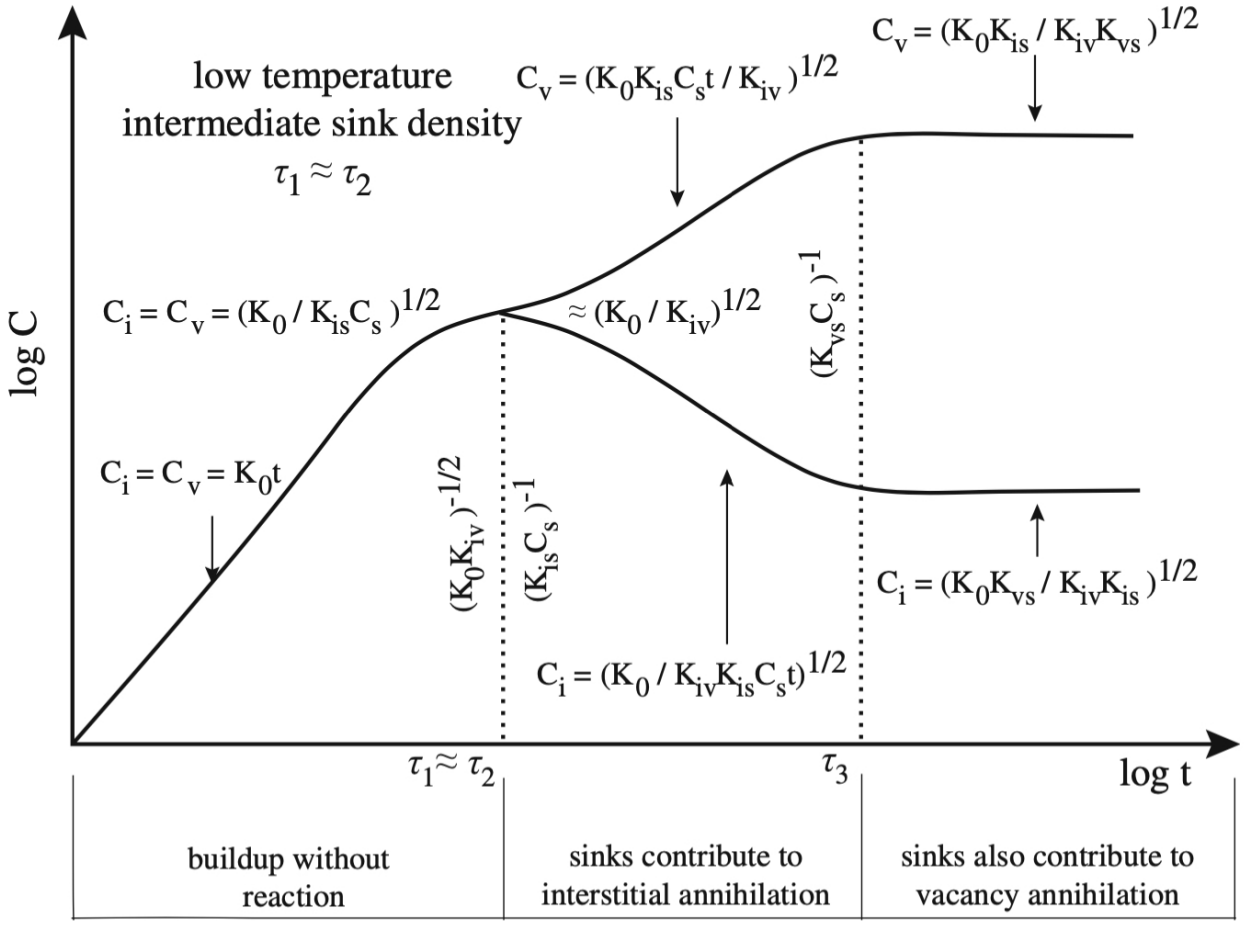

Figure 2.9: Low Temperature / Intermediate sink density Point Defect Concentration vs Time – Adopted from [7]

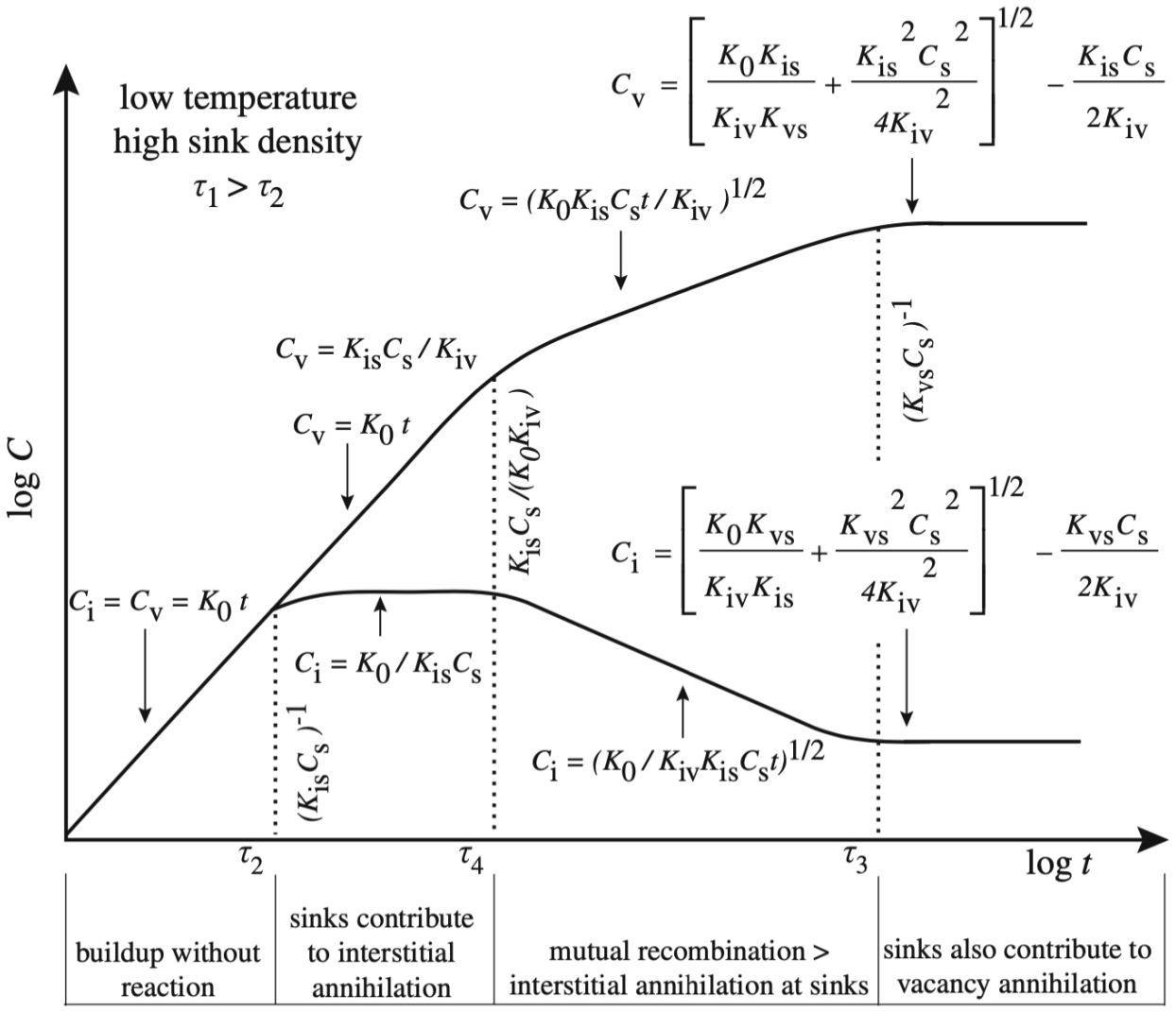

Figure 2.10: Low Temperature / High sink density Point Defect Concentration vs Time – Adopted from [7]

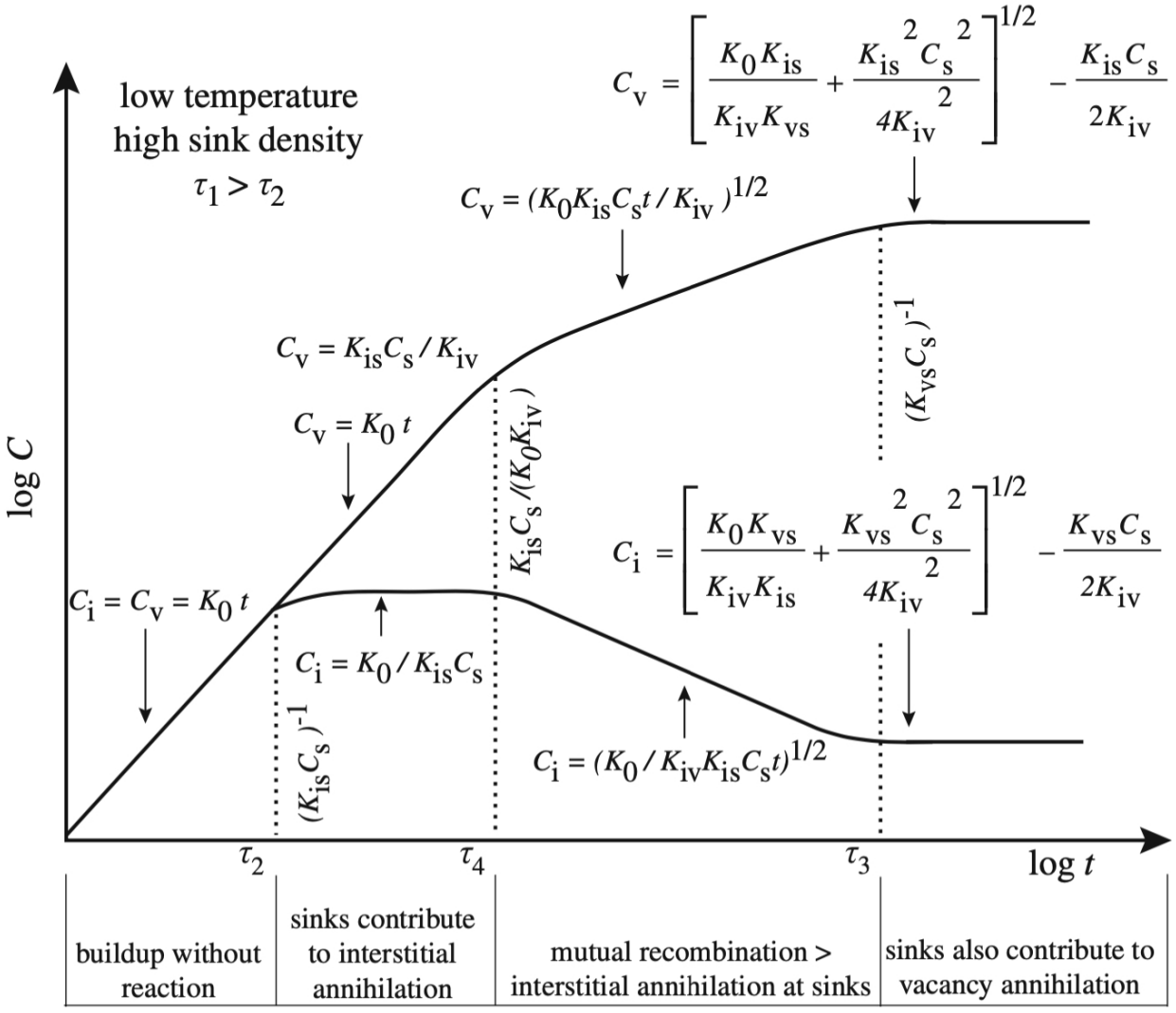

Figure 2.11: RIS vs Temperature for varying dose rates – Adopted from[7]

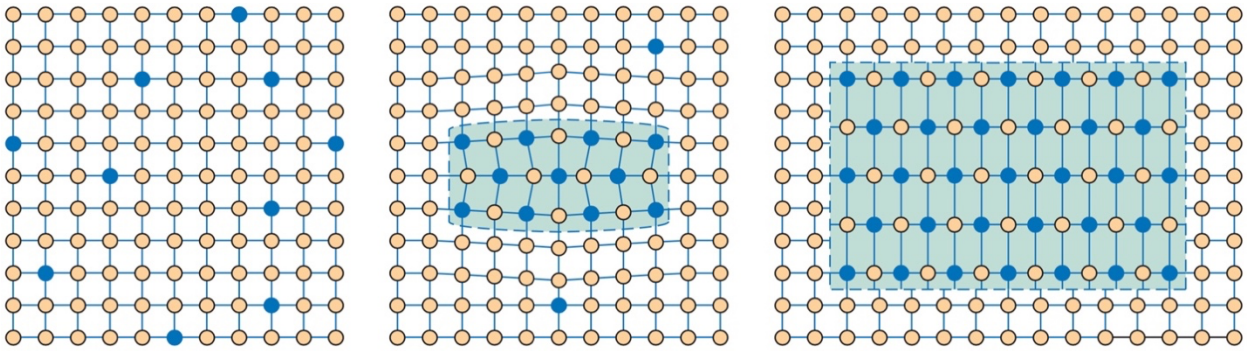

Figure 2.12: a. GP Zone, b. Coherent precipitate, and c. Incoherent precipitate – Adopted from [69]

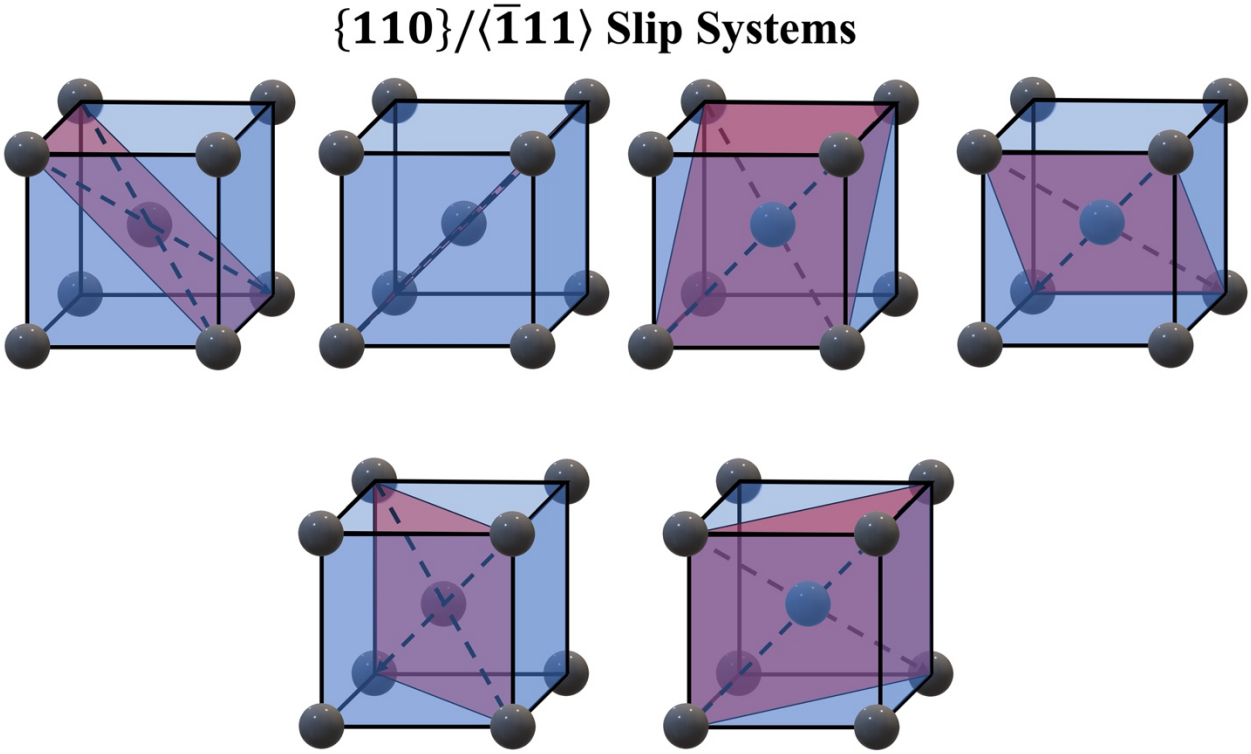

Figure 2.13: BCC {110} / <$\bar{1}$11> Slip Systems

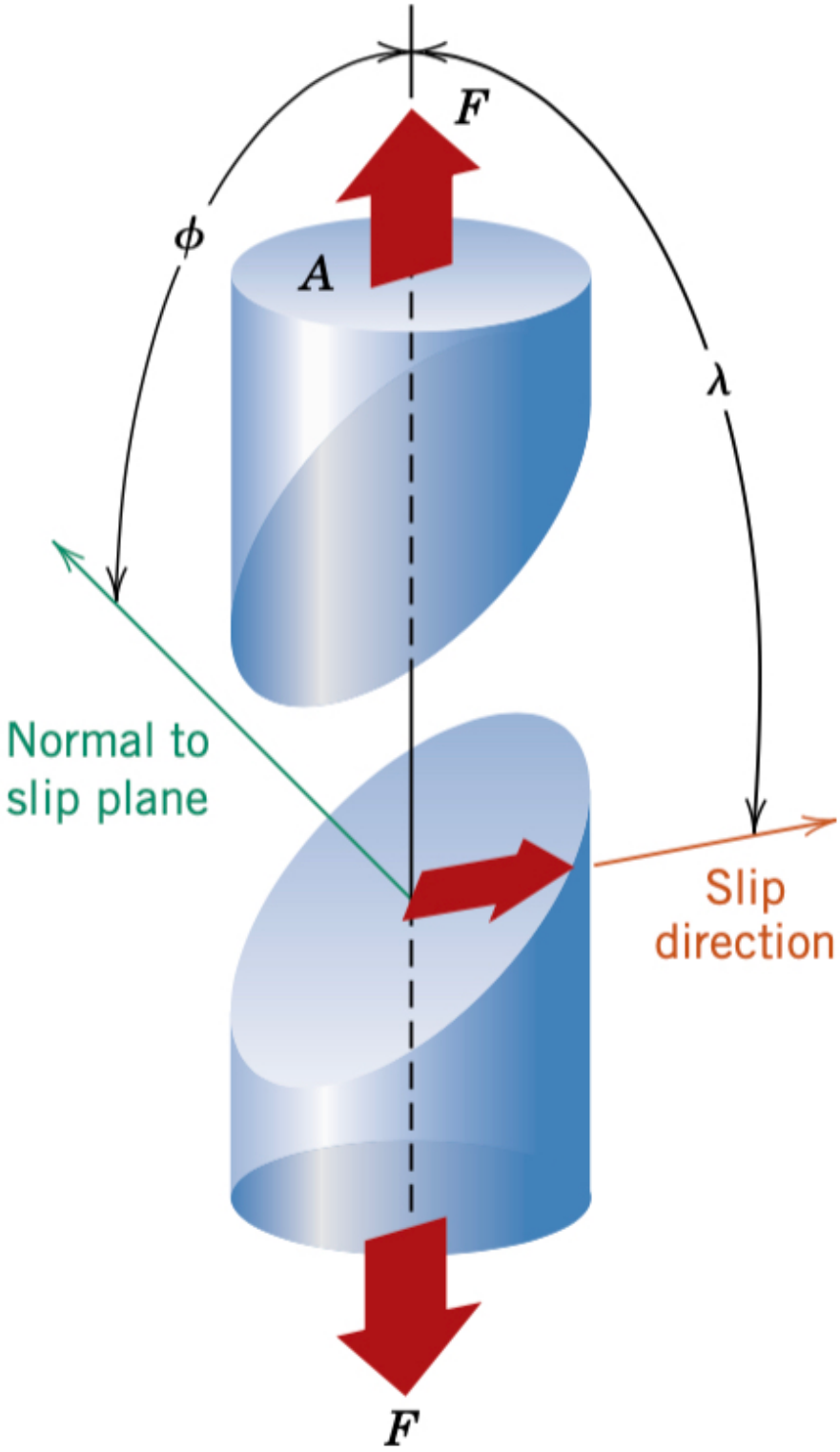

Figure 2.14: Schmid's Law Diagram showing slip plane, slip plane normal direction, slip direction, and stress direction – Adopted from [69]

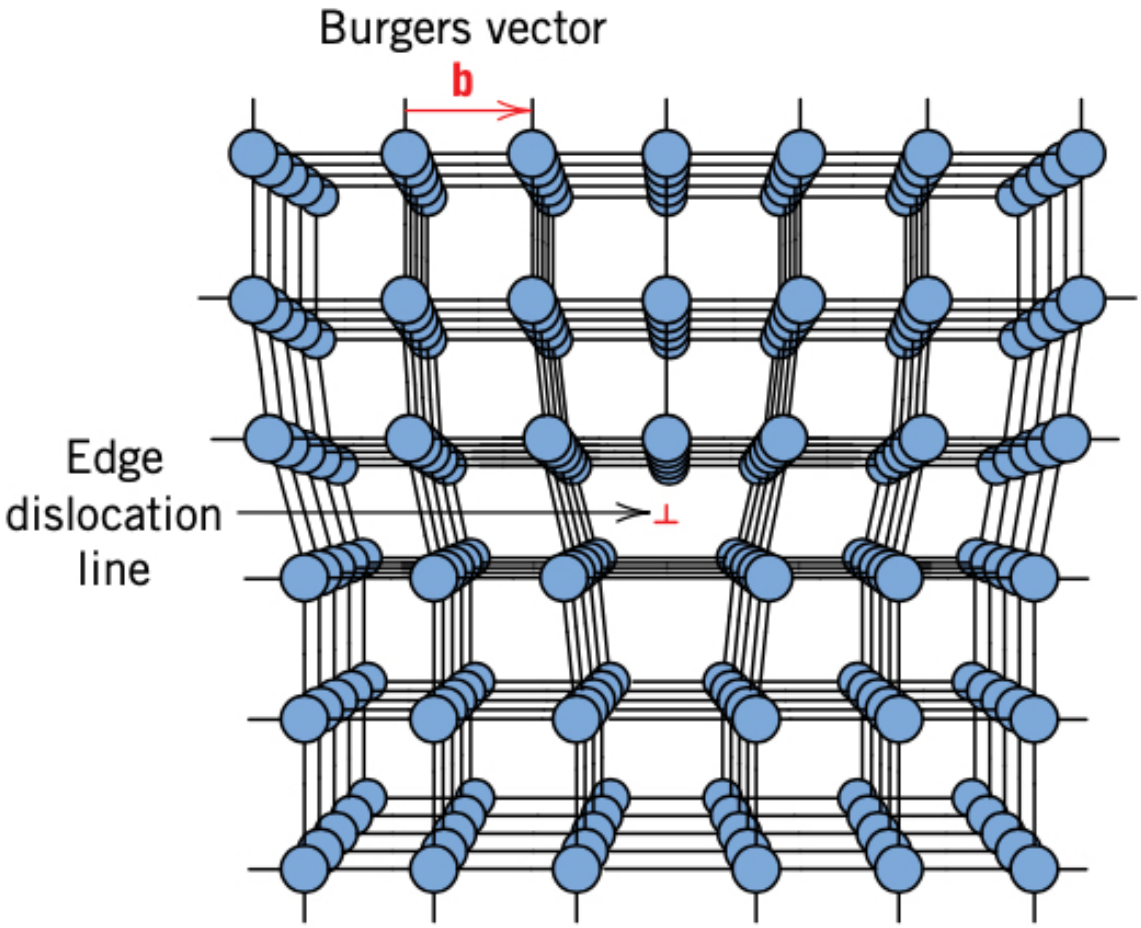

Figure 2.15: Edge dislocation showing Burgers vector direction and slip line direction – Adopted from [69]

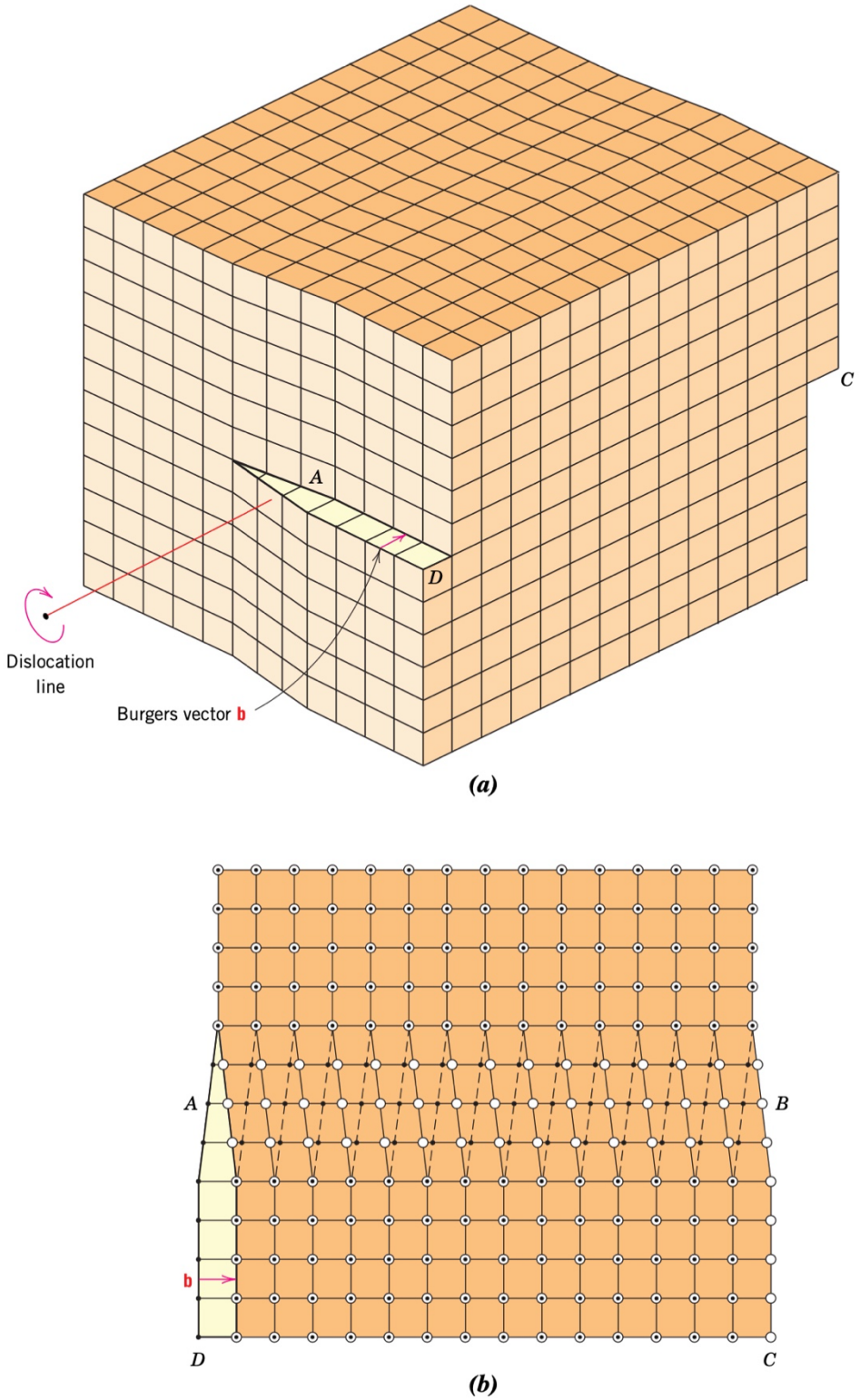

Figure 2.16: Screw dislocation showing Burgers vector direction and dislocation line direction – Adopted from [69]

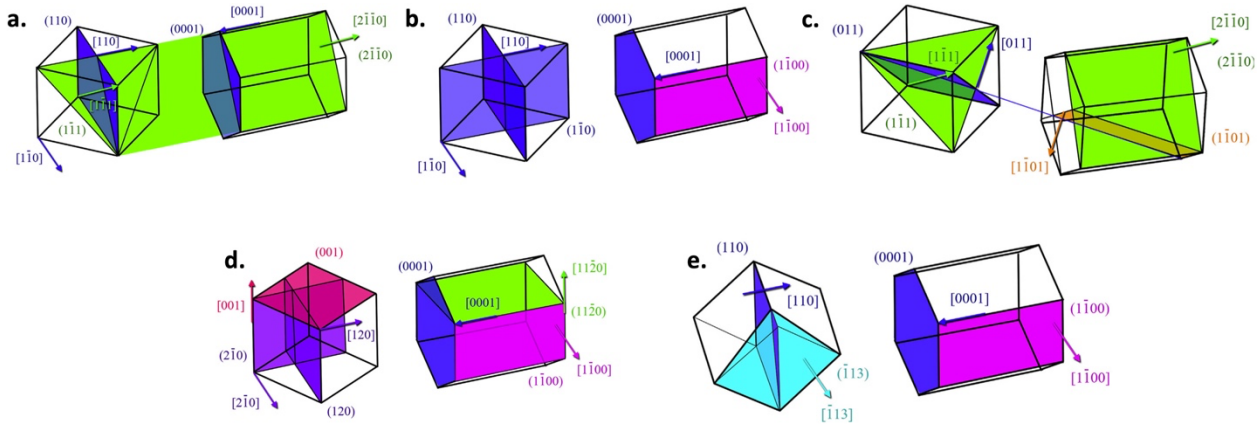

Figure 2.17: BCC to HCP martensitic planar relationships – Adopted from [100]

Table 2.1 BCC / HCP planar relationships

BCC plane	**HCP plane**
(110)	(0001)
$(1\bar{1}1)$	$(2\bar{1}\bar{1}0)$
$(1\bar{1}0)$	$(1\bar{1}00)$
$(\bar{1}13)$	$(1\bar{1}00)$
(001)	$(11\bar{2}0)$

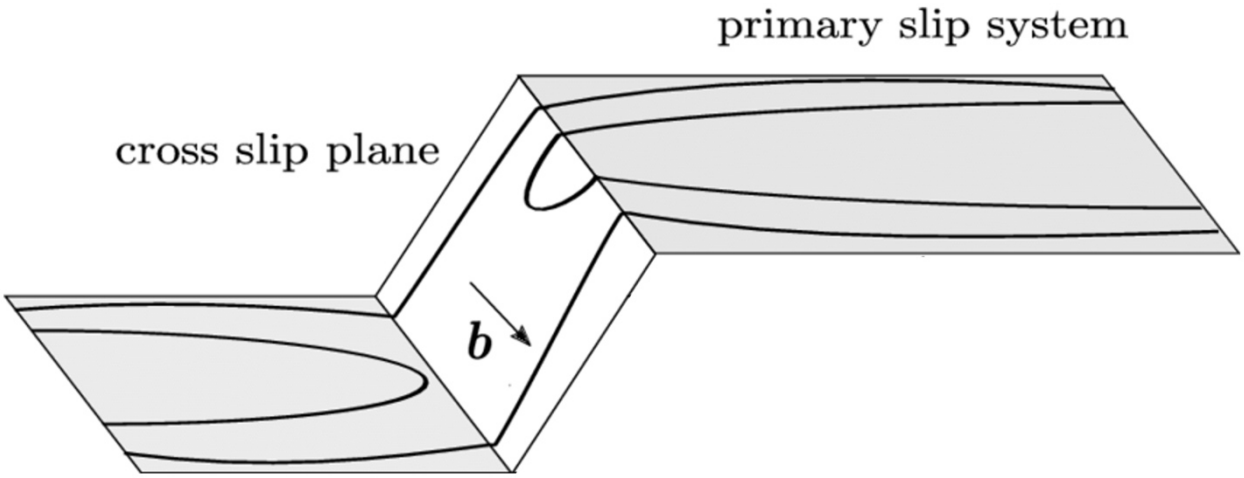

Figure 2.18: Cross slipping dislocation – Adopted from [112]

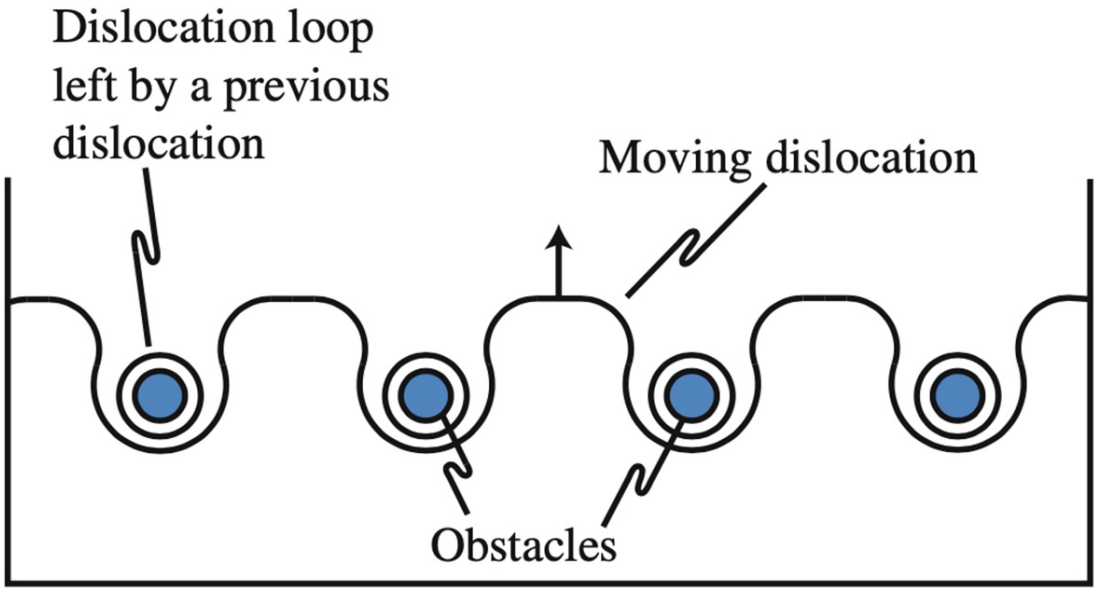

Figure 2.19: Dislocation line approaching obstacles and bowing around them – Adopted from [7]

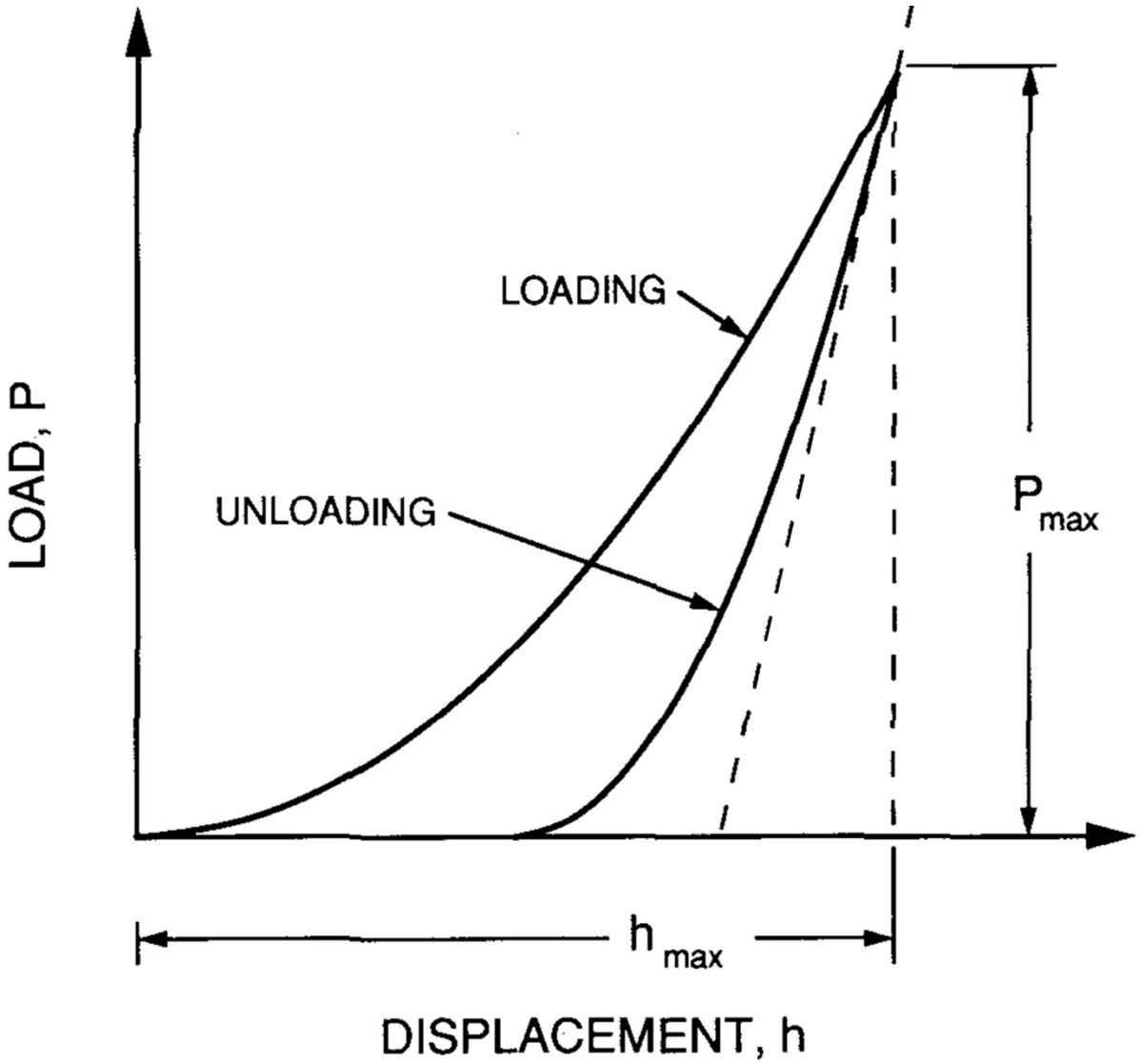

Figure 2.20: Nanoindentation Load vs Displacement – Adopted from [107]

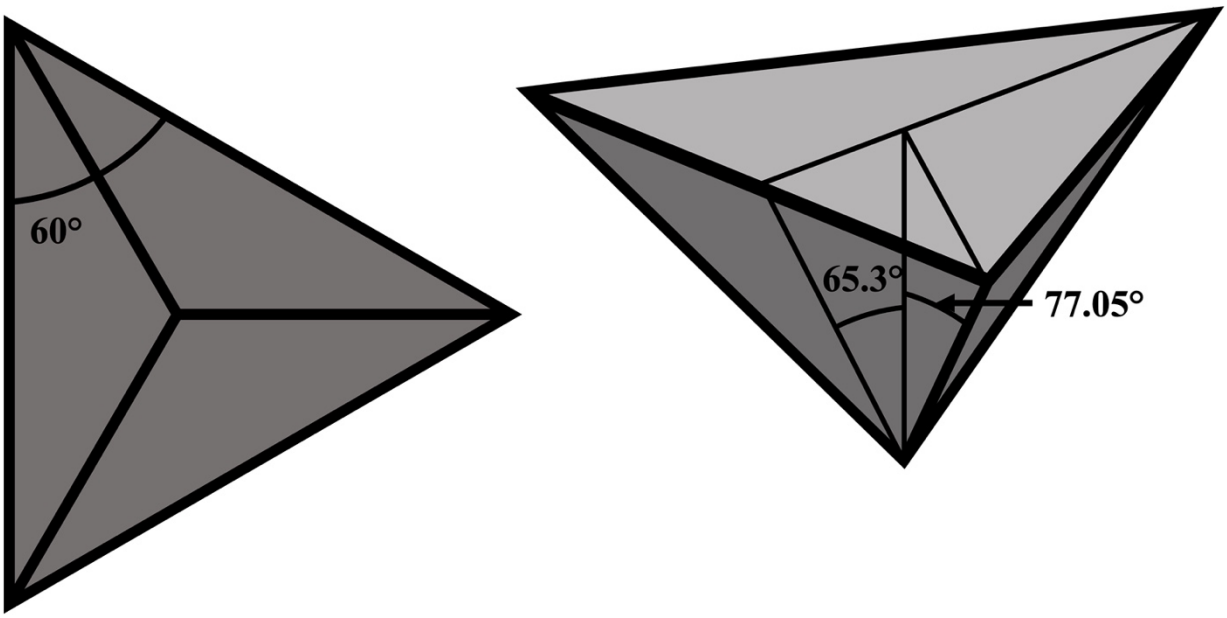

Figure 2.21: Berkovich indenter geometry

3. OBJECTIVE

The objective of this study is to demonstrate the influence of solutes of the oversized substitutional, undersized substitutional, and interstitial solute types, on the irradiated microstructures in three ferritic iron-based model binary alloys including Fe – Cr, Fe – N, and Fe – P. From a broader perspective the aim is to demonstrate how solute misfit effects the resulting defect densities, defect types, and radiation induced segregation behavior in irradiated nuclear reactor structural materials. Furthermore, this study aims to show how the solute influenced irradiated microstructures as well as the solute types effect the mechanical response in each alloy. Lastly, the study aims to demonstrate the importance of controlling for the Berkovich indentation direction in ferritic alloys by showing the change in mechanical response when the indenter is aligned along different crystallographic directions.

The objective will be accomplished through experiments including *ex situ* irradiation, BFSTEM imaging and SAED analysis of Fe – Cr, Fe – N, and Fe - P, *in situ* irradiation and BFTEM imaging of Fe - P, and nanoindentation of Fe – P and Fe - N. Irradiation induced defect densities and solute type will be analyzed quantitatively while solute clustering, crystal orientation, and the existence of multiple phases will be analyzed qualitatively. Mechanical hardness, irradiation hardening, and anisotropy of unirradiated and irradiated Fe - P and Fe – N will be analyzed quantitatively while deformation mechanisms will be analyzed qualitatively. The sub-objectives of each experiment are listed below:

Ex situ Irradiation, BFTEM Imaging and SAED Analysis:

1) Quantify defect densities of Fe – Cr, Fe – N, and Fe – P
2) Observe RIS and solute clustering behavior of Fe – Cr, Fe – N, and Fe – P
3) Identify the solute types by SAED indexing and d space measurement

In situ Irradiation and BFTEM Imaging of Fe - P

1) Observe the defect evolution of Fe – P under irradiation in real time
2) Quantify the defect densities and sizes in two regions of the irradiated Fe – P sample
3) Observed the post irradiation chemical compositions of clusters and irradiation induced phases in two regions of the Fe – P sample

Nanoindentation of Fe – P and Fe – N

1) Quantify the hardening in irradiated Fe – P and Fe – N

2) Relate hardening to irradiated microstructure of Fe – P and Fe – N through dispersed barrier hardening model
3) Observe the deformation mechanisms of unirradiated and irradiated Fe – P and Fe – N through indentation cross section and TEM

4. METHODS

4.1 Bulk Sample Preparation

Three model Fe-*X* (*X* = P, Cr, N) binary alloy buttons were produced by arc melting at Ames Laboratory with P, Cr, and N concentrations of 4.5, 9.5, and 2.3 at% respectively. The arc melted buttons were then cut to 2 mm x 2 mm x 20 mm bars by EDM. Two sets of bars were mechanically polished, one set to be used as an unirradiated reference set of samples and one to be ion irradiated, with silicon carbide paper down to 1200 grit. The samples were then polished with 6 μm and 3 μm diamond slurries and finally vibratory polished with 0.5 μm silica slurry.

Irradiation of the ion irradiated sample set was done at the University of Michigan Ion Beam Laboratory in the Wolverine 3MV tandem particle accelerator with 4.4 MeV Fe^{2+} ions at a temperature of 370 ± 5 °C and dose rate of 7.6 x 10^{-4} dpa/sec. the Stopping Range of Ions in Matter (SRIM) was used to determine the irradiation damage profile. Irradiation parameters were chosen such that a dose of 8.5 dpa would occur at a depth range between 400 nm and 600 nm. This depth was chosen to avoid the strong surface sink at shallower depths and the ion implantation region deeper underneath the surface [111]. Fig 4.1 a. provides the irradiation dose as a function of depth for Fe – P, Fe – Cr, and Fe –N.

4.2 TEM Lamellae Preparation

TEM lamellae for TEM *ex situ* and *in situ* imaging were lifted from each bulk irradiated alloy. A Quanta 3D FEG FEI dual beam (scanning electron microscope) SEM / focused ion beam (FIB) was used to make the initial cuts of the TEM lamella. The SEM / FIB stage was tilted to 52° to perpendicularly align the bulk sample with the FIB beam. A protective platinum strip was deposited at a 52° stage tilt by gas injection system (GIS) platinum deposition on to the surface of the bulk sample with dimensions of X = 10 μm x Y = 2 μm x Z = 4 μm using an accelerating voltage and beam current of 30 kV and 0.1 nA respectively. Trenches were milled, at a 52° stage tilt, on either side of the TEM lamella by rectangular cross section with the dimensions X = 10 μm x Y = 12 μm x Z = 8 μm at an accelerating voltage and beam current of 30 kV and 7 nA respectively. After trenches were milled, finer cleaning cross section cuts were made with the dimensions of X = 10 μm x Y ≤ 2 μm x Z = 5 μm, at stage tilts of 50.5° and 53.5°,

with an accelerating voltage and beam currents of 30 kV, 3 nA and 1 nA respectively, to the lamella to remove the heavy damage of the coarser trench cuts.

After cleaning cross section cuts were completed, the stage was returned to a tilt of 0° and a rectangular cut termed a "J-cut" was made such that the left side and the bottom of the lamella were completely severed from the bulk sample while the right side was partially severed leaving just a small arm attaching the lamella to the bulk sample. After the "J-cut" was made, an Omniprobe micro-manipulator was welded to the lamella using GIS Pt deposition with a beam current of 0.1 nA. After the Omniprobe was welded to the lamella, the small arm on the right side that attached the lamella to the bulk sample was cut which completely severed the lamella from the bulk sample. The lamella was lifted by the Omniprobe away from the bulk sample and the lift out of the lamella was completed.

After lamella lift out, the lamella was welded to the TEM Cu half grid using GIS Pt deposition at a beam current of 0.1 nA. After the sample was welded to the Cu half grid, the lamellae was severed from the Omniprobe and the Omniprobe was removed. The welding of the lamellae to the Cu half grid was also done at a 0° stage tilt. Images of the platinum deposition protective layer, bulk trenching, cleaning cuts, J-cut, lift out, and Cu half grid mounting steps are provided in Fig. 4.2. Yellow and green boxes in Fi. 4.2 are to indicate how FIB deposition (green) and milling (yellow) boxes are places in the image.

After the lamella was mounted to the half grid the stage was tilted back to 52° to return the lamella to a perpendicular orientation with respect to the FIB beam and the lamella was thinned to electron transparent thickness. Thinning of the lamella was done at stage tilts of 50.5° and 53.5° with incrementally decreasing beam currents and Z dimensions. The lamella was thinned with a beam current and Z dimension 1 nA and 2 μm respectively until the lamella was under 1 μm thick. The beam current and Z dimension were reduced to 0.5 nA and 1 μm respectively and the lamella was thinned until it was under 500 nm thick. The beam current and Z dimension were reduced again to 0.3 nA and 500 nm respectively and the lamella was thinned until it was under 250 nm thick. The final thinning step was done at a beam current and Z dimension of 1 nA and 250 nm respectively until the sample was ≤ 100 nm thick.

After the lamella was thinned, it was cleaned to remove any remaining FIB damage. Lamella cleaning was done in two steps. First the stage was tilted to 47° and 59° and the accelerating voltage and beam current were reduced to 5 kV and 48 pA respectively. Rectangular

cuts were done over the entire area of the lamellae for a duration of 4 minutes at both stage tilts. Then the accelerating voltage and beam current were reduced to 2 kV and 27 pA respectively. Rectangular cuts were done again over the entire area of the lamellae for 4 minutes at both stage tilts.

4.3 Microstructure Imaging and Analysis of *ex situ* Irradiated Microstructures

TEM imaging of *ex situ* irradiated microstructures was done in the Microscopy and Characterization Suite (MaCS) at the Center for Advanced Energy Studies (CAES) in Idaho Falls using the FEI Tecnai TF30-FEG STwin TEM. The samples were tilted to the nearest low zone axis (ZA) for imaging. Selected area diffraction (SAED) patterns were collected, and diffraction spot patterns were analyzed to determine crystal structure and orientation. BFSTEM imaging was used to collect images of the irradiated microstructure at a depth range of 400 nm to 600 nm which is indicated by the gray strip in Fig. 1 (a). BFSTEM imaging is advantageous because all dislocation loops can be imaged from one tilt orientation regardless of dislocation loop orientation [113]. This allows for better quantification of dislocation loop densities. Defect density counts, which included dislocation loops and clusters, were done by averaging the densities in four separate images of each sample. The average dislocation loop diameters for each alloy were determined by measuring the major diameters of at least one hundred loops.

Scanning electron microscopy (STEM) EDS was done with a dwell time of five minutes per pixel to produce maps with areas of 0.0056 μm^2 using a Thermo Scientific Themis Z at Birk Nanotechnology Center at Purdue University. These EDS maps have been cropped down to an area of 0.017 μm^2 along with their corresponding reference images

4.4 TEM *in situ* Irradiation Imaging and Analysis

A TEM lamella was extracted from the unirradiated Fe – P bulk sample such that a GB, which was chosen for the intergranular β precipitate within that GB, was situated down the center of the lamella. following the procedure described in section 4.3. TEM *in situ* irradiation was done at the Intermediate Voltage Electron Microscope (IVEM)-Tandem facility at Argonne National Laboratory in Lemont, IL. Prior to the *in situ* irradiation experiment, the sample was first annealed to remove any remaining FIB damage at 400 °C for 10 minutes. Then the sample

was annealed at 430 °C for 10 more minutes. Note that during the 400 °C annealing step no phase change was observed, however, when the sample was annealed at 430 °C there was some precipitate formation along the β precipitate matrix interface which indicates that the 400 °C temperature was not high enough to induce thermally activated phase change. The *in situ* irradiation was done with 1 MeV Kr^{2+} ions at 370 °C to a dose of 10 dpa. The ion energy was chosen to reduce the radiation fluence gradient and to ensure the ion penetration through the thickness of the lamella. The irradiation temperature was chosen for consistency with the *ex situ* Fe^{2+} ion irradiation of the bulk alloys. Imaging and analysis were done in two regions, the Fe-P matrix region and a P depleted α Fe region that was enclosed inside of a Fe_3P β precipitate. These regions will be called the Fe – P matrix region and the α Fe region for the remaining contents of this document. Video imaging was done entirely in the Fe-P matrix and the *in situ* irradiation experiment was paused at 1 dpa, 3 dpa, 6 dpa, and 10 dpa to collect BFTEM images in the α Fe and Fe-P regions. The regions imaged during the experiment are shown in Fig. 4.3. SAED diffraction patterns were also collected from the Fe-P matrix region before the *in situ* irradiation experiment down a [110] ZA and after the experiment down a $[\bar{1}33]$ ZA to produce a better irradiation induced defect imaging condition.

Post-irradiation compositional analysis was done using the Thermo Fisher Scientific Talos F200X S/TEM EDS at the Irradiated Materials Characterization Laboratory (IMCL) at the Idaho National Laboratory (INL) to observe the radiation induced segregation of elements in the α Fe and Fe – P matrix regions. Compositional analysis in these regions included elemental maps which had areas of 0.108 μm^2 and line scans with a 604 pm x 604 pm pixel size and a dwell time of 5 μs across the β precipitate / α Fe interface and across P enriched clusters in the α Fe and Fe-P matrix regions respectively. The EDS scans were done with a 20 μs dwell time and a 302 x 302 pm pixel size. The reference lamella was also cut across a GB that contained an intergranular β precipitate.

Dislocation loops and nano clusters were counted and measured to establish defect densities and sizes respectively in the α Fe and Fe-P matrix regions. All dislocation loops were counted in the α Fe region from one micrograph at each dose since the entire region is contained in the image in the micrographs of each dose. In the Fe-P matrix region no dislocation loops were counted since no obvious or resolvable loops were visible in the micrographs of this region. Instead, nano clusters were counted in several regions of the micrographs of each corresponding

dose and the densities were averaged at each dose. The average diameters of the dislocation loops and clusters from the α Fe and Fe-P matrix regions were determined by measuring the major diameters of at least one hundred dislocation loops and clusters. The fringe separations of Moiré fringes seen forming in both the α Fe and Fe-P matrix regions were measured at doses of 6 dpa and 10 dpa.

EDS maps with areas of 0.387 μm^2 and lines scans both done with dwell times and pixel sizes of 5 μs and 604 pm x 604 pm respectively were also collected from an unirradiated representative reference lamella for comparison using the Thermo Fisher Scientific Talos F200X S/TEM EDS at the IMCL at the Idaho National Laboratory (INL) as well.

4.5 Nanoindentation and Indentation Cross Sectional TEM Lamellae Imaging

Berkovich nanoindentations were done using the Hysitron TI950 TriboIndenter in the MaCS laboratory at CAES in Idaho Falls, ID. Displacement rate controlled nanoindentation 5 x 4 indentation arrays with a separation distance of 20 μm and a displacement rate and an indentation depth of 5 nm/s and 1000 nm respectively were done in the unirradiated and irradiated Fe – P and Fe - N alloys.

Grains with (001) orientation were located using an energy dispersive analysis X-ray (EDAX) electron backscatter diffraction (EBSD) detector in the Quanta 3D FEG SEM / FIB dual beam at the MaCs laboratory at CAES in Idaho Falls. The GBs were then outlined by FIB for identification during nanoindentation. Displacement rate controlled nanoindentations were done in (001) grains in unirradiated and irradiated Fe – P and Fe – N bulk alloys with a displacement rate and indentation depth of 2 nm/s and 1000 nm respectively. Indentations were done with Berkovich nanoindenter tip vertex directed along <001> and <011> directions. Images of the EBSD maps, outlined grain SEM images, and indentation directions are provided in Fig. 4.4. A larger diagram of the indentation lamellae with an oblique perspective of the lamella is provided in Fig. 4.5 (a) and (b) respectively. The indentation orientations, directions, irradiation condition, and alloys are identified in Table 4.1. After the indentations were made, TEM indentation cross sectional lamellae were cut using the procedure outlined in section 2.2 with modified lamella dimensions to allow for the imaging of the large plastic region underneath the indentation. The lamellae were cut along the <001> and <011> directed vertices in each indent. For the following, the unirradiated (001) / <001> Fe – P and unirradiated (001) / <011> Fe – P will be referred to as

unirradiated <001> Fe – P and unirradiated <011> Fe – P respectively. The unirradiated (001) / <001> Fe – N and the unirradiated (001) / <011> Fe – N will be referred to as unirradiated <001> Fe – N and unirradiated <011> Fe – N respectively. Irradiated (001) / <001> Fe – P and irradiated (001) / <001> Fe – N will be referred to as irradiated Fe – P and irradiated Fe – N respectively.

Samples were imaged using down ZA BFSTEM in the FEI Tecnai TF30-FEG STwin TEM in the MaCS laboratory at CAES in Idaho Falls, ID. Samples were tilted to the nearest low ZA and SAED patterns were collected to verify the sample orientations. The plastic zones of each sample were then imaged to observe the deformation mechanisms

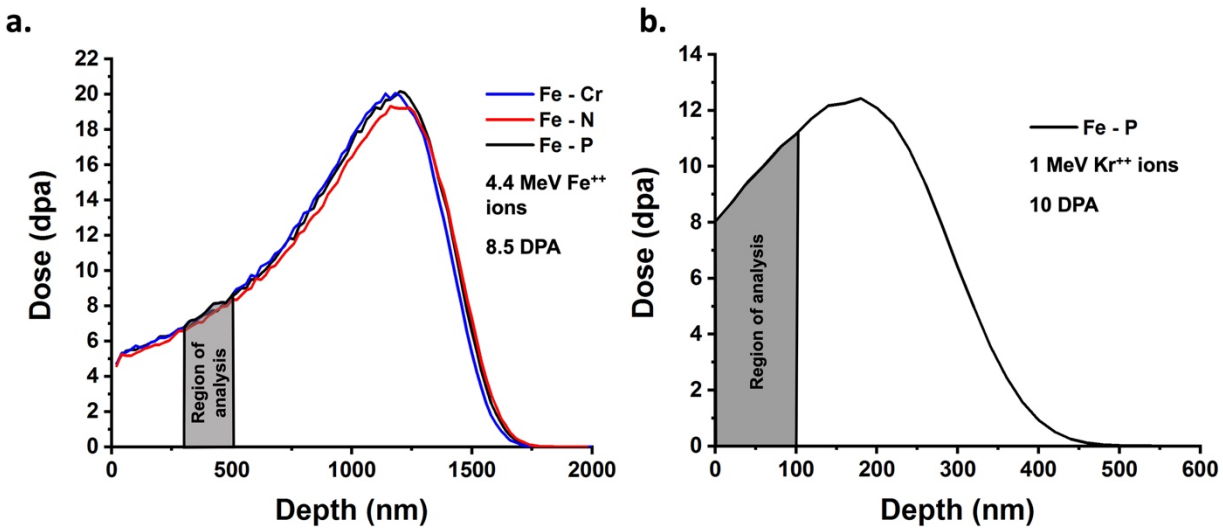

Figure 4.1: SRIM Dose (dpa) vs Depth (nm) profiles with region of interest indicated in gray for (a) Fe-*X* (*X* = Cr (blue), N (red), and P (black) irradiated with 4.4 MeV Fe^{2+} ions and (b) Fe-P irradiated with 1 MeV Kr^{2+} ions with region of interest indicated in gray

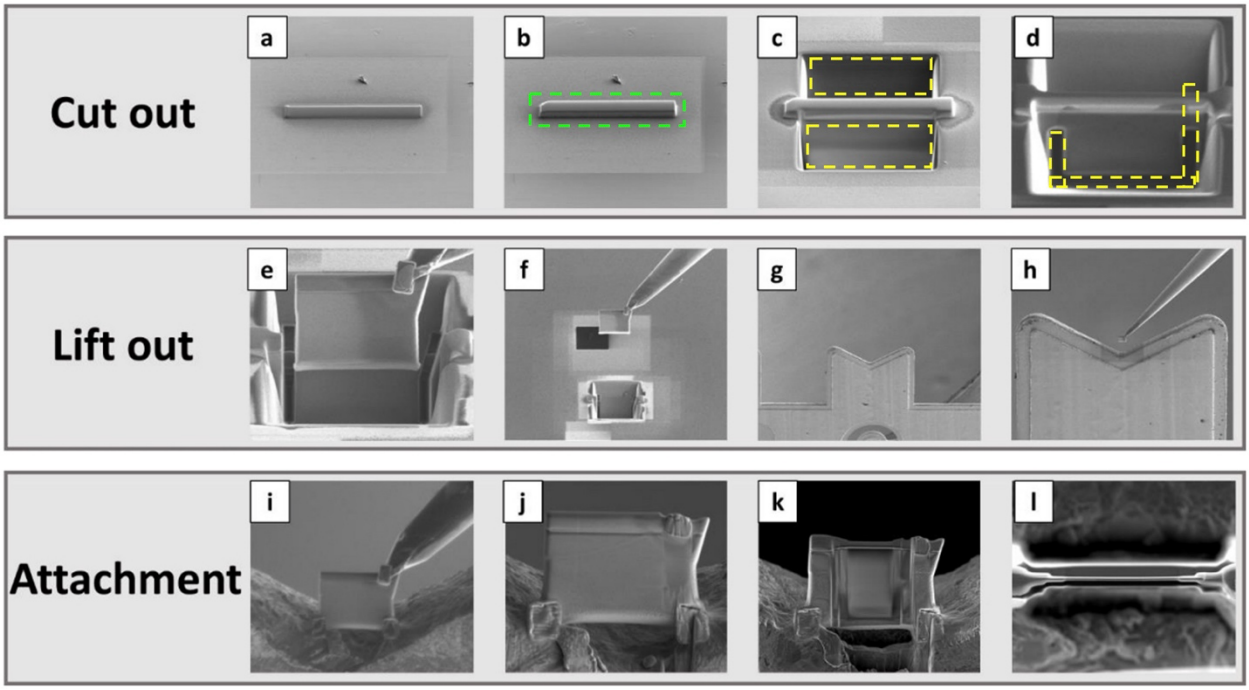
Cut out
a
b
c
d
Lift out
e
f
g
h
Attachment
i
j
k
l

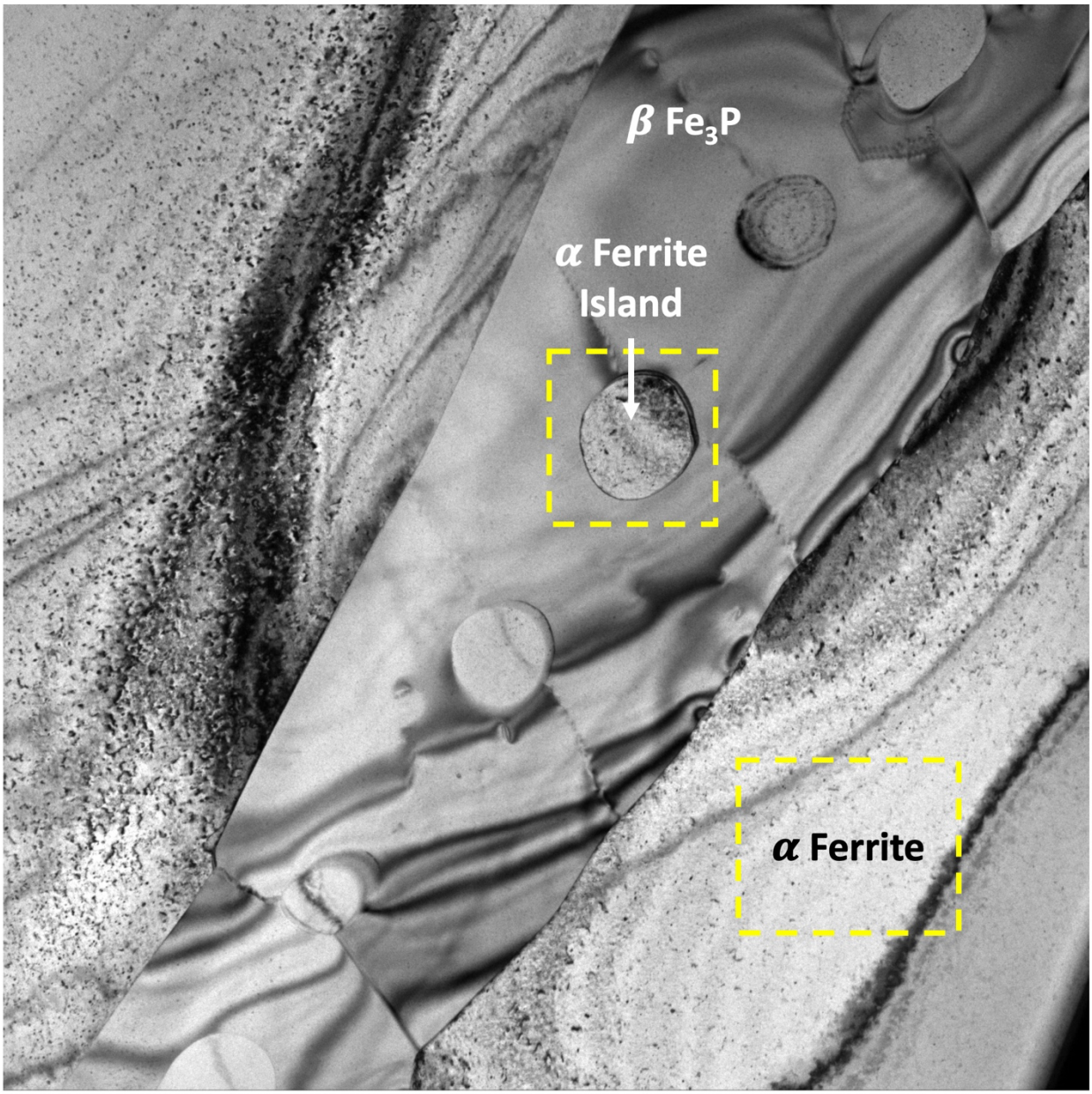

Figure 4.2: TEM *in situ* irradiated lamella showing the analyzed regions in yellow dotted boxes and the β Fe_3P precipitate identified in white text

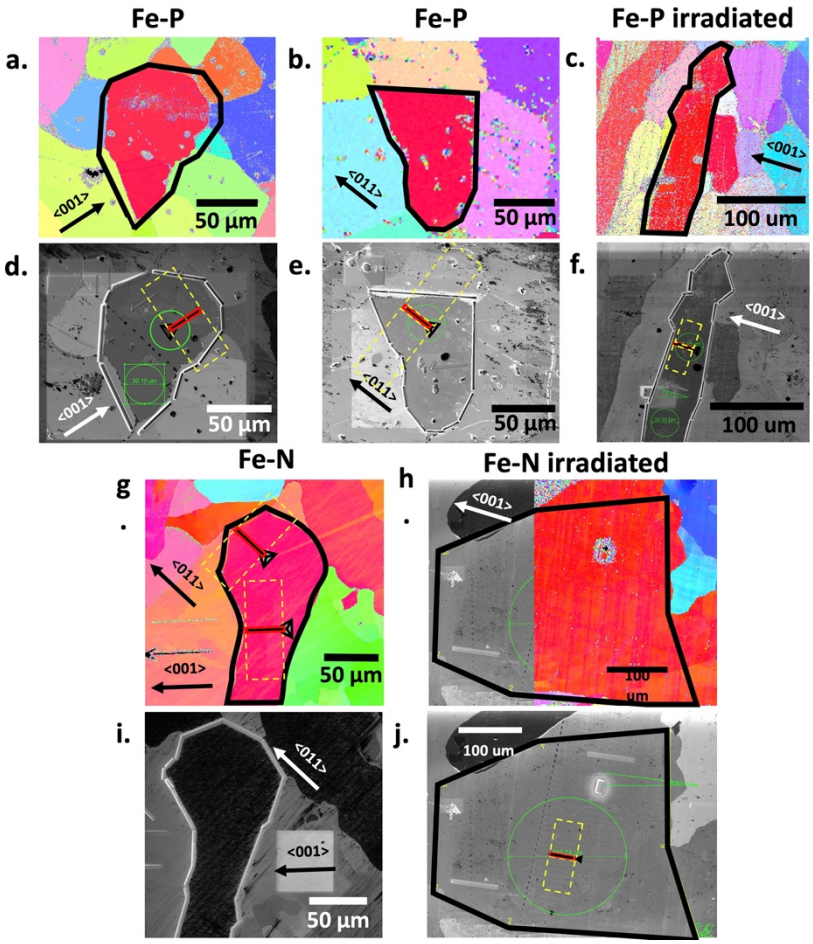

Figure 4.3: (a – c) EBSD maps for Fe - P and irradiated Fe - P respectively with chosen grain (black border), indentation sites (diagramed in grain), and indentation directions (arrow and indices) indicated, (d – f) SEM images of grain indentation locations for Fe – P and irradiated Fe – P respectively, (g – h) EBSD maps for Fe – N and irradiated Fe - N with selected grain (black border), indentation site (diagramed in grain), and indentation direction (arrow and indices), and (i – j) SEM images of indentation locations for Fe – N and irradiated Fe - N

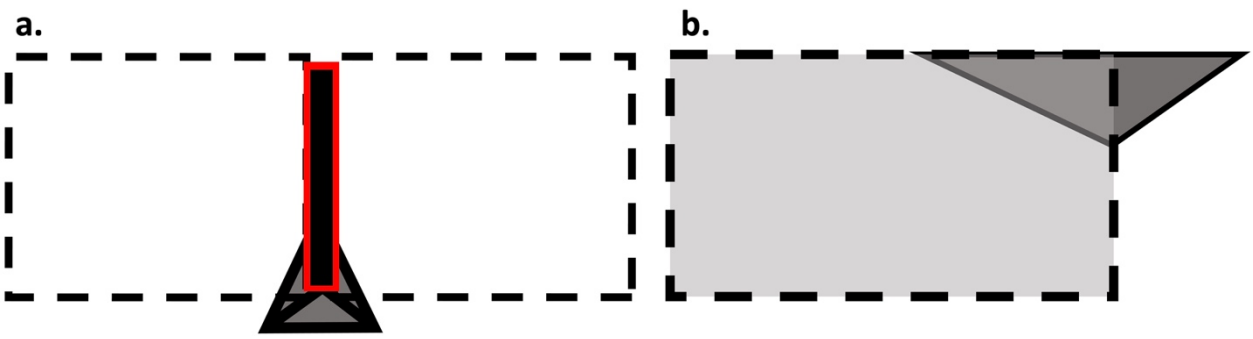

Figure 4.4: Diagrams of nanoindentation TEM cross sectional lamella showing a. top-down perspective with indentation, trenches (black dotted boxes), and lamella (black rectangle red outline), and b. oblique perspective with lamella area (outlined by black dotted box)

Table 4.1 Nanoindentation Cross Sectional Lamellae Conditions

Fe – P		**Fe - N**	
Unirradiated	**Irradiated**	**Unirradiated**	**Irradiated**
(001) / <001>	(001) / <001>	(001) / <001>	(001) / <001>
(001) / <011>	X	(001) / <011>	X

5. RESULTS

5.1 Irradiated Microstructure Characterization

5.1.1 Phases and Determination of Solute Type

The EBSD maps of the Fe-Cr, Fe-P, and Fe-N alloys, Fig. 5.1, provide evidence of the presence or lack of precipitates in each alloy. The EBSD maps of the Fe-Cr and Fe-N alloys, Fig. 5.1 (a) and (b) do not show any indication of precipitates, however, intergranular Fe_3P β precipitates are seen in the Fe-P alloy and are indicated by black dotted borders in Fig. 5.1 (c)

SAED patterns, which are inset on the images in Fig. 5.2 (a), (b), and (c) were collected for the Fe-Cr, Fe-N, and Fe-P alloys and the lattice parameters of each alloy were determined using the relationship between d spacing and lattice parameter provided in Eq. 5.1.

$$d = \frac{a}{\sqrt{h^2+k^2+l^2}} \qquad \text{Equation 5.1}$$

where d is d spacing measured in the SAED pattern, a is the lattice parameter, and h, k, and l, the miller indices [114]. The lattice parameter for the Fe-Cr, Fe-N, and Fe-P alloys are 2.95 Å, 2.95 Å, and 2.9 Å respectively. The lattice spacing measurement was used to determine the nature of the solute atom, specifically whether these solutes are oversized substitutions, undersized substitutions, or interstitial solutes. Each of the lattice parameters is larger than the accepted α Fe value of 2.87 Å [69]. Generally, it would be expected that oversized substitutional atoms and interstitials would result in a lattice expansion, so the Fe-Cr and Fe-N solutes are believed to be oversized substitutional and interstitial type. An undersized substitutional solute is expected to produce a lattice contraction, but the Fe-P alloy is believed to be an undersized substitutional solute even though the Fe-P lattice parameter is larger than the accepted lattice parameter value of α Fe because the measured lattice parameter is smaller than the lattice parameter of the Fe-N alloy. P is a larger atom than N and if P was interstitial, it would produce a larger lattice expansion than N would, but the Fe-P lattice parameter is smaller than the Fe-N lattice parameter. The larger lattice parameter of the Fe-P alloy in comparison to the accepted value of α Fe is attributed to the variations associated with measurements made in different instruments.

5.1.2 *Ex situ* Irradiation Defect Characterization

The irradiated microstructures of the Fe – Cr and Fe – N alloys, Fig. 5.2 (a) and (b) respectively, are comprised primarily of dislocation loops and dislocation lines while the irradiated microstructure of the Fe – P alloy is comprised primarily of small clusters and irradiation induced precipitates. Defect densities, size distributions, and average sizes, which include only dislocation loops and clusters, were determined by counting and measuring defects in at least four separate locations of each sample and provided graphically in Fig. 5.3 (a) and (b). One hundred defects were measured in the determination of average defect size and distribution. The irradiated Fe – Cr alloy has a defect density of 1.59×10^{22} m^{-3} which is 73% smaller than the defect density of the irradiated Fe – P alloy and 61% larger than the defect density of the irradiated Fe – N alloy. The irradiated Fe – Cr average defect size is 6.7 ± 3.1 nm. The irradiated Fe – N alloy has a defect density of 9.85×10^{21} m^{-3} which is almost an order of magnitude smaller than the defect density of the irradiated Fe – P alloy. The irradiated Fe – N average defect size is 7.8 ± 3.3 nm. The irradiated Fe – P alloy has the largest defect density, 6×10^{22} m^{-3}, and smallest average defect size, 5.3 ± 1.5nm, of the three alloys. The standard deviations, ± 3.1 nm and ± 3.3 nm, and the skew of the Fe – Cr and Fe – N size distributions respectively are similar to each other and twice that of the Fe – P size distribution. The Fe – P distribution is also less skewed. The distributions, specifically the differences between the Fe – P alloy and the other two alloys, may provide evidence of the difference in defect type and growth mechanisms. The Fe – P alloy also has irradiated induced precipitates, seen as small Moiré fringes [114,115] and indicated by yellow arrows in Fig. 5.2 (d). The density of the irradiation induced precipitates is 2.25×10^{21} m^{-3}. The sizes of the precipitates, which were determined by measuring the diameters of the moiré fringes, ranged between 5 – 8 nm in size. Evidence of these irradiation induced precipitates is also evident in the SAED pattern of the irradiated Fe – P alloy. Faint rings are seen in the Fe – P SAED pattern and are not observed in the SAED patterns of the other two alloys. Generally, rings indicate polycrystallinity [114] but since these patterns were collected from a single crystal the rings in the irradiated Fe – P SAED pattern are believed to be a result of the polycrystallinity of the irradiation induced precipitates.

The compositions of the irradiated regions in the Fe – Cr, Fe – N and Fe – P samples were also determined by STEM EDS. The Fe – Cr, and Fe – N EDS maps, Fig. 5.4 (a – c) and (d – f), show no indication of solute clustering or segregation while the Fe – P alloy maps, Fig. 5.4

(h – i), have many P rich clusters that correspond to dark shaded defects, indicated by yellow dotted circles in Fig. 5.4 (g) and (i).

5.1.3 TEM *in situ* Irradiation of α Fe and Fe – P

The evolution of irradiation induced defects in the Fe – P alloy were investigated further through TEM *in situ* irradiation. Two regions, an α Fe phase fully contained inside a Fe_3P β precipitate and the Fe – P matrix, were imaged after irradiation to 1 dpa, 3 dpa, 6 dpa, and 10 dpa. These regions of interest are indicated by yellow dotted boxes and white text in Fig. 4.3. The defect evolution and morphologies are notably different in the two regions. The defects in the α Fe region, shown in Fig. 5.5 (a – h), are comprised of dislocation loops and irradiation induced precipitates. Dislocation loops are indicated by red, blue and yellow boxes, and precipitates are indicated by black dotted circles. The dislocation loops evolved in three ways, they are seen growing at subsequent doses, they are seen migrating to the sample surface and then being removed at the sample surface, and they are seen merging with each other. Red numbered boxes with the same number at two different doses indicate a dislocation loop that has grown from one does to a later dose. Yellow numbered boxes with the same number indicate a dislocation loop that has migrated to the sample surface from one dose to a later dose. Blue numbered boxes with the same number indicate dislocation loops that have merged with each other to form larger dislocation loops. Irradiation induced precipitates, which are seen forming by 3 dpa, are indicated by black dotted boxes. The dislocation loops exhibited typical coarsening behavior as they decreased in density from 3.71 x 10^{21} m^{-3} at 1 dpa to 2.53 x 10^{21} m^{-3} at 10 dpa and increased in size from 14.84 nm ± 7.91 nm to 21.66 ± 8.88 nm over the same dose range. This coarsening behavior is shown the Dislocation loop density / diameter vs dose graph in Fig. 5.5 (i). Estimated dislocation loop density and size trend lines have been added to these graphs.

The irradiation induced precipitates grew from 3 dpa to 10 dpa. The moiré fringe separations of the precipitates also increased from 6 dpa to 10 dpa as shown in Fig. 5.6 (a – d), which is an indication that the precipitates are progressing from coherent precipitates to incoherent precipitates [114]. The reference images and EDS maps of the irradiated α Fe, Fig. 5.6 (e – h), and the unirradiated α Fe, Fig. 5.6 (i – l), indicate that irradiation causes C segregation, and that when the local C concentration is high enough, the C rich region transitions

into a C rich precipitate. The maps also show that the α Fe region is rich in Fe and low in P content while the Fe_3P β phase is rich in P and low in Fe content. No P enrichment of the defects in the α Fe region is observed, likely because of the lack of P content in this region.

The irradiated microstructure of the Fe – P region, shown in Fig. 5.7 (a – h), is significantly different than the α Fe region. The defects of the Fe – P region are comprised primarily of P enriched nano clusters, shown in the high magnification images in Fig. 5.7 (c) and (d), and irradiation induced precipitates that formed by 6 dpa, indicated by yellow dotted circles in the high magnification images in Fig. 5.7 (g) and (h). The yellow dotted circles in the 1 dpa and 3 dpa high magnification images show examples of irradiation induced nano clusters and the yellow dotted circles in the 6 dpa and 10 dpa high magnification images provide examples of irradiation induced precipitates.

The EDS maps of the unirradiated and irradiated Fe – P region, which are provided in Fig. 5.8 (a – d) and (e – h) respectively, demonstrate P enrichment of the nano clusters and C enrichment of the larger moiré fringe region. The P clusters are also the same size as the small moiré fringe spots in the reference image in Fig. 5.8 (e) which indicates that the high local P concentration is such that a P rich precipitate is forming. Fig 5.8 (i – l) show line scans and line scan compositional profiles of the unirradiated and irradiated Fe – P region. The line scan of the unirradiated Fe – P show that the P is more uniformly dispersed with smaller pockets of P clustering while the line scan of the irradiated Fe – P show a more coarse dispersion of P. Fig. 5.8 (m) provides the moiré fringe spacing distribution at 6 dpa (red) and 10 dpa (blue). The fringe spacing shifts to larger spacings from 6 dpa to 10 dpa and the distribution spread at 10 dpa is larger than the spread at 6 dpa indicating fringe spacing is increasing as the dose increases and that while preexisting precipitates continue to evolve (right tail of 10 dpa fringe space distribution), new precipitates are forming as well (left tail of 10 dpa fringe space distribution). Small fringe spacing may indicate a closer match between the precipitate lattice and the matrix lattice [114] so the increase in fringe spacing from 6 dpa to 10 dpa indicates precipitates are progressing from coherent precipitates to incoherent precipitates.

5.2 Nanoindentation of Fe – P and Fe – N

5.2.1 Irradiation Hardening

Berkovich nanoindentation was done in the unirradiated and irradiated Fe – P and Fe – N single crystals and cross-sectional lamellae were cut from each indentation to evaluate the irradiation hardening and to observe the deformation mechanisms in these two alloys. The Fe – Cr alloy was excluded because the fine grain structure of the Fe – Cr alloy did not allow for single crystal indentation. Furthermore, orientation specific indents were done in each alloy to evaluate the dependence of hardness on indentation direction and to ensure that the differences in mechanical responses are not due to variations from indentation direction dependence.

The irradiation hardening in the Fe – P alloy is evident in the load vs displacement profile in Fig. 5.9 (a). A study by R. Kasada et al. demonstrated a new method for determining irradiation hardening by Berkovich nanoindentation of ion irradiated ferritic alloys. The study determined the irradiation hardening of the alloy by calculating the difference in hardness between the irradiated alloy and the unirradiated alloy at a depth which avoided the surface sink and the ion implanted region [116]. Irradiation hardening in the current study has been determined in the same way. First the loads of the of the unirradiated and irradiated alloy were converted to Berkovich hardness using Eqs. 2.19 and 2.20 from section 3.3.4. Berkovich hardness was converted to Vickers hardness using Eq. 2.21 in section 3.3.4. The hardnesses of both irradiated and unirradiated alloys were converted to yield strengths by Eq. 2.22 and the difference in yield, i.e. the irradiation hardening, was determined by subtracting the calculated yield strengths of the unirradiated and irradiated indentations at the depth of 500 nm, as this depth was the depth of microstructural analysis and avoids both the surface sink and the ion implantation zone. An expected value for dispersed barrier hardening was then determined by Eq. 2.17 in section 3.3.3. The Fe – P defect density of 6 x 10^{22} m^{-3}, the average Fe – P defect size of 5.3 nm, and an obstacle strength coefficient, α, of 0.1 for weak obstacles such as clusters and small dislocation loops [104,105], were used in the calculation. Hardness for the unirradiated and irradiated Fe – P and Fe – N as well as expected and experimental irradiation hardening values are provided in Table 5.1. The expected irradiation hardening value, determined by the dispersed barrier model equation in Eq. 2.17, was 111 MPa which was 17.6% higher than the experimental value of 91.39 MPa, which was determined by the method introduced by R Kasada

et al. The discrepancy between the expected and the experimental values is likely due to the influence of the substrate since the plastic zone of the indentation may penetrate beneath the irradiated layer at this depth per Eq. 2.23 in section 3.3.5 which will make the irradiated indentation lower and result in a lower experimental hardening value.

The Fe – N alloy also exhibited irradiation hardening. with an experimental irradiation hardening value of 45.97 MPa which was 15.72 % smaller than the expected irradiation hardening value of 54.54 MPa and less than half the experimental irradiation hardening of the Fe – P alloy. The large difference in irradiation hardening between the Fe – P and the Fe – N is expected since the defect density of the irradiated Fe – P, 6 x 10^{22} m^{-3}, is almost an order of magnitude higher than the defect density of the irradiated Fe – N.

The irradiation hardening is also evident in the indentation cross sections of the unirradiated and irradiated Fe – P and Fe – N samples. The heavily deformed region inside the ion irradiated zone of the irradiated Fe – P has an area of 2.66 μm^2, Fig. 5.10 (a), 19.9% smaller than the area of the heavily deformed region of the unirradiated <001> Fe – P, Fig. 5.10 (c) which is 3.19 μm^2. The irradiated Fe – N has a heavily deformed plastic zone area of 3.13 μm^2, Fig. 5.10 (d), which is 1.9% smaller than the area of the heavily deformed region in the unirradiated <001> Fe – N which is 3.13 μm^2, Fig. 5.10 (f). The red dotted borders in Fig. 5.10 (a), (c), (d), and (f) outline the boarders of the heavily deformed region in each sample. Some indentation cross-sections include more of the indentation than others do so the images in Fig. 5.10 have been cropped to show the equivalent location in each indentation cross section. Measurement of the area of the heavily deformed plastic zone is done down to 1.5 μm beneath the surface in each sample, as that is the depth of the irradiated layer in the irradiated Fe – P sample, and 1.4 μm horizontally from the tip of the indent in each sample.

The difference in size of the plastic zones of the irradiation Fe – P and irradiated Fe – N, Fig. 5.10 (a) and (d) respectively, implies a harder response in the irradiated Fe – P than in the irradiated Fe – N which is demonstrated in the load vs displacement and hardness results as well. The resistance to slip, which is the fundamental mechanism of hardening is demonstrated in the higher magnification images of the irradiated zones in the irradiated Fe – P and Fe – N indentation cross sections in Fig. 5.10 (b) and (e) respectively. The red dotted boxes in Fig. 5.10 (a) and (d) identify the location from which the images were taken. Fig. 5.10 (b) shows no discrete dislocations which implies that any dislocation slip is completely prevented by the

defects in the irradiated zone of the irradiated Fe – P sample while several discrete dislocations can be seen in the irradiated zone of the irradiated Fe – N indentation cross section. Some of these dislocations are identified by red dotted circles in Fig. 5.10 (e).

5.2.2 Schmid Factor Values

Stress is assumed to be normal to the facets, the edges, and the tip of the Berkovich nanoindenter. Fig. 5.11 (a) and (b) provide 3D and top-down diagrams indenter stress directions. The Schmid factors have been calculated from these stress directions along primary BCC slip systems for the <001> and <011> indentation directions. Table 5.2 provides the Schmid factors for each stress direction / slip system combination for the <001> and <011> indentation directions. The Schmid factor combined average of the three facets for the <011> indentation direction is 0.246 which is larger than the Schmid factor combined average of the three facets for the <001> of 0.236. The Schmid factor combined average of the edges for the <011> direction is 0.276 which is slightly larger than the Schmid factor combined average of 0.275. A larger Schmid factor implies that a larger portion of the applied stress will be felt along a given slip system, so it will require less applied stress to trigger yield in a slip system with a highe Schmid factor. There are four edge 1 Schmid factors in the <001> indentation direction which are equivalent. This may explain the prevalence of cross slip in the unirradiated and irradiated <001> Fe – P indentation cross section, Fig. 5.12 (a), as cross slip is facilitated by a high number of slip systems with similar Schmid factors [117]. The $(\bar{1}\bar{1}0)$ / $[\bar{1}1\bar{1}]$ slip plane has a Facet 1 Schmid factor of 0.5 in the <011> indentation direction. The $(\bar{1}\bar{1}0)$ plane intersects the (011) plane along the $[\bar{1}1\bar{1}]$ direction so slip along that direction would be visible in the (011) sample as it is in the unirradiated <011> Fe – P cross section in Fig. 5.12 (b).

5.2.3 (001) / <001> Fe – P Indentation

The primary deformation mechanism for the unirradiated and irradiated <001> Fe – P samples is cross slip. As Deusbery et al. explains, slip systems must have similar Schmid factors in order for cross slip to occur between those two slip systems [117]. Cross slip in the <001> Fe – P samples is evident in the TEM cross sections in Fig. 5.12 (a) and (e). Many bowing dislocations, indicated by white dotted line in Fig. 5.12 (a), are seen in both images. There are

four slip systems with equivalent Schmid factors along edge 1 stress direction, the edge that is visible in the <001> Fe – P TEM lamellae as shown in Table 5.1. Furthermore, those Schmid factors, all 0.367 are relatively high and slip would occur readily in any of those slip systems. The entire plastic zone, which is the zone which has a dislocation density significantly above zero and indicated by the blue dotted line in Fig. 5.12 (e), of the irradiated <001> Fe – P is larger than the plastic of the unirradiated <001> Fe – P, Fig. 5.12 (a), which is unexpected since the plastic zone of a harder sample should be smaller than that of a softer sample per [118]. The larger size of the irradiated <001> Fe – P plastic zone may be due to the hard irradiated layer pressing down substrate instead of the indenter.

The unirradiated <001> Fe – P sample, with a max load of ~84,000 μN, is harder than the unirradiated <011> Fe – P sample which has a max load of ~78,900 μN. Fig. 5.9 (c) provides the load vs displacement profiles of the unirradiated <001> Fe – P (red) and unirradiated <011> Fe – P (green). The harder response of the unirradiated <001> Fe – P sample is likely due to the lower average Schmid factors of the <001> indentation direction, Table 5.1. The average Schmid factors along the <001> indentation direction are all either lower or equal to the average Schmid factors of the <011> indentation direction. This implies that a larger applied load will be required in the <001> indentation direction to produce an equivalent shear stress in a given slip system and to trigger yield along that slip system [69].

The unirradiated and irradiated <001> Fe – P samples are also harder than the unirradiated and irradiated <001> Fe – N samples respectively. Typically, solid solution hardening is greater for interstitial solutes than for substitutional solutes per M. Swenson et al. [104], so the difference in hardness between Fe – P and Fe – N is unexpected and must be related to different deformation mechanisms in the two alloys. The difference in deformation mechanisms is evident in the TEM cross sections of the Fe – P and Fe – N samples. Furthermore, the load vs displacement profiles of the Fe – P show no load drops while the Fe – N load vs displacement profiles have many load drops.

5.2.4 (001) / <011> Fe – P Indentation

The primary deformation mechanism in the unirradiated <011> Fe – P sample is pure slip along (011) / <111> slip systems. Fig. 5.12 (b) shows many linear dislocations, indicated by yellow and white dotted lines, directed along <111> directions in {001} plane which is the plane

of the lamella. There are several facet 1, facet 2, and edge 1 Schmid factors along $[\bar{1}1\bar{1}]$ and $[\bar{1}\bar{1}1]$ directions that are maximized or nearly maximized including. This includes the facet 1 / $(110)/[\bar{1}1\bar{1}]$ Schmid factor of 0.5, the edge 1 /$(110)/[\bar{1}1\bar{1}]$ Schmid factor of 0.43, the facet 2 / $(10\bar{1})/[\bar{1}1\bar{1}]$ Schmid factor of 0.5 and the edge 1 / $(10\bar{1})/[\bar{1}1\bar{1}]$ Schmid factor of 0.43. Facets 1 and 2 and edge 1 are highlighted here because these are the stress directions that are visible in unirradiated <011> Fe – P indentation cross section.

The unirradiated <011> Fe – P, with a max load of ~78,900 μN, is softer than the unirradiated <001> Fe – P which has a max load of 84,000 μN but harder than the unirradiated <011> Fe – N which has a max load of ~46,300 μN. As discussed in section 5.2.3, the softer response in the unirradiated <011> Fe – P sample is likely due to the higher average Schmid factors in this indentation direction. The higher Schmid factors will result in more shear stress concentrated along the primary slip systems which means a lower applied stress is required to activate those slip systems [69].

The unirradiated <011> Fe – P is also harder than the Fe – N samples. Similar to the explanation in section 5.2.3, the solute hardening of interstitial solutes is expected to be more than that of the solute hardening for substitutional solutes [104], as such the excess hardening of the Fe – P alloy over the Fe – N alloy is likely due to a difference in deformation mechanism between the Fe – P and Fe – N alloys. Additionally, the unirradiated <011> Fe – P load vs displacement profile did not exhibit load drops while the unirradiated <011> Fe – N load vs displacement profile has many load drops.

5.2.5 (001) / <001> Fe – N

There are two visible deformation mechanisms in the unirradiated and irradiated <001> Fe – N samples, cross slip and stress induced HCP martensitic phase transformation. Cross slip in the unirradiated and irradiated <001> Fe – N samples is likely facilitated by the four equivalent edge 1 Schmid factors in the <001> direction, similar to the reasoning behind cross slip <001> Fe – P samples.

The stress induced HCP martensitic phase transformation is evident in the unirradiated and irradiated <001> Fe – N TEM indentation cross sections, Fig. 5.12 (c) and (f). Many martensitic lathes, indicated by yellow dotted circles in Fig. 5.12 (c) and (f), have <001>

directional preference which is indicated by white and yellow dotted lines in Fig. 5.12 (c) and (f). A higher magnification images of the martensitic lathes in both unirradiated and irradiated <001> Fe – N samples, Fig 5.13 (a) and (c), show the moiré fringes resulting from the lattices of the BCC and HCP phases. The inset SAED pattern of the irradiated <001> Fe – N sample, Fig. 5.13 (c), shows the primary $(011)_{bcc}$ pattern and the satellite spots of the $(0\bar{1}10)_{hcp}$ pattern which contrasted with the unirradiated <001> Fe – N sample.

The many load drops, which are known to occur during a stress induced martensitic transformation [119–121], in the unirradiated and irradiated <001> Fe – N load vs displacement profiles, Fig 5.9 (b), provide further evidence of the stress induced martensitic phase transformation. Furthermore, a "pop out" event, indicated by a black dotted line in Fig. 5.9 (b), is seen in the irradiated <001> Fe – N load vs displacement profile and is also known to occur during stress induced martensitic transformations [121,122] when some of the transformation is reversible. The stress induced martensitic phase transformation does however seem to be inhibited by the irradiated layer in the irradiated <001> Fe – N sample, as no martensitic lathes are seen in the irradiation damaged zone of the irradiated <001> Fe – N. Instead, many small defects which may be dislocations are seen aligned along the same <001> directions. Fig. 5.14 provides a high magnification BFSTEM image of these vertically and horizontally aligned defects which are indicated by red dotted circles.

The unirradiated <001> Fe - N Lath size vs Distance from indentation plot in Fig. 5.15 (a) indicates that the size of these lathes increased slightly with increasing distance from the indentation site while the irradiated <001> Fe – N Defect size vs Distance from indentation plot in Fig. 5.15 (c) shows that lathe size decreases with distance to the indentation site and there is a stronger relationship than the relationship of the unirradiated <001> Fe – N from Fig. 5.15 (a). A closer look at the micrograph provided in Fig 5.15 (a) and Fig. 5.12 (c) reveals that the largest lathes are closest to the indentation site and that a large number of small lathes close to the indentation site decreased the overall average lathe size near the indentation site which is the likely reason for the positive lathe size / indentation site distance relationship.

5.2.6 (001) / <011> Fe – N

There are two visible deformation mechanisms in the unirradiated <011> Fe – N sample, pure slip along primary slip systems, as indicated the yellow and white dotted lines in Fig. 5.12

(d), and stress induced HCP martensitic phase transformation. Martensitic lathes, which for the most part are aligned along horizontal <001> directions, are indicated by yellow dotted circles in Fig. 5.12 (d). Vertically aligned martensitic lathes are not seen in the unirradiated <011> Fe – N sample. Instead, many vertically aligned wider darkly shaded defects are seen as indicated by red dotted circles in Fig. 5.12 (d). Horizontally aligned lathes are also smaller than the lathes in the unirradiated <001> Fe – N sample as indicated by the Lathe size vs Distance to indentation site plot in Fig. 5.15 (b). The smaller size of the horizontally aligned lathes as well as the lack of vertically aligned lathes that appear to have been replaced by these wide dark shaded defects is likely a product of the perspective from which these lathes are being viewed. If the [001] viewing direction is more normal to the lathes than the [011] viewing direction, they will appear larger from the [001] viewing perspective. Additionally, if horizontally aligned martensite planes are more in plane with the (011) plane, they will appear as wide dark shaded defects as seen in Fig. 5.12 (d). Similarly, if the martensite planes are more normal to the (001) plane they will appear as narrow lathe as seen in Fig. 5.12 (c) and (f). A higher magnification image of a unirradiated <011> Fe – N lathe and a SAED pattern from the lathe, Fig. 5.13 (b), provides further evidence that there are in fact more than one crystal structure. Moiré fringes are seen in the martensite lathe in Fig. 5.13 (b). Furthermore, in addition to the primary $(011)_{bcc}$ spots in the SAED pattern inset in Fig 5.13 (b), the $(0\bar{1}10)_{hcp}$ martensite satellite spots are also seen. The load drops in the unirradiated <011> Fe – N load vs displacement profile also provides further evidence of the stress induced martensitic phase transformation.

The unirradiated <011> Fe – N sample is the softest as demonstrated by the max load in the unirradiated <011> Fe – N load vs displacement profile in Fig. 5.9 (d). The softer response of the <011> indentation direction, as discussed in section 5.2.4, is likely due to the higher average Schmid factors of the <011> direction. As discussed previously, the higher Schmid factor means more stress is concentrated along a given slip system and a lower applied stress will be required to activate that slip system thus the yield of the material will be lower.

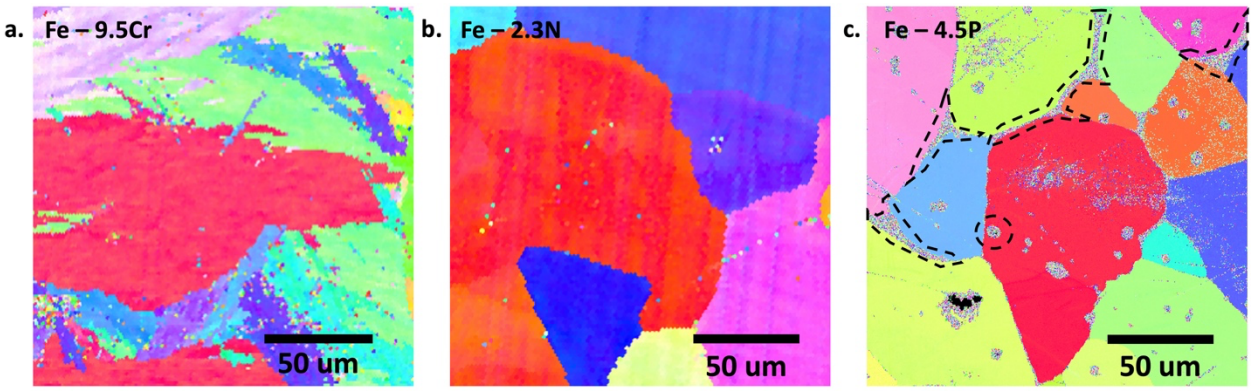

Figure 5.1: EBSD maps of (a) Fe-Cr, (b) Fe-N, and (c) Fe-P with precipitate phases indicated by black dotted boarders

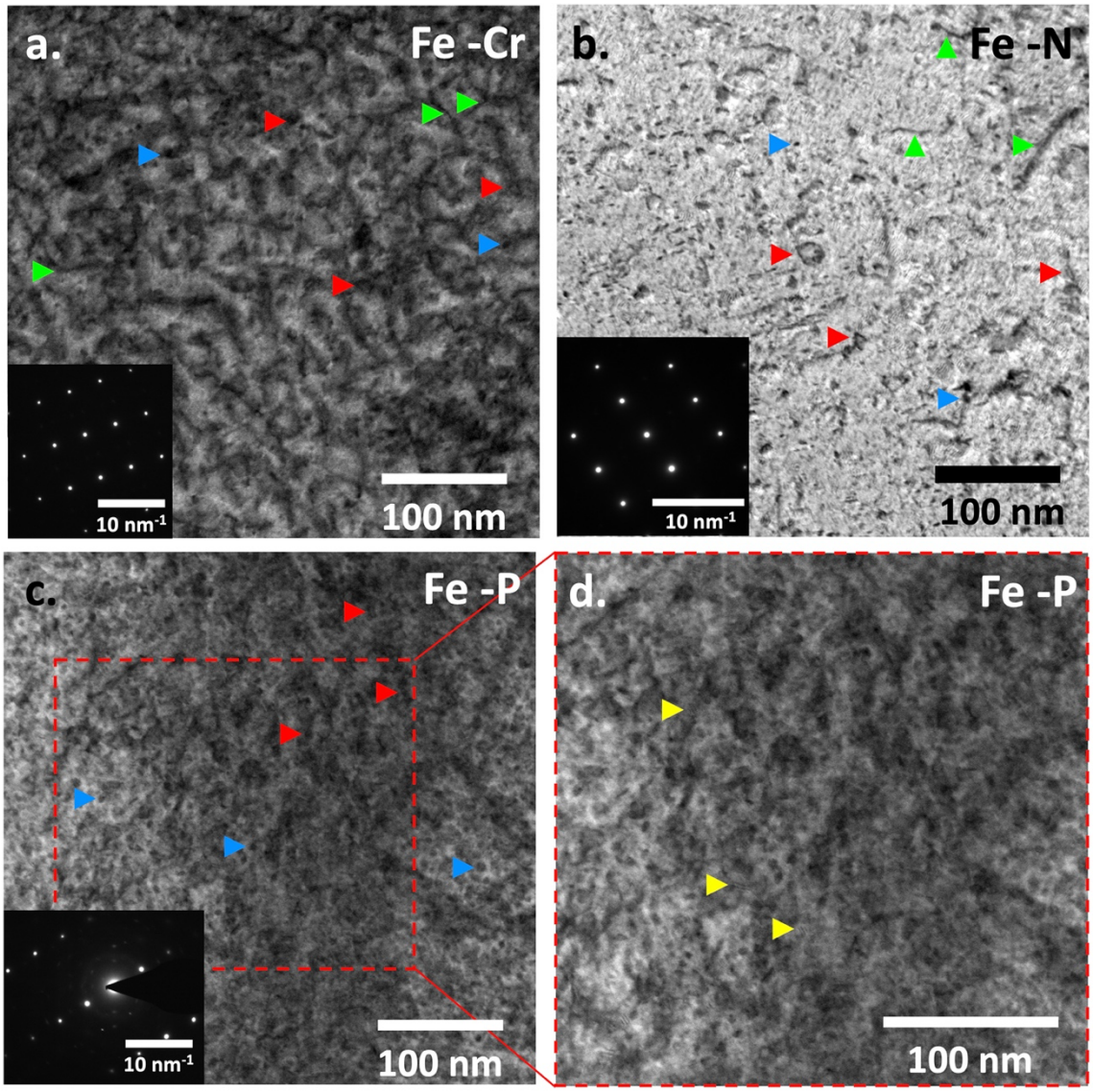

Figure 5.2: BFSTEM micrograpahs with inset SAED patterns of *ex situ* irradiated (a) Fe-Cr, (b) Fe-N, (c) Fe-P and (d) Fe-P in higher magnification. Dislocation loops, dislocation lines, clusters, and precipitates are indicated by red, green, blue, and yellow arrows respectively

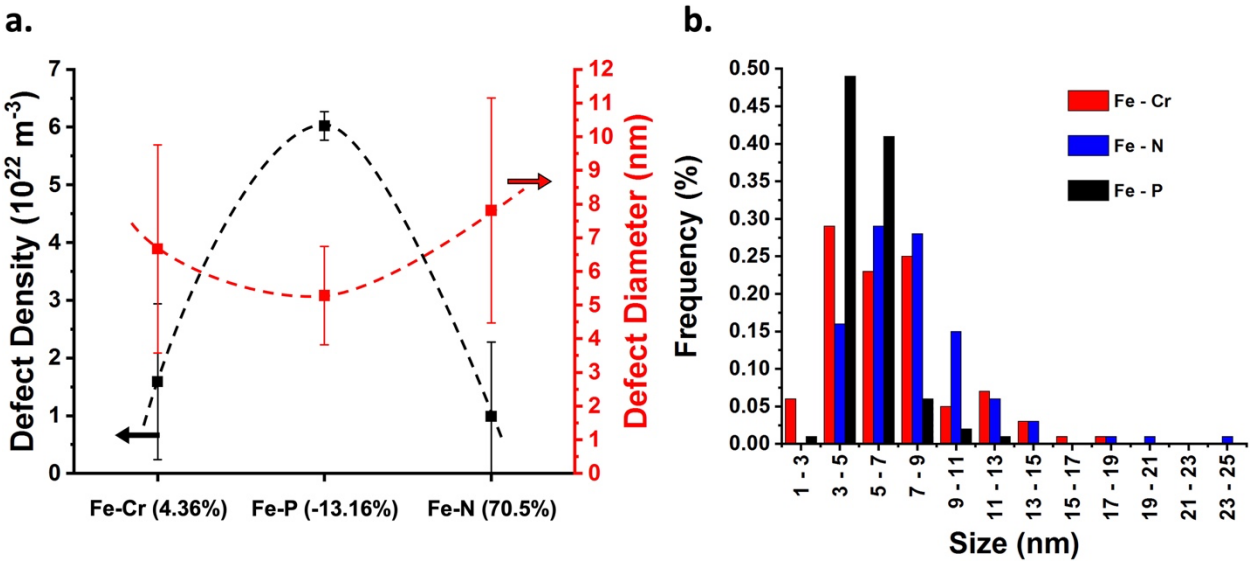

Figure 5.3: (a) Fe-Cr, Fe-P, and Fe-N Defect Density (left vertical axis) and Average Defect Diameter (right vertical axis) vs Alloy Type ordered by size factor and (b) Size distributions of Fe-Cr, Fe-P, and Fe-N

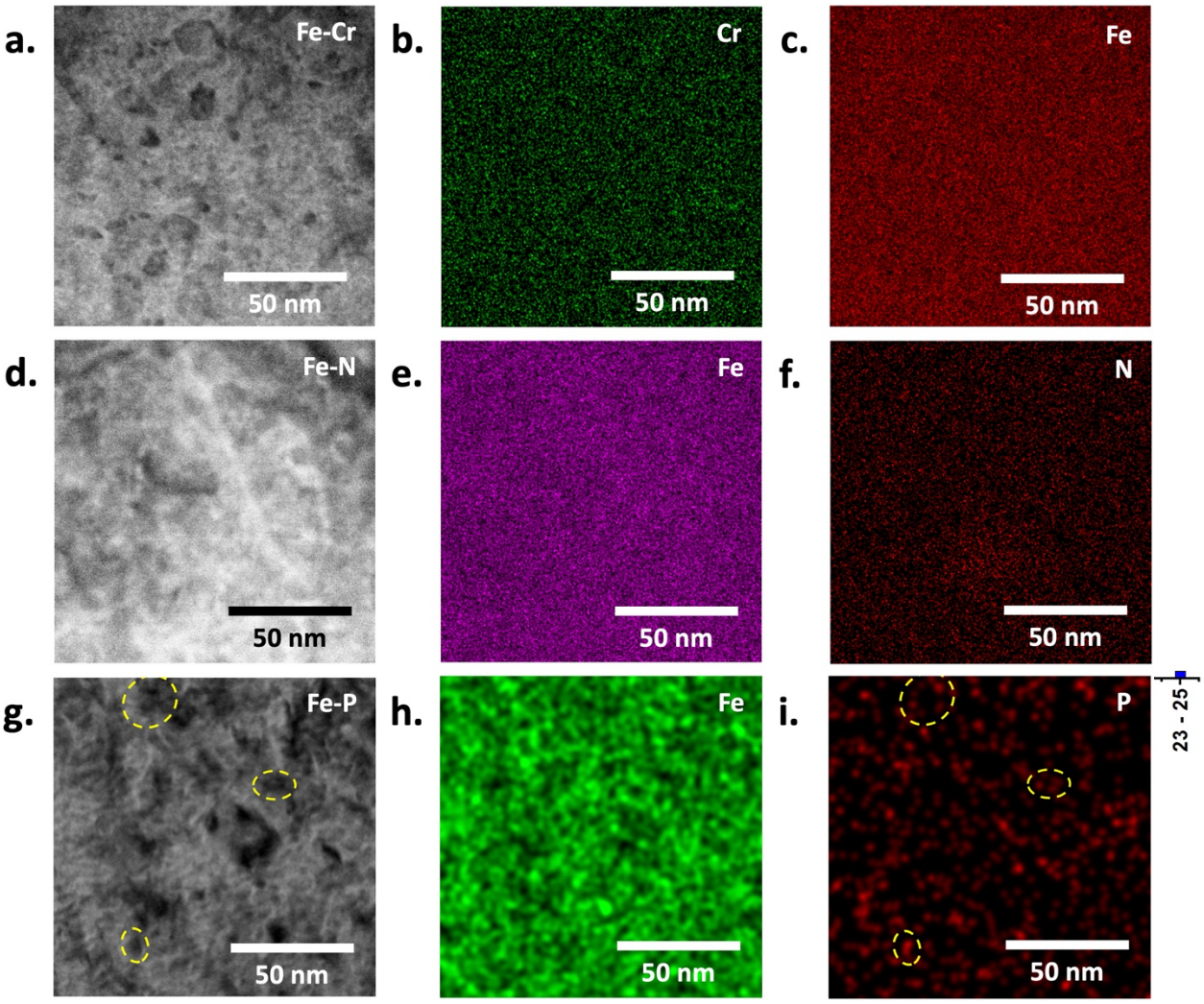

Figure 5.4: Reference images, Fe and solute EDS maps of (a – c) Fe - Cr, (d – f) Fe - N, and (g – i) Fe - P

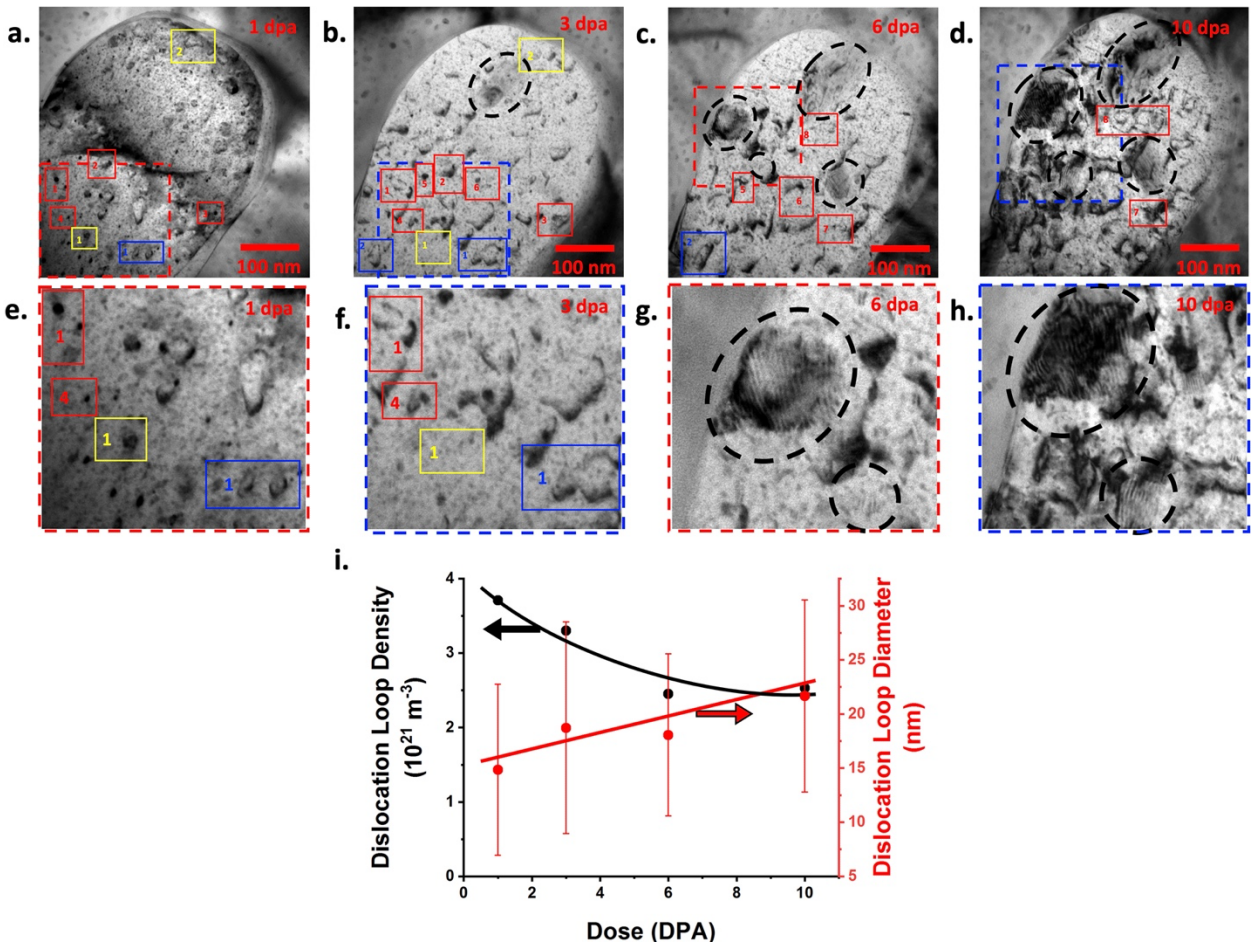

Figure 5.5: (a – d) BFTEM micrographs of α Fe region, (e – d) higher magnification images of the α Fe region from 1 dpa to 10 dpa, and (i) Dislocation Loop Density (left vertical axis) and Average Dislocation Loop Diameter (right vertical axis) vs Dose.

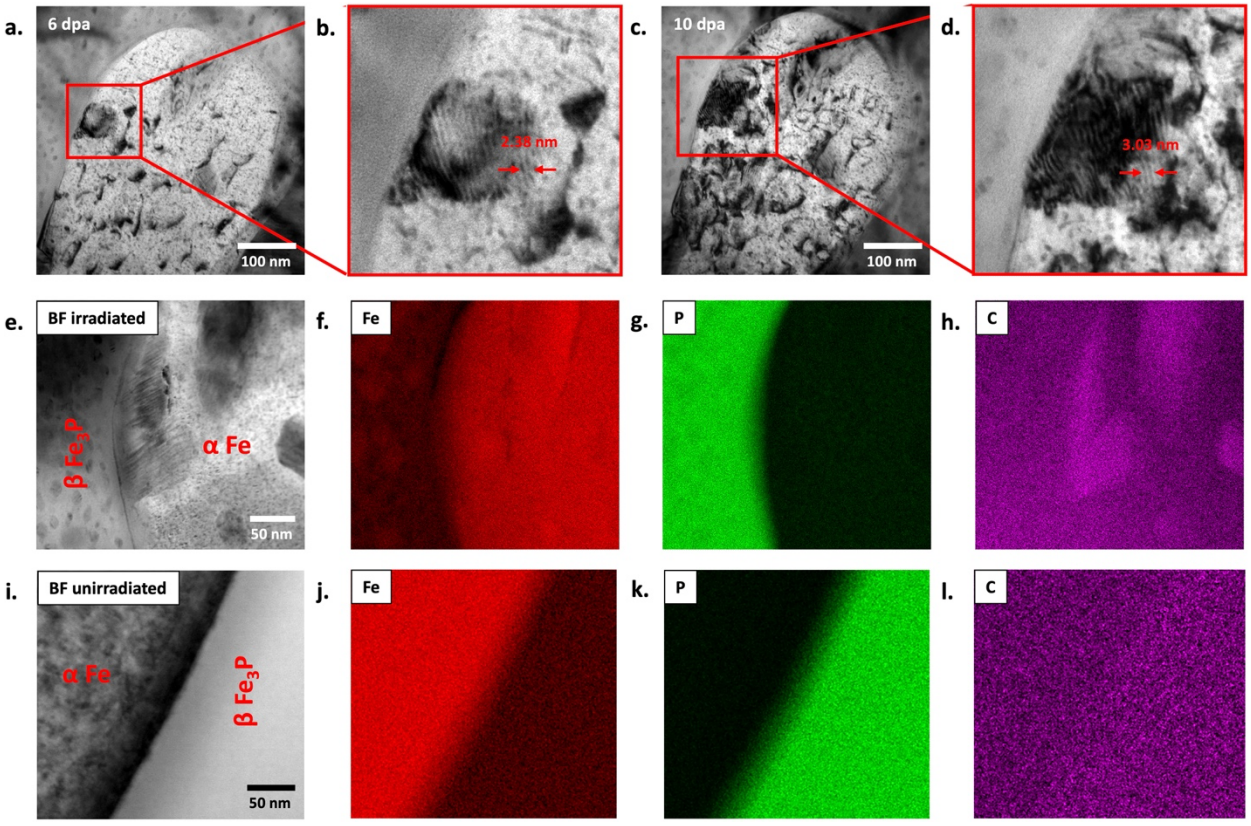

Figure 5.6: (a) BFTEM image of α Fe region at 6 dpa with (b) higher magnification image of precipitate showing fringe separation measurement, (c) BFTEM image of α Fe region at 10 dpa with (d) higher magnification image of precipitate showing fringe separation measurement, (e) STEM reference image of irradiated α Fe region and corresponding (f) Fe, (g) P, and (h) C EDS maps, and (i) STEM reference image of unirradiated α Fe region and corresponding (j) Fe, k. P, and (l) C EDS maps

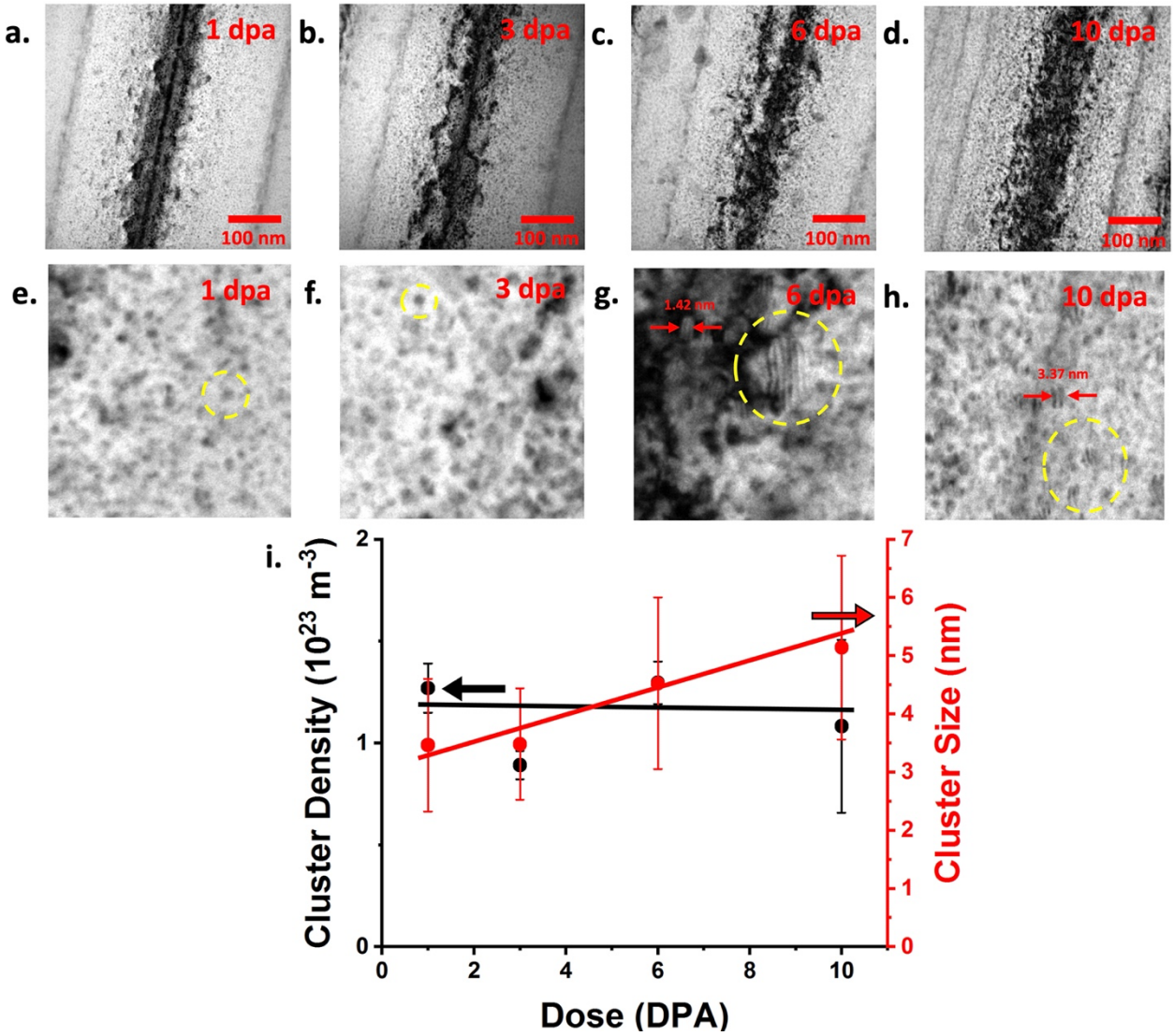

Figure 5.7: BFTEM images of Fe - P region at (a) 1 dpa, (b) 3 dpa, (c) 6 dpa, and (d) 10 dpa with high magnification images of the same region at (e) 1 dpa, (f) 3 dpa, (g) 6 dpa, (h) 10 dpa and (i) Cluster Density (left vertical axis) and Size (right vertical axis)

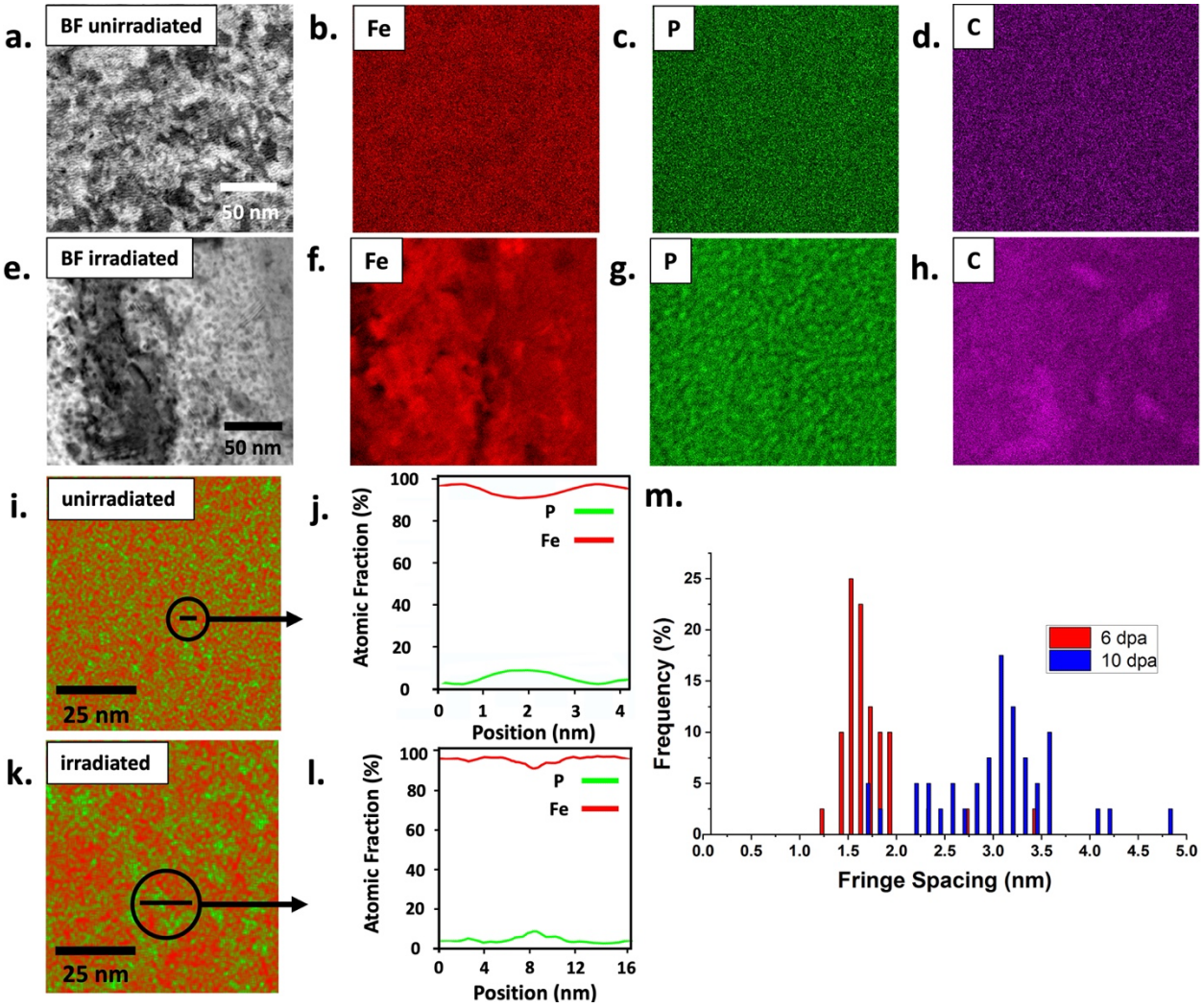

Figure 5.8: (a - d) Reference image and Fe, P, and C EDS maps of unirradiated Fe - P region, (e - h) reference image and Fe, P, and C EDS maps of irradiated Fe - P region, (i – l) EDS maps with black circled line indicating line scan and line scan composition profile, and (m) moiré fringe spacing distribution at 6 dpa (red) and 10 dpa (blue)

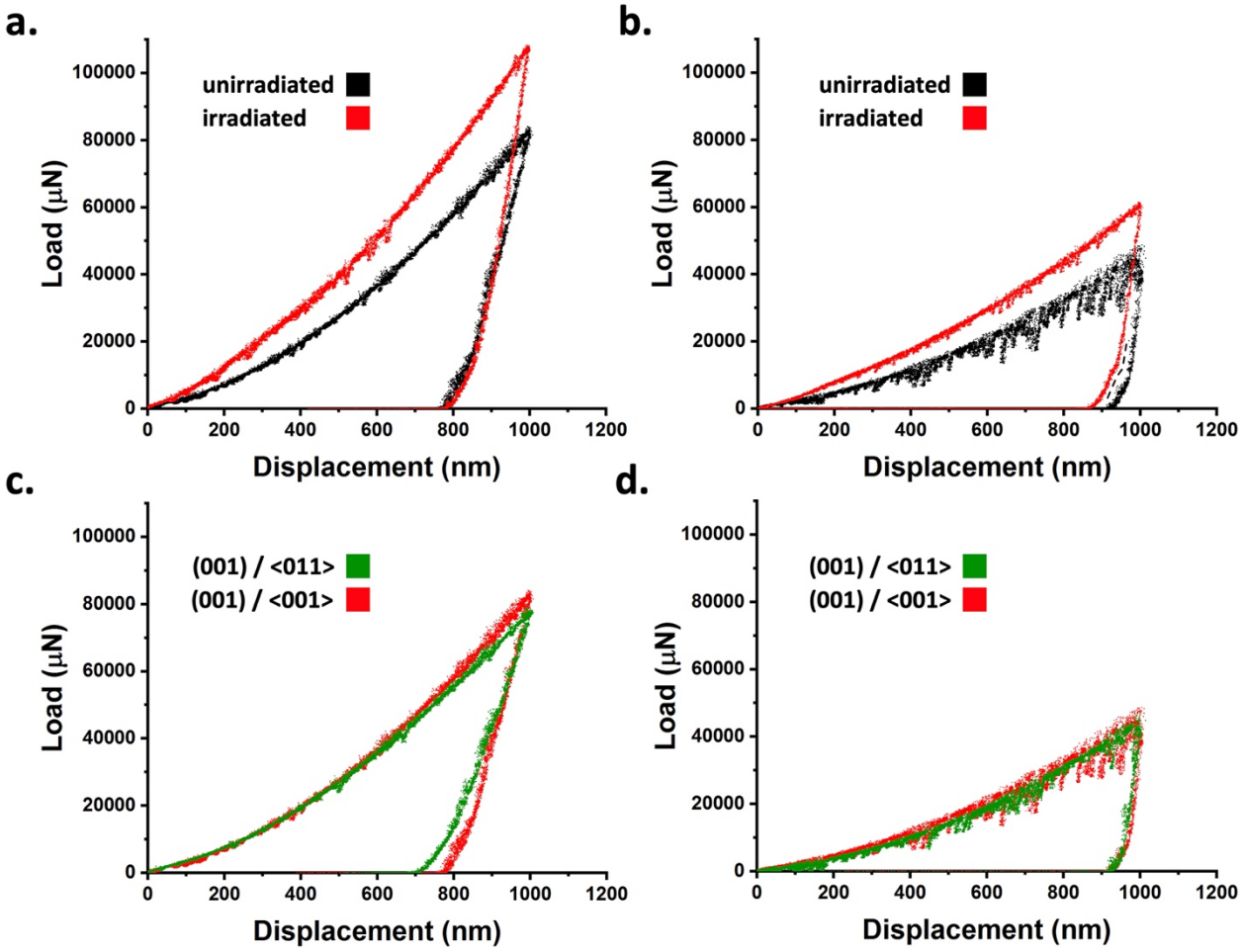

Figure 5.9: (a) Unirradiated and irradiated Fe - P Load vs Displacement (b) unirradiated and irradiated Fe - N Load vs Displacement with "pop out" indicated by black dotted line and black circle (c) (001) / <011> (green) and (001) / <001> (red) Fe – P Load vs Displacement and (d) (001) / <011> (green) and (001) / <001> (red) Fe – N Load vs Displacement

Table 5.1: Fe - P and Fe - N Hardness and Irradiation Hardening at depth of 500 nm

		Hardness (GPa)	**Irradiation hardening (MPa)**
Fe – P	Unirradiated	0.618	91.39
	Irradiated	0.934	
Fe - N	Unirradiated	0.356	45.97
	Irradiated	0.515	

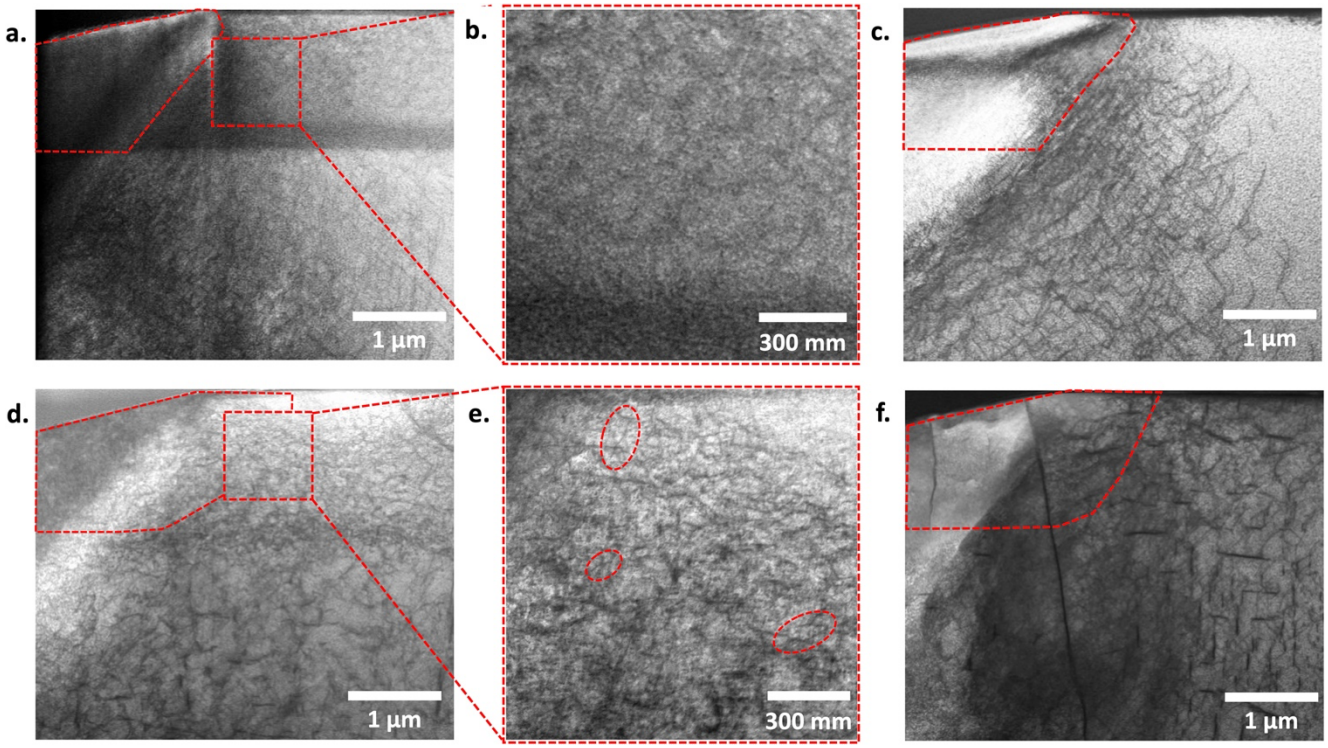

Figure 5.10: (a) heavily deformed region (indicated by red dotted border) of the irradiated Fe – P indentation (b) high magnification image of deformation microstructure in the irradiated zone of the irradiated Fe – P indentation cross section (c) heavily deformed region (indicated by red dotted border) of the unirradiated Fe – N indentation (d) heavily deformed region (indicated by red dotted border) of the irradiated Fe – N indentation (e) high magnification image of deformation microstructure in the irradiated zone of the irradiated Fe – N indentation cross section and (f) heavily deformed region (indicated by red dotted border) of the unirradiated Fe – N indentation

Table 5.2: Schmid Factors for <001> and <011> indentation directions

	Slip System	Facet 1	Facet 2	Facet 3	Edge 1	Edge 2	Edge 3	Tip
110 Indent Direction	(-1,0,-1)or (1,0,1)/[-1,-1,1]	0.328	0.2	0.375	0.304	0.478	0.351	0.408
	(-1,0,-1) or (1,0,1)/[-1,1,1]	0.212	0.464	0.227	0.451	0.295	0.387	0.408
	(-1,0,1) or (1,0,-1)/[-1,1,-1]	0.248	0.5	0.151	0.43	0.478	0.351	0.408
	(-1,0,1)or (1,0,-1)/[-1,-1,-1]	0.293	0.164	0.431	0.325	0.295	0.387	0.408
	(0,-1,-1) or (0,1,1)/[-1,-1,1]	0.128	0.128	0	0	0.127	0.127	0
	(0,-1,-1) or (0,1,1)/[-1,1,-1]	0.252	0.252	0	0	0.091	0.091	0
	(0,1,-1)or (0,-1,1)/[-1,-1,-1]	0.171	0.048	0.219	0.126	0.127	0.127	0
	(0,1,-1) or (0,-1,1)/[-1,1,1]	0.048	0.171	0.219	0.126	0.091	0.091	0
	(-1,1,0) or (1,-1,0)/[-1,-1,1]	0.2	0.328	0.375	0.195	0.351	0.478	0.408
	(-1,1,0) or (1,-1,0)/[-1,-1,-1]	0.464	0.213	0.227	0.317	0.387	0.295	0.408
	(-1,-1,0) or (1,1,0)/[-1,1,1]	0.165	0.293	0.466	0.325	0.351	0.478	0.408
	(-1,-1,0) or (1,1,0)/[-1,1,-1]	0.5	0.248	0.156	0.43	0.387	0.295	0.408
	AVERAGES	0.251	0.251	0.237	0.252	0.288	0.288	0.272
	OVERALL AVERAGES	**FACET Avg** = 0.246			**EDGE Avg** = 0.276			**TIP Avg.** = 0.272
100 Indent Direction	(-1,0,-1) or (1,0,1)/[-1,-1,1]	0.215	0.264	0.492	0.299	0.427	0.413	0.408
	(-1,0,-1) or (1,0,1)/[-1,1,1]	0.404	0.356	0.182	0.477	0.335	0.348	0.408
	(-1,0,1) or (1,0,-1)/[-1,1,-1]	0.356	0.196	0.182	0.477	0.427	0.413	0.408
	(-1,0,1) or (1,0,-1)/[-1,-1,-1]	0.264	0.104	0.492	0.299	0.335	0.348	0.408
	(0,-1,-1) or (0,1,1)/[-1,-1,1]	0.023	0.059	0.226	0.069	0.099	0.037	0
	(0,-1,-1) or (0,1,1)/[-1,1,-1]	0.08	0.044	0.084	0.11	0.115	0.021	0
	(0,1,-1)or (0,-1,1)/[-1,-1,-1]	0.221	0.023	0.226	0.069	0.099	0.037	0
	(0,1,-1) or (0,-1,1)/[-1,1,1]	0.164	0.08	0.084	0.11	0.115	0.021	0
	(-1,1,0) or (1,-1,0)/[-1,-1,1]	0.2	0.328	0.375	0.367	0.327	0.41	0.408
	(-1,1,0) or (1,-1,0)/[-1,-1,-1]	0.464	0.213	0.227	0.367	0.41	0.327	0.408
	(-1,-1,0) or (1,1,0)/[-1,1,1]	0.165	0.293	0.446	0.367	0.327	0.41	0.408
	(-1,-1,0) or (1,1,0)/[-1,1,-1]	0.5	0.248	0.156	0.367	0.41	0.327	0.408
	AVERAGES	0.255	0.184	0.264	0.282	0.286	0.259	0.272
	OVERALL AVERAGES	**FACET Avg** = 0.234			**EDGE Avg** = 0.275			**TIP Avg.** = 0.272

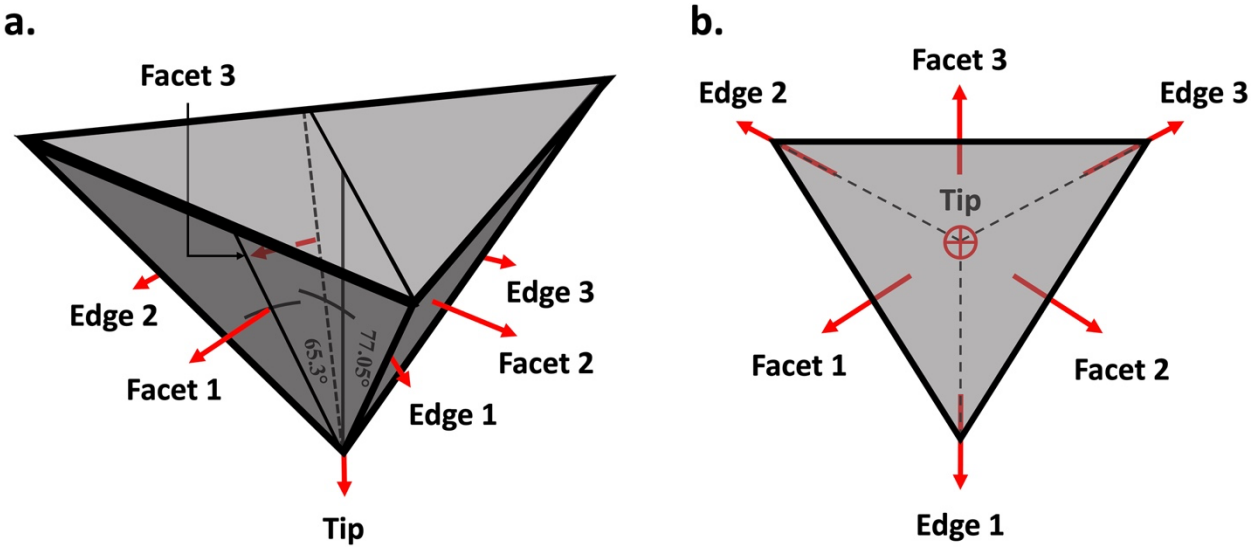

Figure 5.11: (a) 3D perspective of Berkovich nanoindenter tip with stress directions indicated by red arrows and (b) Top-down perspective of Berkovich nanoindenter tip with stress directions indicated by red arrows

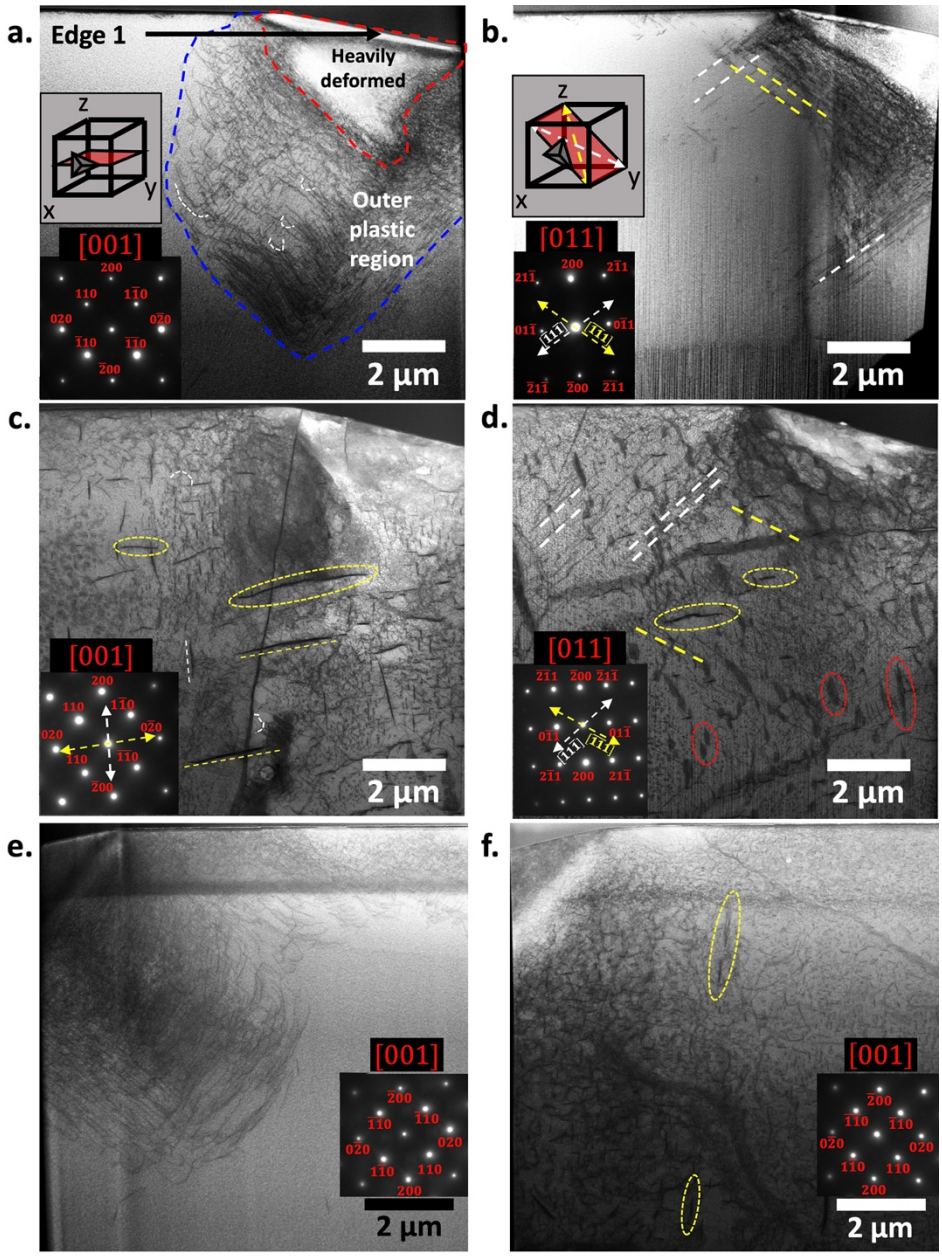

Figure 5.12: (a) Unirradiated (001) / <001> Fe - P indentation cross section (b) unirradiated (001) / <011> Fe - P (c) unirradiated (001) / <001> Fe - N (d) unirradiated (001) / <011> Fe – N (e) irradiated (001) / <001> Fe – P (f) irradiated (001) / <001> Fe - N

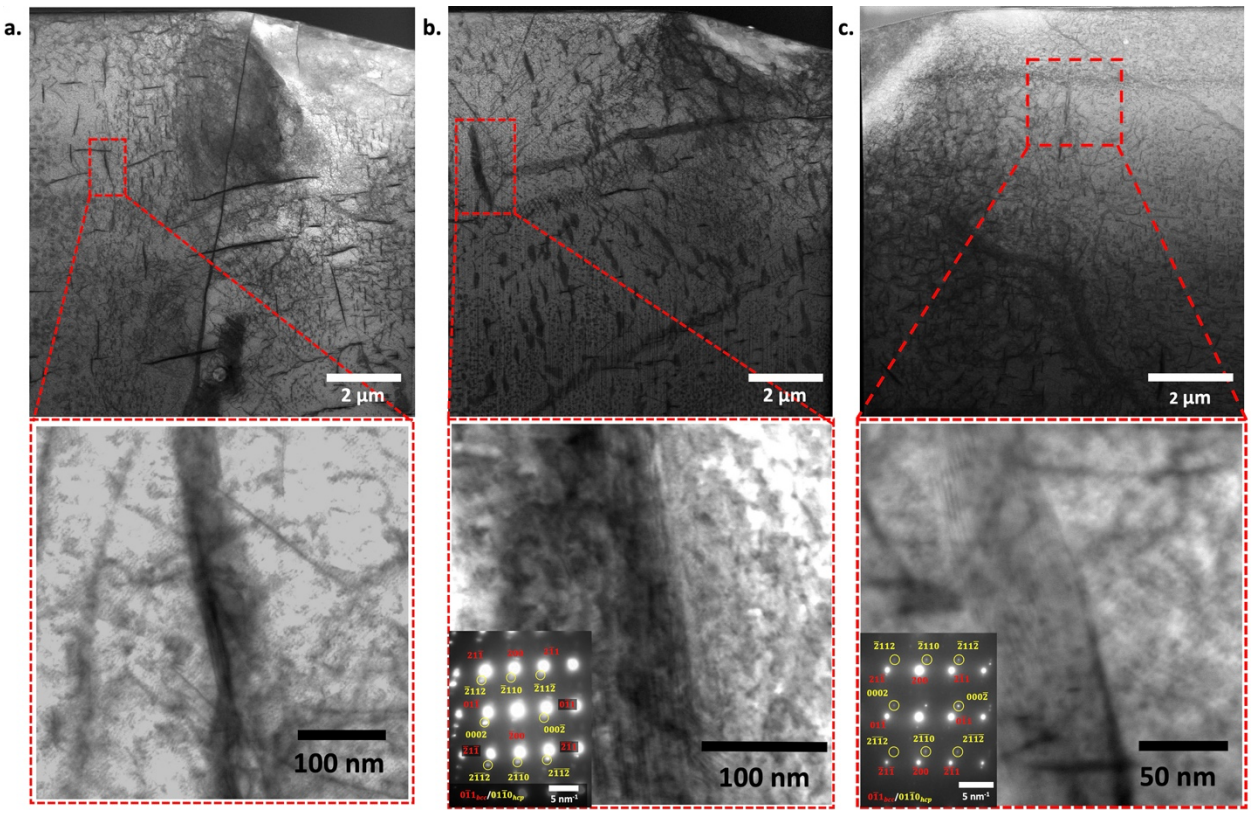

Figure 5.13: BFSTEM indentation cross section images of (a) unirradiated (001) / <001> Fe – N with enlarged martensitic lathe image (bottom left) (b) unirradiated (001) / <011> Fe – N with enlarged martensitic lathe image (bottom middle) and (c) irradiated (001) / <001> Fe – N with enlarged martensitic lathe image (bottom right)

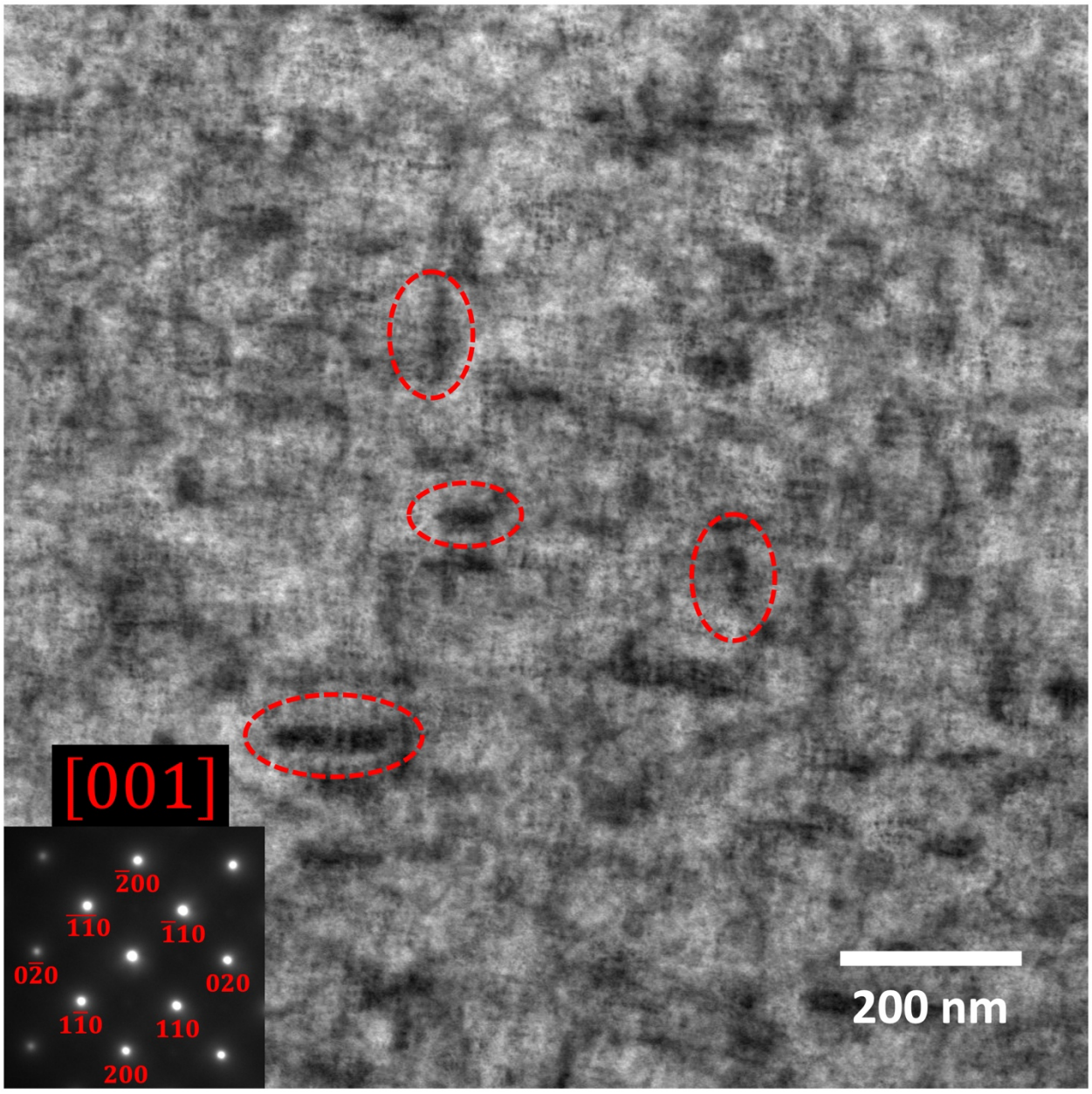

Figure 5.14: High magnification BFSTEM image of irradiation damaged zone in irradiated (001) / <001> Fe - N with vertically and horizontally aligned dislocations indicated by red dotted circles

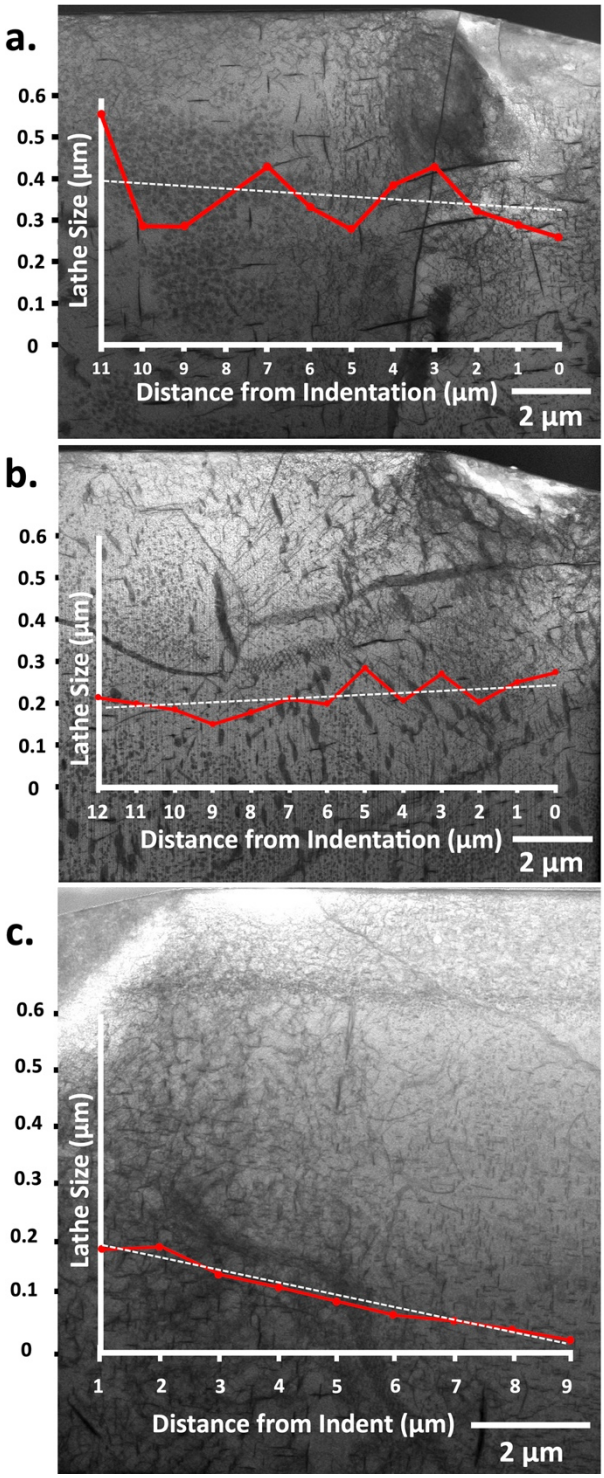

Figure 5.15: Lathe size vs Distance from indentation for (a) unirradiated (001) / <001> Fe - N (b) unirradiated (001) / <011> Fe - N and (c) irradiated (001) / <001> Fe - N

6. DISCUSSION

6.1 Self-interstitial Atom Trapping

The solute misfit in an alloy, which is quantified by size factor and discussed in section 3.2.2.2, has been demonstrated by a number of studies to influence the irradiation induced microstructural evolution, i.e. RIS behavior [7,13] and defect density in iron-based alloys. G Was explains that the strain fields produced by misfitting solute atoms interact with and trap migrating SIAs [7]. The degree of solute misfit can influence the trapping capability of the solute atom. Satoh et al. demonstrated this point in a study that showed an increase in defect density with an increase in the magnitude of the size factor, i.e. the degree of solute misfit, in model Cu binary alloys with undersized substitutional Co, Ni, and Be which had size factors of -3.78, -8.46, and -26.45 respectively [27]. Enhanced SIA trapping increases the SIA migration energy and slows SIA mobility as indicated by Eq 2.6 in section 3.2.2.2. Trapped SIAs then form defects such as di interstitial dumbbells and crowdions which act as nucleation sites for interstitial clusters and dislocation loops [57,123]. The strong trapping and reduced mobility of SIAs leads to an increase in defect density per Eq 2.5 in section 3.2.2.2. The degree to which these migrating SIAs become trapped and the configurations these di interstitial defects assume, i.e. dumbbell or crowdion configuration, dictate the stability of the nucleation sites. More stable nucleation sites will result in lower nucleation site dissociation and an increase in defect density.

The elevated defect density, 6 x 10^{22} m^{-3}, of the Fe-P alloy in the current study can be explained in part by the misfitting P in the α Fe lattice. P, with a size factor of -13.16, is an undersized substitutional atom with a relatively large size factor magnitude in α Fe [78]. The enhanced trapping capability of P in α Fe has been demonstrated by ab initio studies [55,123]. Furthermore, P has a strong binding energy, between 1.02 eV and 1.05 eV, with SIAs in the <110> dumbbell configuration [123]. The <110> dumbbell configuration is the most stable SIA configuration in α Fe [124], so P will form a highly stable solute – SIA complex in α Fe leading to more stable cluster and dislocation loop nucleation sites and increased defect densities as discussed in the previous paragraph. The increased defect density in Fe alloys as a result P concentration has been demonstrated in other studies [88,125] and a density functional theory (DFT) study by C Becquart et al. showed that the stability of the solute – SIA complexes was

highest for P. The stability of the P – SIA complex was attributed in part to the degree of misfit, i.e. the magnitude of the size factor. However, size factor was not the sole predictor of solute – SIA bonding in the study by C Becquart et al. [91], and cannot entirely explain the defect density disparities in the current study either.

Studies have reported mixed defect density results in ferritic Fe alloys with N [19,22,126]. The Fe – N alloy has the largest size factor and size factor magnitude, 70.5 [63], but this alloy has the lowest defect density, 9.85 x 10^{21} m^{-3}, of the three alloys in the current study so clearly, neither size factor nor size factor magnitude alone can predict the irradiation induced defect densities in irradiated materials. The strain of the lattice produced by interstitial N will result in interaction with migrating SIAs and may slow the mobility of those SIAs as well, but the stability of the resulting cluster or dislocation loop nucleation site also matters. An ab initio study by C Becquart et al. showed that interstitials, N and C, do not form stable solute – SIA complexes in shared sites such as <110> dumbbells of <111> crowdions in fact a negative binding energy has been shown for N and C solute – SIA complexes, and they may migrate back to interstitial sites after interaction. The lack of stability of these complexes is due to the space occupied by interstitial atoms in the α Fe lattice [127]. Excess space is required to form a stable <110> dumbbell or <111> crowdion defect since the formation of a <110> dumbbell involves forcing two atoms into one atomic position, the center position, while the formation of a <111> crowdion defect involves the sharing of 8 or 9 lattice sites by 9 or 10 atoms along a <111> direction. Larger solute atoms will have a more difficult time fitting into these configurations which results in instability. Although it was not demonstrated with interstitial solutes, C Becquart et al. demonstrated in a DFT study the instability or even repulsion of solute – SIA complexes resulting from largely oversized solute atoms similar to the instability present in interstitial C and N – SIA complexes, which implies interstitial behavior is similar to largely oversized substitutional atoms with respect to SIA binding. Furthermore, to highlight the importance of the magnitude of size factor for undersized solutes, the same DFT study demonstrated stronger stability of solute – SIA complexes for undersized substitutional atoms with a larger size factor magnitude in α Fe [91].

The Fe – Cr alloy had a defect density of 1.59 x 10^{22} m^{-3}, is approximately a quarter the defect density of the Fe – P alloy and almost double the defect density of the Fe – N alloy. The Cr size factor, 4.36, is larger than the size factor of P, -13.16, and smaller than size factor of N,

70.5 but the magnitude of the Cr size factor is the smallest of the three solutes so clearly, neither the size factor nor the size factor magnitude can be the sole predictors of increased defect density. Instead, as the DFT study by C Becquart et al. demonstrated, size factor matters but there are regimes to the influence of size factor on solute - SIA complex stability and thus defect density. A higher magnitude of size factor for undersized solutes will result in increased solute – SIA complex stability, while a higher magnitude of the size factor for oversized solutes will result in instability or repulsion of solutes with SIAs. Furthermore, no strong solute – SIA complex stability relationship was seen for solutes with atomic sizes similar to sizes of the solvent atoms [91]. The Defect Density vs Size Factor graph in Fig. 6.1, which pulls data from literature [27,86,128–133], solid data points, as well as the current study, open data points, demonstrates these points. The graph shows a strong positive relationship between size factor magnitude and defect density for undersized substitutional solutes. This is likely due to the strong interaction between the migrating SIA and the elastic strain field produced by the misfitting undersized atom as well the stable solute – SIA complex that is formed upon trapping. For oversized substitutional solutes however, the story is not as straight forward. The defect densities are suppressed for all oversized solutes with large size factor magnitude. This is because, even if migrating SIAs interact with and are trapped by the large elastic strain field produced by the oversized substitutional atoms, they cannot form stable solute – SIA complexes which serve as cluster and dislocation loop nucleation sites. There is a large spread of defect densities for slightly oversized substitutional solutes and there is seemingly no relationship. This may imply that, in addition to enhanced trapping of SIAs by strain fields produced by misfitting solute atoms and improved solute – SIA complex stability through the excess volume provided by undersized solutes, chemical bonding is also an important component of SIA trapping and solute – SIA complex stability, which is also demonstrated by the DFT study by C Becquart et al. [91]. Finally, all interstitial solutes, which behave similarly to highly oversized substitutional atoms, exhibit suppressed defect densities. This is likely due to the lack of stability of the solute – SIA complexes produced by interstitials such as C or N [127]. This lack of stability may stem from the lack of excess volume for the formation of di interstitials.

6.2 Radiation Induced Segregation and Radiation Induced Precipitates

In addition to defect densities, solute size factor also influences the radiation induced segregation behavior in irradiated ferritic alloys [7,13]. Undersized solutes typically enrich at defects while depletion is seen for oversized solutes. Furthermore, the size of the solute atom also plays a significant role in their migration mechanisms. As discussed in section 3.2.4, undersized substitutional atoms will preferentially switch sites with SIAs so they will tend to follow interstitial flux and migrate toward interstitial biased sinks which will result in the enrichment of interstitial sinks such as clusters, dislocation loops and grain boundaries. On the other hand, oversized atoms preferentially switch with vacancies, thus they tend to move in the opposite direction as vacancies resulting in oversized solute depletion at vacancy sinks [7,134]. This explains the irradiation induced P and C segregation, clustering, and irradiation induced precipitation seen from Fig. 5.4, 5.6, and 5.8. The competition of undersized substitutional atoms such as P for interstitial segregation also explains the delayed carbide formation in the Fe - P region as compared to the α Fe region described in section 5.1.3. Recall that the α Fe has a relatively low concentration of P while the Fe - P region had a relatively high concentration of P as demonstrated in the EDS maps in Fig. 5.6 and 5.8. The low P concentration in the α Fe region means C atoms will not compete with P to migrate by interstitial flux to sinks. Thus, more C will reach those sinks and the local composition at the sink will reach the solubility limit of C in Fe more quickly resulting in the earlier formation of radiation induced carbides. The competition between P and C in segregation and enrichment of defect sites has been provided as an explanation in other studies as well [135,136]. Additionally, other studies have demonstrated the inhibition of C rich phases in the presence of P in ferritic steels as well [137,138].

The clustering of Cr in irradiated ferritic alloys is a well-known occurrence which was not observed in the Fe – Cr alloy in the current study [75,77,139,140]. This was despite the clustering of P in the Fe – P under the same conditions. The lack of Cr can be explained by the dose rate associated with ion irradiation [57,77]. Ion irradiation produces a high dose rate and a super saturation of interstitials and vacancies. These point defects find each other and annihilate before they have the opportunity to segregate to sinks and higher temperatures are needed to produce segregation as depicted in Fig. 3.12 [7,57] Furthermore, Cr may move by vacancy diffusion in ferritic Fe under irradiation since it is oversized [78] and as discussed in section 3.2.4, oversized substitutional solutes preferentially switch with a move by vacancy flux [7].

Vacancy diffusion requires high temperatures to become a dominating diffusion mechanism and the 370 °C irradiation temperature of the current study may not be high enough to produce significant vacancy diffusion [69]. P is able to segregate and cluster under high dose rate conditions because P diffuses rapidly in α Fe [55], thus P atoms can reach sinks before they are annihilated by vacancies. Additionally, since P is undersized in α Fe [78], it will preferentially switch with interstitials and diffuse by interstitial diffusion, which does not require an elevated temperature.

6.3 Hardening in Fe – P and Fe - N

The as received Fe – P was harder than the as received Fe – N which is expected since solid solution strengthening is generally greater in interstitial solid solutions than in substitutional solid solutions [104,141–143]. A closer look at the unirradiated Fe – N Load vs Displacement profile in Figs. 5.9 (d) which shows several load drops, and the Fe – N indentation cross section images in 5.12 (c), (d), and (f), which indicate martensitic phase transformation, may provide the answer. Stress induced martensitic phase transformations can act as stress relievers in ferritic alloys under applied stress due to a volume change associated with the phase change as explained by W.J. Dan et al. [144]. The lathes defects seen in Fig. 5.12 (c), (d), and (f) and the stress drops in the Load vs displacement profile in Fig. 5.9 (d), which have been demonstrated during martensitic phase transformations [121], suggest that a martensitic transformation has occurred, and that the transformation acted as a stress relief to the Fe – N alloy. The stress relief produced by the martensitic phase transformation would result in lower indentation load at all indentation depths thus a softer response. The stress relief from the martensitic transformation would also affect the irradiation hardening results in the Fe – N as well, since martensitic phase transformation was not seen in the irradiated region of the irradiated Fe – N sample and may have been prevented the increased defect density in the irradiation damaged region of the irradiated Fe – N, which was another unexpected result that will be discussed in more depth below. If the martensitic phase transformation produces a softer response, and there was no martensitic phase transformation in the irradiation damaged region, this would produce an even harder response in the irradiated Fe – N sample and more irradiation hardening than if the martensitic phase transformation had been absent from both irradiated and unirradiated conditions. This may explain the mixed irradiation hardening results in ferritic

alloys containing N [19–21,126] since some ferritic alloys containing N may not exhibit the stress induced martensitic transformation.

The nanoindentation results of the unirradiated and irradiated Fe – P and Fe – N demonstrate the dispersed barrier model well which predicts that the yield strength will increase with an increase in defect density [7]. The irradiation hardening of both alloys match well with the hardening values expected by the dispersed barrier model in Eq. 2.17 from section 3.3.3, and the error is likely due to the substrate effects associated with indentation in ion irradiated alloys [145,146]. Furthermore, the results demonstrated how P and N influence the mechanical properties resulting from irradiation. P has been shown by the current study as well as others [88,125], to enhance defect formation in irradiated Fe alloy. This enhanced defect formation produces a high defect density which results in a harder material. The Fe – N alloy on the other hand, which had a significantly smaller irradiated induced defect density, also exhibits less irradiation hardening as expected. This hardening effect is further reinforced by the size differences of the plastic zones of the Fe – P and Fe – N alloys from Fig. 5.10 in section 5. The results also indicate that the indentation method, the method to calculate irradiation hardening put forward by Kasada et al. [116] and the inspection of indentation cross section are all valuable in evaluating the mechanical properties of unirradiated and irradiated alloys.

6.4 Deformation Mechanism and Hardness Dependence on Indentation Direction

Single crystal mechanical anisotropy is a phenomenon that has been demonstrated in BCC materials [117,147,148]. The different deformation mechanisms that are triggered along different crystallographic orientations is one explanation for mechanical anisotropy [148]. Cross slip which is demonstrated for the <001> indentation direction, Fig. 5.12 (a) and (e), may be the dominant deformation mechanism along the <001> indentation direction generally although the entire indentation was not imaged so it cannot be said definitively. It is feasible that the high number of similar Schmid factors associated with the <001> indentation direction facilitates the cross slip mechanism as implied by M.S. Duesbery et al. [117]. Cross slip as a dominant deformation mechanism in the <001> indentation direction may also be supported by the fact that the hardness of the <001> indentations were higher than the <011> indentation direction, as cross slip generally requires more stress than pure slip. Cross slip involves the slipping of a dislocation from a more favorable slip system to a less favorable slip system which requires

more stress to continue the slipping process. Furthermore, cross slip involves the activation of screw dislocations which are generally less mobile than pure edge dislocations [103], and finally, cross slip produces an increase in the number of obstacles to dislocation motion as it involves the activation of secondary slip systems. As such, cross slip has been identified as a strengthening mechanism in stages I and II of deformation. The activation of these secondary slip systems would certainly be facilitated by several slip systems with similar Schmid factors shown in the <001> indentation rows in Table 5.2. The dependence of indentation direction has been demonstrated in a previous study by Yin et al. which involved the Vicker's indentation of W along <001> and <011> indentation directions in a (001) oriented crystal [147]. Another study by C.A. Brookes et al. demonstrated the dependence of indentation direction on hardness through knoop indentation of MgO and LiF [148]. The study by Yin et al. demonstrated a harder indentation response when the vertices of the Vicker's indenter was aligned along the <011> direction. The study attributed the differences in hardness along the <001> and <011> directions to the differences in Schmid factors along those directions, and although the results of the current study show a harder response along the <001> indentation direction in the (001) single crystal Fe – P and Fe – N, the Schmid factor values from Table 5.2 support the results of higher hardness in the <001> indentation direction.

The anisotropy is also evident in the by the shapes of the heavily deformed regions of the <001> and <011> indentations, Fig. 5.12 (a – d). The heavily deformed regions of the <001> indentations expand out radially while the heavily deformed plastic zones of the <011> indentations are more confined beneath the indenter. These plastic zones are very similar to the Von Misses stress fields in a finite element model (FEM), in Fig. 6.2 (a) and (b) for <001> and <011> indentation directions respectively, by T. Khvan et al. [149]. The study by T. Khvan et al. also highlighted the point that the highest stress does not occur directly under the indenter for <001> indentation. This is demonstrated in the current study in the <001> indentation cross section, Fig. 5.12 (a). The brightest region of the plastic zone, which is the most deformed region and the region of highest stress, is to the side of the tip of the indentation. On the other hand, the FEM from [149] predicts the highest stress in the <011> indentation to occur directly under the indenter which is also demonstrated in the <011> indentation cross section, Fig. 5.12 (b) in the current study. An FEM study by W.Z. Yao et al. demonstrated similar results. The study involved FEM simulation of Berkovich indentation in (001) and (011) single crystal BCC W

with indenter rotation of -20°, 38°, and 45° inside a (001) grain and indenter rotation of -90°, -45°, and 60° inside a (011) grain. The study demonstrated more surface pile up in the (001) indention than in the (011) indentation, Fig. 6.3 (a) and (c) respectively, and more surface strain in the (001) indentation than in the (011) indentation, Fig 6.3 (b) and (d) respectively [150]. The plastic strain dependence on Berkovich indenter rotation was also investigated in a study by S. Jacob et al. which used surface strain mapping for indentations in (001) single crystal BCC Mo. The researchers found that more plastic strain occurred when facets were more normal to <111> directions [151].

6.5 Stress Induced Martensitic Phase Transformation in Fe - N

Stress induced martensitic phase transformation are not typically seen in ferritic alloys because a low SFE is generally required to produce this deformation mechanism. BCC materials generally have high SFE and high stresses between 13 GPa and 25 GPa are required to trigger a stress induced martensitic phase transformation [97,99,152]. N has been shown to lower the SFE in austenitic Fe alloys [153–157]. Stress induced martensitic phase transformations have also been demonstrated in high N austenitic steels as well [62,158,159]. It has been predicted that N will stabilize stacking faults in α Fe [95] which may also facilitate the stress induced martensitic phase transformation to occur. Furthermore, the stabilizing effect of N on the stacking faults may cause much of the martensitic phase to remain after unloading which has made it easier to detect in the current study than in others where the martensitic transformation in ferritic alloys has been reversed [97].

The stress induced HCP martensitic phase transformation in the current study is demonstrated by the Load vs Displacement behavior of the Fe – N alloy from Fig. 5.9 (b) and (d), and the SAED patterns and high magnification martensite lath images showing moiré fringes in Fig. 5.13 (a – c). A study by Matsukawa et al. that shows the parallelism between BCC and HCP planes demonstrates that $(110)_{bcc}$ planes will be parallel with $(1\bar{1}00)_{hcp}$ in a Zr-Nb HCP matrix with BCC precipitates. This suggests that the $(1\bar{1}00)_{hcp}$ satellite spots will be visible from a [011] ZA as seen in the unirradiated <011> Fe – N and the irradiated Fe – N samples. The moiré fringes further establish this point because moiré fringes imply there are two closely matched crystals where the moiré fringes appear [114,115]. The stress drops seen in all Fe – N

load vs displacement profiles as well as the "pop out" event seen in the irradiated Fe – N Load vs Displacement profile are demonstrated in a number of experimental and computational studies for martensitic phase transformations [62,121,160,161]. The stress drops associated with stress induced martensitic phase transformations are the result of the volume change that occurs during the phase transformation [144], while the "pop out" event is thought to be caused by a transformation back to the original phase [122].

The stress induced martensitic phase transformation may also explain why the cross slip deformation mechanism is not seen to such a degree in the <001> Fe – N samples as it is in both <001> Fe – P samples. Cross slip is favored in materials with high SFE while localized deformation mechanisms such as stress induced martensitic transformation is favored in materials with low SFE [7]. The stress induced martensitic phase transformation in the Fe – N alloy suggests a low SFE which would inhibit the cross slip deformation mechanism. This may suggest that the Fe – P alloy has a higher stacking fault energy that the Fe – N alloy.

The irradiation of Fe – N on the other hand seems to prevent the stress induced martensitic phase transformation in the Fe – N alloy as shown in Fig. 5.14 (c). The defects, which appear to be dislocations aligned along the same directions as the martensitic laths in the substrate, are smaller, with an average size of 82 nm, than the laths which had an average size of ~200 nm nearest the indentation site. Furthermore, the largest of the small vertically and horizontally aligned dislocations in the irradiated region of the irradiated Fe – N sample were 130 nm – 140 nm while the largest laths in the substrate of the irradiated Fe – N sample were between 400 nm and 1.25 μm. This may be due to the destabilization of stacking faults by self-interstitial Fe in the irradiated region of the Fe – N alloy. In the irradiated region there will be Fe^{2+} ion implantation as well as displaced Fe atoms that will occupy interstitial and di interstitial sites. This will result in an increase in the lattice parameter in the Fe – N irradiated region which has been shown to result in increased SFE. It is true that interstitial N will also produce lattice expansion as well, but interstitial N is small enough to fit into the larger interstices created during the formation of a stacking fault and stabilize those stacking faults. On the other hand, Self-interstitial atoms will be too large to fit into these stacking fault interstices and may end up destabilizing the stacking faults. A study by J. Yong et al. and S Lu et al. have shown increased SFE through with increasing lattice parameter [162]. These studies suggest that increasing the size of the interstitial atoms, i.e. Fe self-interstitial atoms resulting from Fe^{2+} irradiation and ion

implantation, will result in a decrease of the stacking fault energy and stress induced martensitic phase transformation will be inhibited as seen in the irradiated region of the Fe – N alloy in the current study.

The inhibition of the stress induced martensitic phase transformation in the irradiated Fe – N alloy may also be due to the BCC crystal structure. The inhibition of this stress induced martensitic phase transformation by the irradiation damage is different than the behavior in FCC alloys which exhibit decreased SFE from increased defect densities as demonstrated by several studies [163–165]. As such, the elevated defect densities produced by irradiation damage will decrease the SFE in irradiated FCC alloys. On the other hand, studies by Yang et al. and Y. Matsukawa et al. demonstrate the suppression of martensitic phase transformation in NiTi with B2 crystal structure, which is a BCC crystal structure with chemical ordering [166], by irradiation damage. Matsukawa attributed the suppression of the martensitic phase transformation to amorphization resulting from irradiation damage. Yang et al. attributed the suppression of the transformation to pinning by defects with the strongest influence coming from interstitial point defects and disordering [167,168]. The suppression of martensitic phase transformation by defect pinning is feasible since the defect structure of the small vertically and horizontally aligned dislocations suggests that martensitic needles start to form but are pinned by defects in the irradiated region of the irradiated Fe – N alloy. Alternatively, the suggestion by Yang et al. that the interstitial point defects produced strongest suppression of martensitic transformation supports the explanation from the previous paragraph that stacking faults are destabilized by large SIAs such as implanted Fe^{2+} and displaced Fe atoms in irradiated Fe – N.

6.6 Role of Irradiated Microstructure of Fe – P and Fe – N on Mechanical Properties

Ion irradiation, which is an attractive alternative neutron irradiation experiments because of the high dose rates, displaces atoms in ferritic alloys which agglomerate and cluster forming larger irradiation induced defects. The rate at which these defects nucleate and grow is dependent on how easily the point defects generated during irradiation can move throughout the system. If point defects are allowed to move easily, growth will be favored over nucleation and the microstructure will be comprised of a lower density of large defects. If the migration of these defects is slowed by the trapping of these point defects by sinks, nucleation will be favored over growth and the microstructure will be comprised of a high density of smaller defects [7].

Alloying elements and impurities will influence the development of the irradiated microstructure because they can act as traps to point defects and effect the resulting defect size and density [7]. P is an undersized substitutional solute in ferritic alloys with a large size factor magnitude so there is a large degree of misfit of P in these alloys [78]. The misfitting P produces a strain on the lattice which interacts with and traps migrating point defects forming solute – SIA complexes with highly stable di interstitial dumbbell configurations. The stability of which is due to the excess volume created in the unit cell by undersized substitutional P and the ease with which these SIAs can fit into these dumbbell arrangements [91]. These solute – SIA complexes act as nucleation sites for larger defects such as clusters and dislocation loops [57,123]. The stability of those nucleation sites results in a ubiquity of cluster and dislocation loop nucleation sites. Cr which is a slightly oversized substitutional atom in ferritic alloys [78] can also trap migrating point defects and form these nucleation sites, but since Cr is oversized the formation of the highly stable di interstitial dumbbell is not easily achieved [89,91]. Instead, Cr in ferritic alloys tends to form crowdion configurations which can also act as cluster and dislocation loop nucleation sites, but they are less stable so cluster and dislocation loop nucleation sites will be in lower density than that of the Fe – P case. N is an interstitial atom in ferritic Fe with a large size factor magnitude, thus it produces a large strain on the surrounding lattice. The strain field does interact with the migrating point defects and slows them down, but the excess space occupied by interstitial N makes the formation of solute – SIA complexes difficult so density of these cluster and dislocation loop nucleation sites will be much less [127]. These resulting microstructures play an important role in the mechanical properties in these ferritic alloys.

The primary deformation mechanisms of Fe – P, cross slip and pure slip along primary BCC slip systems, are prevented by the elevated density of defects in the irradiated case which makes plastic deformation more difficult. This is demonstrated in heavily deformation region of the irradiated Fe – P alloy and the outer deformed region of the irradiated Fe – P, Fig. 5.10 (a) and (b). The increased number of defects act as obstacles to dislocation motion and when a dislocation moves in this microstructure it quickly gets blocked by an obstacle. As more dislocations are generated and become blocked, they begin to tangle with and block each other resulting in forest hardening which makes it difficult to resolve discrete dislocations in TEM as seen in Fig. 5.10 (b). This resistance to dislocation motion by obstacles is defined by the dispersed barrier model [7] and illustrated by Fig. 6.4 (a), unirradiated Fe – P, and (b), irradiated

Fe - P. When the dislocations encounter these obstacles, more stress is required to push them through those obstacles which produces hardening. This is demonstrated by the correlation between defect or obstacle density and irradiation hardening, Fig. 6.5.

Stress induced martensitic lath formation in Fe – N may be inhibited in a similar way to the blockage of dislocation motion in Fe – P. It is true that defect density in irradiated Fe – N is less than in Fe – P but the irradiated Fe – N defect density is still much higher than the unirradiated condition. As such, the higher defect density of the irradiated Fe – N alloy will present many obstacles to deformation in the irradiated Fe – N alloy as well. These obstacles will prevent the formation or growth of the stress induced martensitic laths and irradiation hardening will occur which is shown in Fig. 5.14. The blockage of these martensitic laths is illustrated in Fig. 6.4 (c), unirradiated Fe – N, and (d), irradiated Fe – N while the correlation between hardening and defect density is shown graphically in Fig. 6.5.

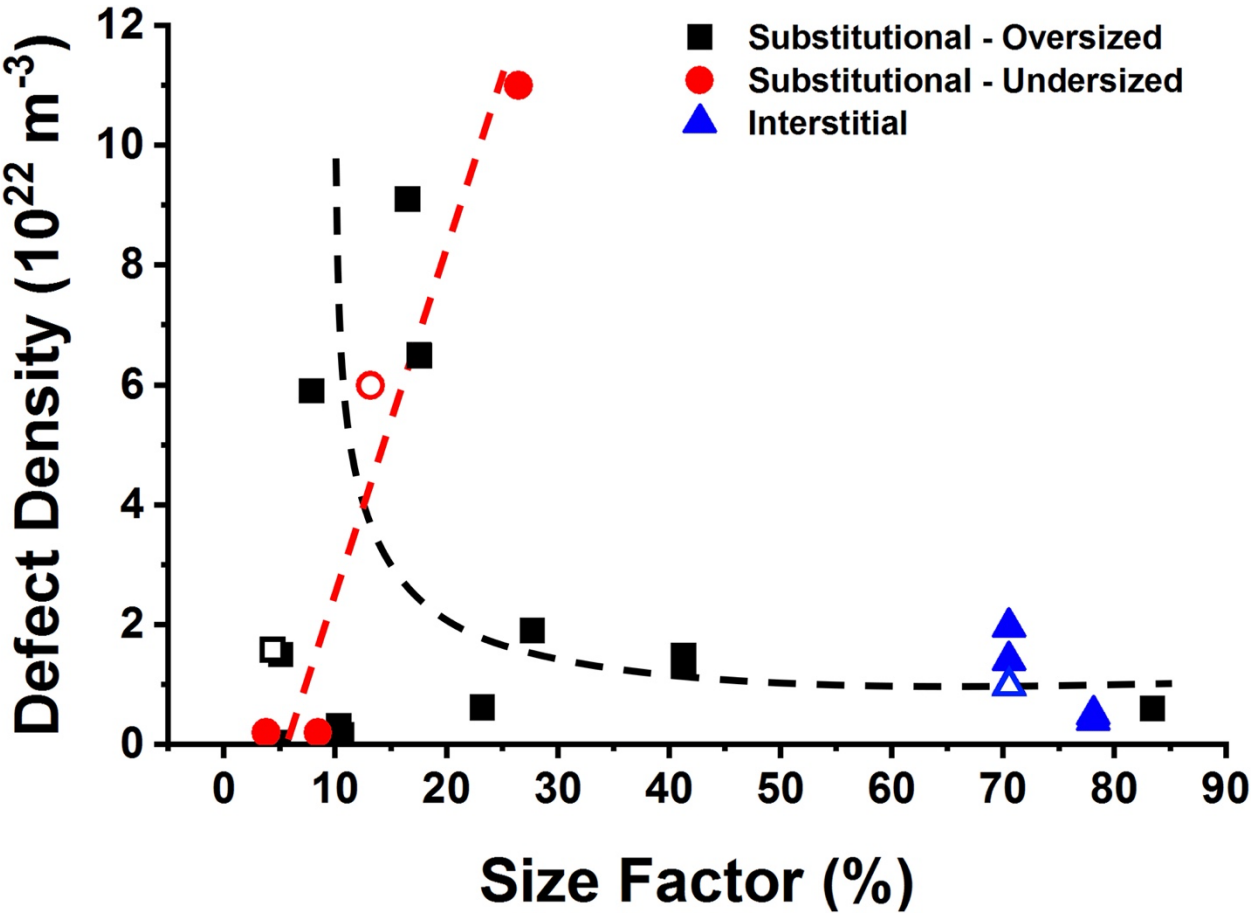

Figure 6.1: Defect Density vs Size Factor for Oversized Substitutional (black) undersized substitutional (red) and interstitial (blue) solutes

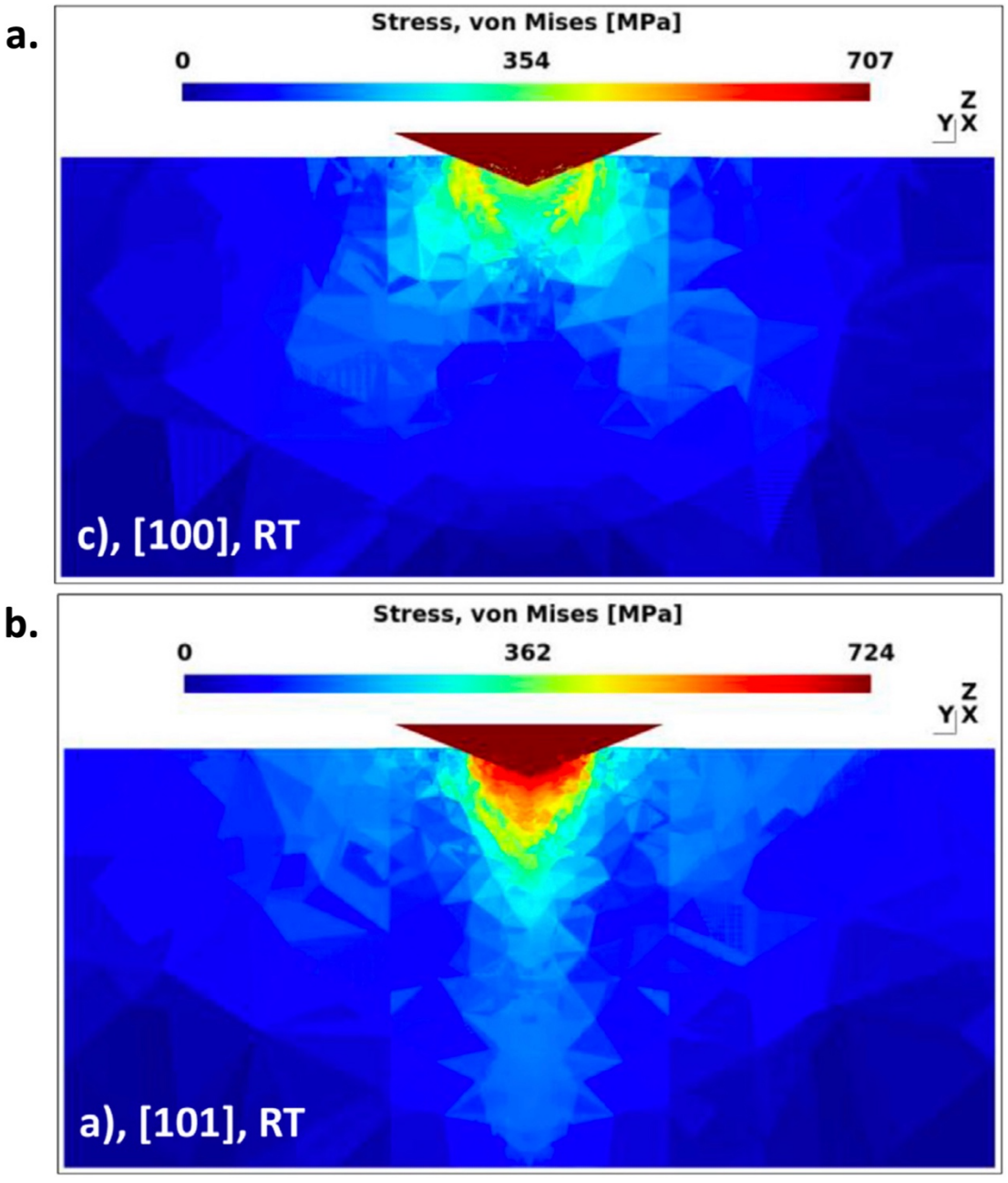

Figure 6.2: FEM Berkovich nanoindentation Von Misses stress field for (a) [100] surface orientation and (b) [101] surface orientation Adopted from [149]

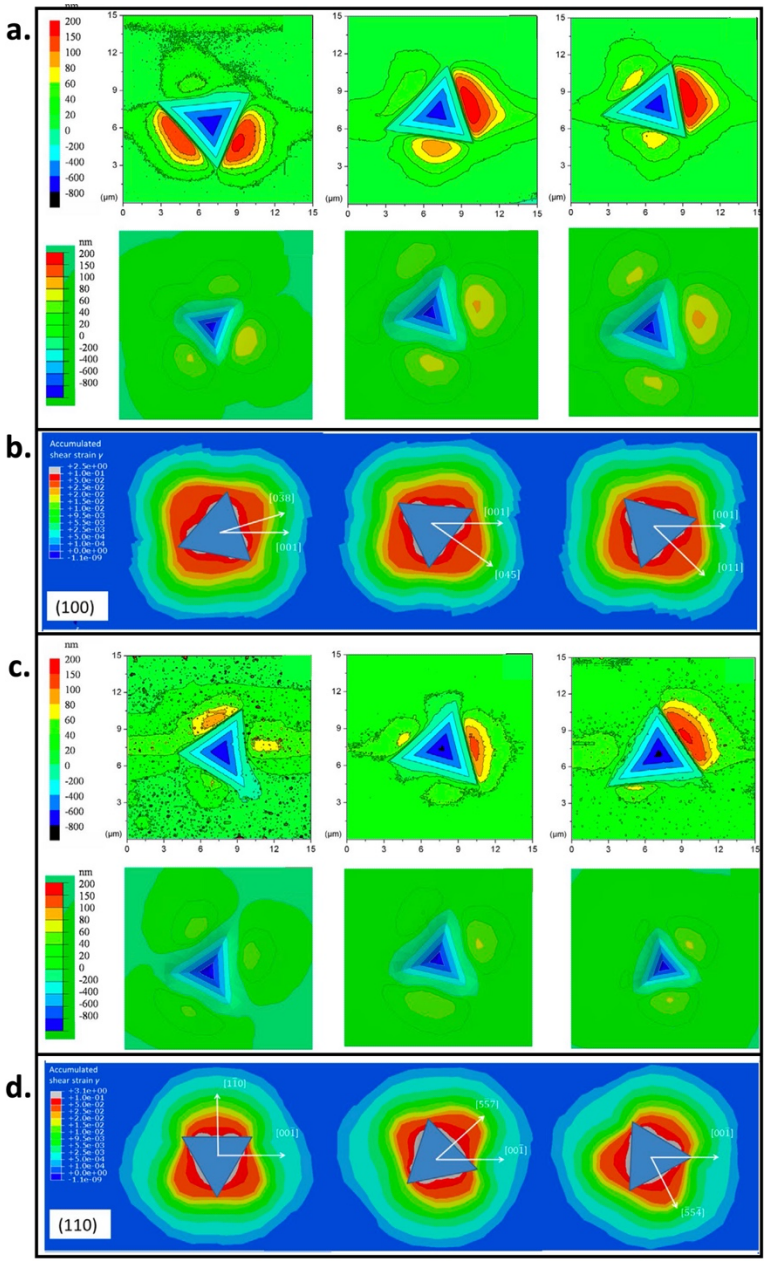

Figure 6.3: (a) FEM of surface pile up in (100) crystal orientation with indenter rotated off [001] direction by -20° (left), 38° (middle), and 45° (right) (b) FEM surface strain fields in (100) crystal orientation with indenter rotated off [001] direction by -20° (left), 38° (middle), and 45° (right) (c) FEM of surface pile up in (110) crystal orientation with indenter rotated off [001] direction by -90° (left), -45° (middle), and 60° (right) (d) FEM surface strain fields in (110) crystal orientation with indenter rotated off [001] direction by -90° (left), -45° (middle), and 60° (right)

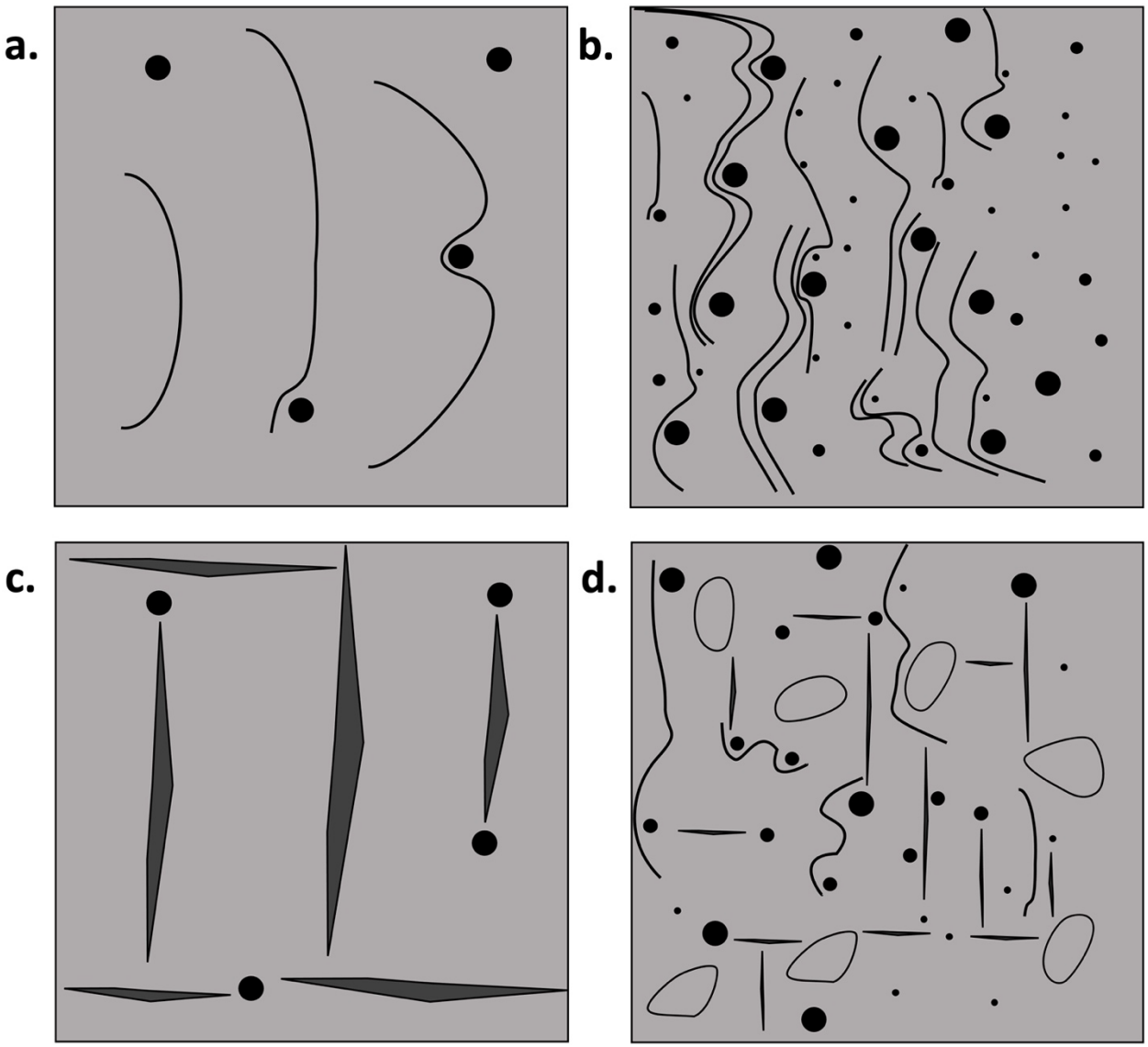

Figure 6.4: (a) Cross slip in unirradiated Fe - P (b) Dislocation pile up and tangling in irradiated Fe - P (c) Large stress induced martensitic lath formation in unirradiated Fe – N (d) Blockage of stress induced martensitic lath formation in irradiated Fe - N

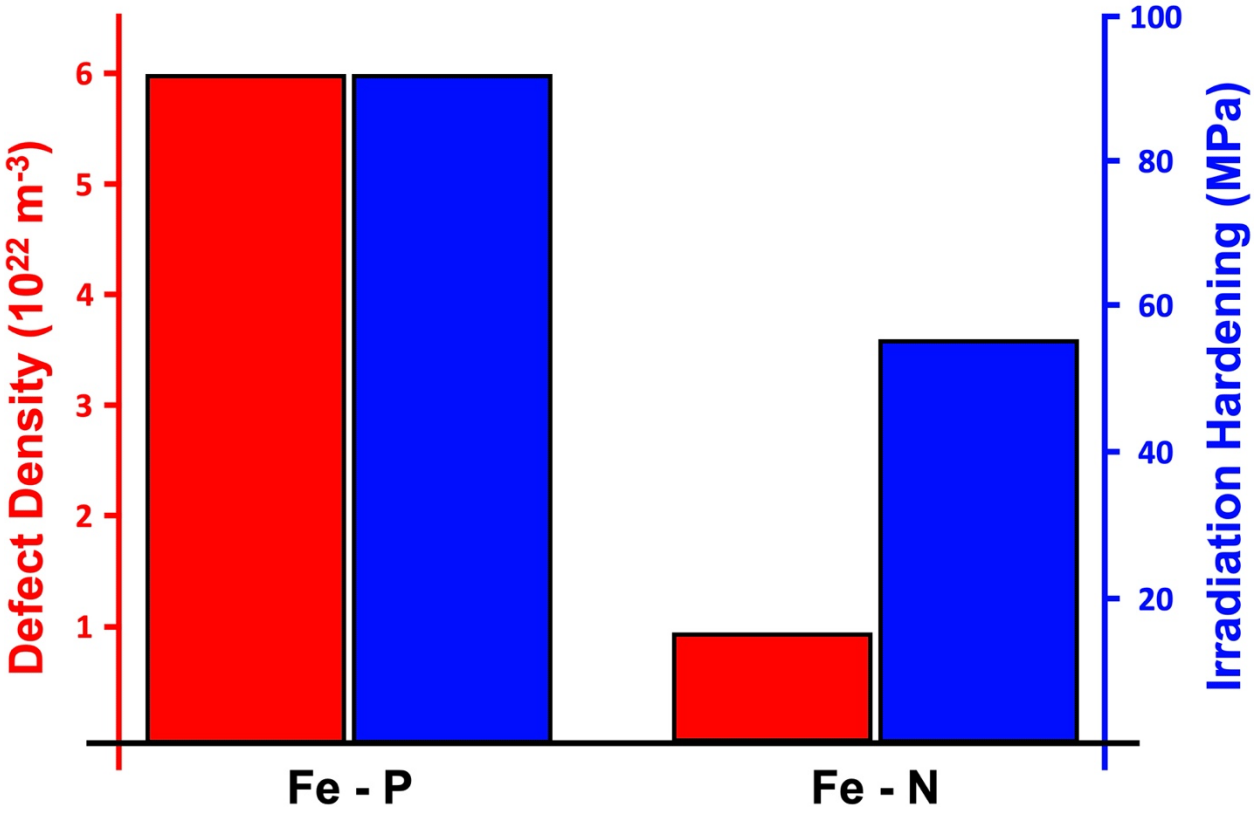

Figure 6.5: Fe - P and Fe - N Defect Density (red) and Irradiation Hardening (blue) Bar Chart

7. Summary and Conclusions

7.1 Irradiated Microstructures of Fe-Cr, Fe-N, and Fe-P

Three ferritic Fe binary alloys, Fe-9.5at%Cr, Fe-4.5 at%P, and Fe-2.3at%N, have been irradiated *ex situ* with 4.4 MeV Fe^{2+} ions to 8.5 dpa. The resulting irradiated microstructures were investigated to determine the influence of solute size, i.e. oversized or undersized, and solute type, i.e. interstitial or substitutional, on the irradiation induced defect formation in irradiated ferritic Fe alloys. The Fe-4.5at%P alloy was also irradiated *in situ* with 1 MeV Kr^{2+} ions to 10 dpa while the defect evolution of two regions, an Fe-P region and a α Fe region were observed. The following conclusions have been made:

- The Fe-P irradiated microstructure has a significantly higher defect density and finer defect structure than the irradiated microstructures of the Fe-Cr and the Fe-N.
- Point defects are trapped by P in the P rich Fe-P region resulting in a high density of P rich clusters and the limited formation and growth of dislocation loops.
- Point defects are allowed to migrate more easily in the P depleted α Fe region allowing dislocation loops to form and grow.
- P slows the formation of radiated-assisted carbides in the P rich Fe-P region
- Undersized substitutional solutes may have enhanced SIA trapping and may form highly stable defect nucleation sites thus promoting high irradiation induced defect density.
- The excess space occupied by oversized substitutional and interstitial solutes may prevent the formation of stable solute-SIA sites thus resulting in unstable cluster and dislocation loop nucleation sites and lower defect densities.

7.2 Fe-P and Fe-N Nanoindentation

Berkovich nanoindentation was done in (001) single crystal unirradiated and irradiated Fe-P and Fe-N alloys along <001> and <011> crystallographic directions. Cross sections of each indentation were then cut by FIB to produce indentation cross sectional TEM lamellae and the hardness, the irradiation hardening, and the deformation mechanisms were evaluated through the

analysis of the Load vs displacement profiles and TEM imaging. The following conclusions have been made:

- Indentation in both Fe-P and Fe-N along <001> produces a harder response than indentation along <011> which is the result of higher Schmid factors and easier activation of slip systems along the <011> indentation direction.
- Fe-P is harder than Fe-N in all cases and is likely the result of martensitic phase transformation in the Fe-N alloy which acts to relieve stress
- Greater irradiation hardening is demonstrated in the Fe-P alloy than in the Fe-N by unirradiated – irradiated hardness differences and by plastic zone sizes of both irradiated alloys.
- The greater irradiation hardening in the Fe-P in comparison to the Fe-N alloy is the result of significantly higher defect density in the irradiated Fe-P alloy and is verified by close agreement between hardness results and dispersed barrier model
- Cross slip demonstrated in <001> indented Fe-P may be the result of many slip systems with similar Schmid factors in the <001> indentation direction.
- More cross slip is demonstrated in Fe-P than in Fe-N which may be due to the high stacking fault energy in Fe-P and low stacking fault energy in Fe-N.
- Stress induced HCP martensitic phase transformation is demonstrated in Fe – N and may be the result of stacking fault stabilization by N interstitials.
- Stress induced HCP martensitic phase transformation is prevented in the irradiated zone of the irradiated Fe – N alloy and may be due to defect pinning, amorphization, or stacking fault destabilization.

REFERENCES

[1] W.Y. Chen, Y. Miao, J. Gan, M.A. Okuniewski, S.A. Maloy, J.F. Stubbins, Neutron irradiation effects in Fe and Fe-Cr at 300 °c, Acta Mater. 111 (2016). https://doi.org/10.1016/j.actamat.2016.03.060.

[2] S.J. Zinkle, G.S. Was, Materials challenges in nuclear energy, Acta Mater. 61 (2013). https://doi.org/10.1016/j.actamat.2012.11.004.

[3] P.D. Edmondson, S.A. Briggs, Y. Yamamoto, R.H. Howard, K. Sridharan, K.A. Terrani, K.G. Field, Irradiation-enhanced α′ precipitation in model FeCrAl alloys, Scr Mater. 116 (2016). https://doi.org/10.1016/j.scriptamat.2016.02.002.

[4] U. DoE, A technology roadmap for generation IV nuclear energy systems, Nuclear Energy Research Advisory Committee and the …. (2002).

[5] Z. Yao, M. Hernandez-Mayoral, M.L. Jenkins, M.A. Kirk, Heavy-ion irradiations of Fe and Fe-Cr model alloys Part 1: Damage evolution in thin-foils at lower doses, Philosophical Magazine. 88 (2008). https://doi.org/10.1080/14786430802380469.

[6] T. Lechtenberg, Irradiation effects in ferritic steels, Journal of Nuclear Materials. 133–134 (1985). https://doi.org/10.1016/0022-3115(85)90125-4.

[7] G.S. Was, Fundamentals of radiation materials science: Metals and alloys, second edition, 2016. https://doi.org/10.1007/978-1-4939-3438-6.

[8] G.R. Odette, G.E. Lucas, Recent progress in understanding reactor pressure vessel steel embrittlement, Radiation Effects and Defects in Solids. 144 (1998). https://doi.org/10.1080/10420159808229676.

[9] X. Xiao, Fundamental mechanisms for irradiation-hardening and embrittlement: A review, Metals (Basel). 9 (2019). https://doi.org/10.3390/met9101132.

[10] L.E. Rehn, P.R. Okamoto, D.I. Potter, H. Wiedersich, Effect of solute misfit and temperature on irradiation-induced segregation in binary Ni alloys, Journal of Nuclear Materials. 74 (1978). https://doi.org/10.1016/0022-3115(78)90363-X.

[11] N.Q. Lam, P.R. Okamoto, H. Wiedersich, Effects of solute segregation and precipitation on void swelling in irradiated alloys, Journal of Nuclear Materials. 74 (1978). https://doi.org/10.1016/0022-3115(78)90538-X.

[12] Z. Jiao, G.S. Was, Novel features of radiation-induced segregation and radiation-induced precipitation in austenitic stainless steels, Acta Mater. 59 (2011). https://doi.org/10.1016/j.actamat.2010.10.055.

[13] G.S. Was, J.P. Wharry, B. Frisbie, B.D. Wirth, D. Morgan, J.D. Tucker, T.R. Allen, Assessment of radiation-induced segregation mechanisms in austenitic and ferritic-martensitic alloys, Journal of Nuclear Materials. 411 (2011). https://doi.org/10.1016/j.jnucmat.2011.01.031.

[14] L. Steele, Chapter 8–Review and Analysis of Reactor Vessel Surveillance Programs, in: Status of USA Nuclear Reactor Pressure Vessel Surveillance for Radiation Effects, 2009. https://doi.org/10.1520/stp29426s.

[15] A. Kimura, R. Kasada, A. Kohyama, H. Tanigawa, T. Hirose, K. Shiba, S. Jitsukawa, S. Ohtsuka, S. Ukai, M.A. Sokolov, R.L. Klueh, T. Yamamoto, G.R. Odette, Recent progress in US-Japan collaborative research on ferritic steels R&D, Journal of Nuclear Materials. 367-370 A (2007). https://doi.org/10.1016/j.jnucmat.2007.03.013.

[16] A. Bhattacharya, E. Meslin, J. Henry, A. Barbu, S. Poissonnet, B. Décamps, Effect of chromium on void swelling in ion irradiated high purity Fe-Cr alloys, Acta Mater. 108 (2016). https://doi.org/10.1016/j.actamat.2016.02.027.

[17] M. Lambrecht, L. Malerba, Positron annihilation spectroscopy on binary Fe-Cr alloys and ferritic/martensitic steels after neutron irradiation, Acta Mater. 59 (2011). https://doi.org/10.1016/j.actamat.2011.06.046.

[18] I. Charit, C.S. Seok, K.L. Murty, Synergistic effects of interstitial impurities and radiation defects on mechanical characteristics of ferritic steels, Journal of Nuclear Materials. 361 (2007). https://doi.org/10.1016/j.jnucmat.2006.12.003.

[19] E.A. Little, D.R. Harries, Radiation-Hardening and Recovery in Mild Steels and the Effects of Interstitial Nitrogen, Metal Science Journal. 4 (1970) 188–195. https://doi.org/10.1179/msc.1970.4.1.188.

[20] C.J. Rietema, M.R. Chancey, S.K. Ullrich, C.B. Finfrock, D.V. Marshall, B.P. Eftink, Y.Q. Wang, G.R. Bourne, S.A. Maloy, A.J. Clarke, K.D. Clarke, The influence of nitrogen and nitrides on the structure and properties of proton irradiated ferritic/martensitic steel, Journal of Nuclear Materials. 561 (2022). https://doi.org/10.1016/j.jnucmat.2022.153528.

[21] E. Aydogan, J. Gigax, S. Parker, B.P. Eftink, M. Chancey, J.D. Poplawsky, S. Maloy, Nitrogen effects on radiation response in 12Cr ferritic/martensitic alloys, Scr Mater. 189 (2020).

[22] H. Kim, J.G. Gigax, C.J. Rietema, O. el Atwani, M.R. Chancey, J.K. Baldwin, Y. Wang, S.A. Maloy, Void swelling of conventional and composition engineered HT9 alloys after high-dose self-ion irradiation, Journal of Nuclear Materials. 560 (2022) 153492. https://doi.org/10.1016/j.jnucmat.2021.153492.

[23] Y. Katoh, A. Kohyama, The influence of impurity trapping on formation and growth of defect clusters in irradiated materials, Nuclear Inst. and Methods in Physics Research, B. 102 (1995). https://doi.org/10.1016/0168-583X(95)80109-Y.

[24] H. Watanabe, A. Aoki, H. Murakami, T. Muroga, N. Yoshida, Effects of phosphorus on defect behavior, solute segregation and void swelling in electron irradiated FeCrNi alloys, Journal of Nuclear Materials. 155–157 (1988). https://doi.org/10.1016/0022-3115(88)90422-9.

[25] E.H. Lee, L.K. Mansur, A.F. Rowcliffe, The effect of phosphorus on the swelling and precipitation behavior of austenitic stainless steels during irradiation, Journal of Nuclear Materials. 122 (1984). https://doi.org/10.1016/0022-3115(84)90614-7.

[26] M.A. Stopher, The effects of neutron radiation on nickel-based alloys, Materials Science and Technology (United Kingdom). 33 (2017). https://doi.org/10.1080/02670836.2016.1187334.

[27] Y. Satoh, T. Yoshiie, S. Arai, Undersize solute element effects on defect structure development in copper under electron irradiation, Philosophical Magazine. 98 (2018). https://doi.org/10.1080/14786435.2017.1414326.

[28] Hysitron Nanoindenters, (2022). https://www.bruker.com/en/products-and-solutions/test-and-measurement/nanomechanical-test-systems/hysitron-nanoindenters.html.

[29] M. Saleh, A. Xu, C. Hurt, M. Ionescu, J. Daniels, P. Munroe, L. Edwards, D. Bhattacharyya, Oblique cross-section nanoindentation for determining the hardness change in ion-irradiated steel, Int J Plast. 112 (2019). https://doi.org/10.1016/j.ijplas.2018.08.015.

[30] T. Scholz, K.K. McLaughlin, F. Giuliani, W.J. Clegg, F.J. Espinoza-Beltrán, M. v Swain, G.A. Schneider, Nanoindentation initiated dislocations in barium titanate (Ba Ti O 3), Appl Phys Lett. 91 (2007) 062903-062903–3. https://doi.org/10.1063/1.2766846.

[31] G.W. Egeland, J.A. Valdez, S.A. Maloy, K.J. McClellan, K.E. Sickafus, G.M. Bond, Heavy-ion irradiation defect accumulation in ZrN characterized by TEM, GIXRD, nanoindentation, and helium desorption, Journal of Nuclear Materials. 435 (2013). https://doi.org/10.1016/j.jnucmat.2012.12.025.

[32] Matt Besser, MPC Service Agreement - Terms and Conditions, Ames, IA, 2018. www.mpc.ameslab.gov (accessed August 15, 2022).

[33] K.-O. Yu, Modeling for Casting and Solidification Processing, First edition., CRC Press, Boca Raton, FL, 2001. https://doi.org/10.1201/9781482277333.

[34] E.C. Jameson, Electrical discharge machining : tooling, methods, and applications, 1st ed., Society of Manufacturing Engineers, Marketing Services Division, Dearborn, Mich, 1983.

[35] K.A. Cashell, N.R. Baddoo, Ferritic stainless steels in structural applications, Thin-Walled Structures. 83 (2014) 169–181. https://doi.org/10.1016/J.TWS.2014.03.014.

[36] H. Kayano, A. Kimura, M. Narui, Y. Sasaki, Y. Suzuki, S. Ohta, Irradiation embrittlement of neutron-irradiated low activation ferritic steels, Journal of Nuclear Materials. 155–157 (1988) 978–981. https://doi.org/10.1016/0022-3115(88)90452-7.

[37] M.O.H. Amuda, E.T. Akinlabi, S. Mridha, Ferritic Stainless Steels: Metallurgy, Application and Weldability, Reference Module in Materials Science and Materials Engineering. (2016). https://doi.org/10.1016/B978-0-12-803581-8.04010-8.

[38] T. Misawa, T. Adachi, M. Saito, Y. Hamaguchi, Small punch tests for evaluating ductile-brittle transition behavior of irradiated ferritic steels, Journal of Nuclear Materials. 150 (1987) 194–202. https://doi.org/10.1016/0022-3115(87)90075-4.

[39] L. Tan, L.L. Snead, Y. Katoh, Development of new generation reduced activation ferritic-martensitic steels for advanced fusion reactors, Journal of Nuclear Materials. 478 (2016) 42–49. https://doi.org/10.1016/J.JNUCMAT.2016.05.037.

[40] H.R. Abbasi, M. Bazdar, A. Halvaee, Effect of phosphorus as an alloying element on microstructure and mechanical properties of pearlitic gray cast iron, Mater Sci Eng A Struct Mater. 444 (2007) 314–317. https://doi.org/10.1016/j.msea.2006.08.108.

[41] G.L. Krasko, G.B. Olson, Effect of boron, carbon, phosphorus and sulphur on intergranular cohesion in iron, Solid State Commun. 76 (1990) 247–251. https://doi.org/10.1016/0038-1098(90)90832-V.

[42] R. Wu, A.J. Freeman, G.B. Olson, First Principles Determination of the Effects of Phosphorus and Boron on Iron Grain Boundary Cohesion, Science (American Association for the Advancement of Science). 265 (1994) 376–380. https://doi.org/10.1126/science.265.5170.376.

[43] E. Wachowicz, A. Kiejna, Effect of impurities on grain boundary cohesion in bcc iron, Comput Mater Sci. 43 (2008) 736–743. https://doi.org/10.1016/J.COMMATSCI.2008.01.063.

[44] W.-S. Ko, N.J. Kim, B.-J. Lee, Atomistic modeling of an impurity element and a metal-impurity system: pure P and Fe-P system, Journal of Physics. Condensed Matter. 24 (2012) 225002–225002. https://doi.org/10.1088/0953-8984/24/22/225002.

[45] A. Akhatova, F. Christien, V. Barnier, B. Radiguet, E. Cadel, F. Cuvilly, P. Pareige, Investigation of the dependence of phosphorus segregation on grain boundary structure in Fe-P-C alloy: cross comparison between Atom Probe Tomography and Auger Electron Spectroscopy, Appl Surf Sci. 463 (2019) 203–210. https://doi.org/10.1016/j.apsusc.2018.08.085.

[46] W. Liu, C. Ren, H. Han, J. Tan, Y. Zou, X. Zhou, P. Huai, H. Xu, First-principles study of the effect of phosphorus on nickel grain boundary, J Appl Phys. 115 (2014) 043706. https://doi.org/10.1063/1.4863181.

[47] P.J. Maziasz, Formation and stability of radiation-induced phases in neutron-irradiated austenitic and ferritic steels, Journal of Nuclear Materials. 169 (1989) 95–115. https://doi.org/10.1016/0022-3115(89)90525-4.

[48] Z. Liu, Y. Kobayashi, M. Kuwabara, K. Nagai, Interaction between Phosphorus Micro-Segregation and Sulfide Precipitation in Rapidly Solidified Steel—Utilization of Impurity Elements in Scrap Steel, Mater Trans. 48 (2007) 3079–3087. https://doi.org/10.2320/matertrans.MK200704.

[49] Z. Liu, Y. Kobayashi, K. Nagai, Effect of Phosphorus on Sulfide Precipitation in Strip Casting Low Carbon Steel, Mater Trans. 46 (2005) 26–33. https://doi.org/10.2320/matertrans.46.26.

[50] E.H. Lee, L.K. Mansur, A mechanism of swelling suppression in phosphorous-modified Fe-Ni-Cr alloys, Journal of Nuclear Materials. 141–143 (1986) 695–702. https://doi.org/10.1016/0022-3115(86)90076-0.

[51] Y. Guo, K. Wang, S. Song, Abnormal influence of impurity element phosphorus on the hot ductility of SA508Gr.4N reactor pressure vessel steel, Mater Sci Eng A Struct Mater. 792 (2020) 139837. https://doi.org/10.1016/j.msea.2020.139837.

[52] Y. Nishiyama, T.E. Bloomer, J. Kameda, Effect of Bulk Phosphorus Content on Hardening, Non-Equilibrium Segregation and Embrittlement in Neutron Irradiated Iron-Based Alloys, MRS Proceedings. 650 (2000). https://doi.org/10.1557/PROC-650-R6.10.

[53] K.J. Harrelson, S.H. Rou, R.C. Wilcox, Impurity element effects on the toughness of 9Cr-1Mo steel, Journal of Nuclear Materials. 141 (1986) 508–512. https://doi.org/10.1016/S0022-3115(86)80091-5.

[54] O.K. von Goldbeck, IRON—Binary Phase Diagrams, 1982. https://doi.org/10.1007/978-3-662-08024-5.

[55] C. Domain, C.S. Becquart, Diffusion of phosphorus in α-Fe: An ab initio study, Phys Rev B Condens Matter Mater Phys. 71 (2005). https://doi.org/10.1103/PhysRevB.71.214109.

[56] Ab initio calculations of the lattice parameter and elastic stiffness coefficients of bcc Fe with solutes, United States. Office of the Assistant Secretary of Energy Efficiency and Renewable Energy, Washington, D.C, 2016.

[57] C. Pareige, V. Kuksenko, P. Pareige, Behaviour of P, Si, Ni impurities and Cr in self ion irradiated Fe-Cr alloys - Comparison to neutron irradiation, Journal of Nuclear Materials. 456 (2015). https://doi.org/10.1016/j.jnucmat.2014.10.024.

[58] B. Egert, G. Panzner, Electron spectroscopic study of phosphorus segregated to α-iron surfaces, Surf Sci. 118 (1982) 345–368. https://doi.org/10.1016/0039-6028(82)90034-6.

[59] V.G. Gavriljuk, Nitrogen in Iron and Steel, ISIJ International. 36 (1996) 738–745. https://doi.org/10.2355/isijinternational.36.738.

[60] R. Ritzenhoff, Corrosion Resistance of High Nitrogen Steels, IntechOpen, s.l, 2012.

[61] Factors Affecting Radiation Damage of Steels, Materials Science Monographs. 79 (1994) 66–120. https://doi.org/10.1016/B978-0-444-98708-2.50008-8.

[62] T.H. Ahn, S.B. Lee, K.T. Park, K.H. Oh, H.N. Han, Strain-induced ε-martensite transformation during nanoindentation of high-nitrogen steel, Materials Science and Engineering: A. 598 (2014) 56–61. https://doi.org/10.1016/J.MSEA.2014.01.030.

[63] H.W. King, Quantitative size-factors for interstitial solid solutions, J Mater Sci. 6 (1971). https://doi.org/10.1007/BF00550085.

[64] M.A.J. Somers, R.M. Lankreijer, E.J. Mittemeijer, Excess Nitrogen in the Ferrite Matrix of Nitride Binary Iron-Based Alloys, Philosophical Magazine. A, Physics of Condensed Matter. Defects and Mechanical Properties. 59 (1989) 353–378.

[65] M.R. Fellinger, L.G. Hector, D.R. Trinkle, Ab initio calculations of the lattice parameter and elastic stiffness coefficients of bcc Fe with solutes, Comput Mater Sci. 126 (2017) 503–513. https://doi.org/10.1016/j.commatsci.2016.09.040.

[66] M.J. Konstantinović, W. van Renterghem, M. Matijašević, B. Minov, M. Lambrecht, T. Toyama, M. Chiapetto, L. Malerba, Mechanical and microstructural properties of neutron irradiated Fe-Cr-C alloys, Physica Status Solidi. A, Applications and Materials Science. 213 (2016) 2988–2994. https://doi.org/10.1002/pssa.201600316.

[67] A.-A.F. Tavassoli, E. Diegele, R. Lindau, N. Luzginova, H. Tanigawa, Current status and recent research achievements in ferritic/martensitic steels, Journal of Nuclear Materials. 455 (2014) 269–276. https://doi.org/10.1016/j.jnucmat.2014.06.017.

[68] L. Gardner, The use of stainless steel in structures, Progress in Structural Engineering and Materials. 7 (2005) 45–55. https://doi.org/10.1002/pse.190.

[69] W.D. Callister, Materials science and engineering : an introduction., 8th edition / Wil..., John Wiley & Sons, Hoboken, NJ, 2010.

[70] K. Ono, K. Arakawa, K. Hojou, Formation and migration of helium bubbles in Fe and Fe–9Cr ferritic alloy, Journal of Nuclear Materials. 307–311 (2002) 1507–1512. https://doi.org/10.1016/S0022-3115(02)01268-0.

[71] M. Matijasevic, A. Almazouzi, Effect of Cr on the mechanical properties and microstructure of Fe–Cr model alloys after n-irradiation, Journal of Nuclear Materials. 377 (2008) 147–154. https://doi.org/10.1016/j.jnucmat.2008.02.061.

[72] M. Sarikaya, B.G. Steinberg, G. Thomas, Optimization of Fe/Cr/C base structural Steels for improved strength and toughness, Metall. Trans., A; (United States). 13 (1982) 2227–2237. https://doi.org/10.1007/BF02648394.

[73] T. Fujita, Current Progress in Advanced High Cr Ferritic Steels for High-temperature Applications, ISIJ International. 32 (1992) 175–181. https://doi.org/10.2355/isijinternational.32.175.

[74] N.R. Baddoo, Stainless steel in construction: A review of research, applications, challenges and opportunities, J Constr Steel Res. 64 (2008) 1199–1206. https://doi.org/10.1016/j.jcsr.2008.07.011.

[75] C.D. Hardie, C.A. Williams, S. Xu, S.G. Roberts, Effects of irradiation temperature and dose rate on the mechanical properties of self-ion implanted Fe and Fe–Cr alloys, Journal of Nuclear Materials. 439 (2013) 33–40. https://doi.org/10.1016/j.jnucmat.2013.03.052.

[76] C.R. de Farias Azevedo, H. Boschetti Pereira, S. Wolynec, A.F. Padilha, An overview of the recurrent failures of duplex stainless steels, Eng Fail Anal. 97 (2019) 161–188. https://doi.org/10.1016/J.ENGFAILANAL.2018.12.009.

[77] Y. Zhao, A. Bhattacharya, C. Pareige, C. Massey, P. Zhu, J.D. Poplawsky, J. Henry, S.J. Zinkle, Effect of heavy ion irradiation dose rate and temperature on α′ precipitation in high purity Fe-18%Cr alloy, Acta Mater. 231 (2022) 117888. https://doi.org/10.1016/j.actamat.2022.117888.

[78] H.W. King, Quantitative size-factors for metallic solid solutions, J Mater Sci. 1 (1966). https://doi.org/10.1007/BF00549722.

[79] P. Olsson, C. Domain, J. Wallenius, Ab initio study of Cr interactions with point defects in bcc Fe, Phys Rev B Condens Matter Mater Phys. 75 (2007) 014110. https://doi.org/10.1103/PhysRevB.75.014110.

[80] S. Djaziri, Y. Li, G.A. Nematollahi, B. Grabowski, S. Goto, C. Kirchlechner, A. Kostka, S. Doyle, J. Neugebauer, D. Raabe, G. Dehm, Deformation-Induced Martensite: A New Paradigm for Exceptional Steels, Advanced Materials. 28 (2016). https://doi.org/10.1002/adma.201601526.

[81] J.F. Ziegler, M.D. Ziegler, J.P. Biersack, SRIM – The stopping and range of ions in matter (2010), Nucl Instrum Methods Phys Res B. 268 (2010) 1818–1823. https://doi.org/10.1016/j.nimb.2010.02.091.

[82] T. Hashimoto, N. Shigenaka, A theory of dislocation loop formation in binary alloys under irradiation, Journal of Nuclear Materials. 187 (1992). https://doi.org/10.1016/0022-3115(92)90548-Y.

[83] W.B. (William B. Pearson, A handbook of lattice spacings and structures of metals and alloys., Pergamon Press, New York, 1958.

[84] A. Bakaev, D. Terentyev, G. Bonny, T.P.C. Klaver, P. Olsson, D. van Neck, Interaction of minor alloying elements of high-Cr ferritic steels with lattice defects: An ab initio study, Journal of Nuclear Materials. 444 (2014) 237–246. https://doi.org/10.1016/j.jnucmat.2013.09.053.

[85] Y. Zhang, S. Zhao, W.J. Weber, K. Nordlund, F. Granberg, F. Djurabekova, Atomic-level heterogeneity and defect dynamics in concentrated solid-solution alloys, Curr Opin Solid State Mater Sci. 21 (2017) 221–237. https://doi.org/10.1016/J.COSSMS.2017.02.002.

[86] T. ni Yang, C. Lu, G. Velisa, K. Jin, P. Xiu, M.L. Crespillo, Y. Zhang, H. Bei, L. Wang, Effect of alloying elements on defect evolution in Ni-20X binary alloys, Acta Mater. 151 (2018) 159–168. https://doi.org/10.1016/J.ACTAMAT.2018.03.054.

[87] A.A. Vasiliev, V. v. Rybin, A.A. Zisman, The nature of the phosphorus atom mobility in bcc iron irradiated at low temperatures, Journal of Nuclear Materials. 231 (1996). https://doi.org/10.1016/0022-3115(96)00201-2.

[88] H. Watanabe, A. Aoki, H. Murakami, T. Muroga, N. Yoshida, Effects of phosphorus on defect behavior, solute segregation and void swelling in electron irradiated Fe-Cr-Ni alloys, Journal of Nuclear Materials. 155–157 (1988) 815–822. https://doi.org/10.1016/0022-3115(88)90422-9.

[89] D. Terentyev, Study of radiation effects in FeCr alloys for fusion applications using computer simulations, Phd Thesis. (2006).

[90] D. Terentyev, P. Olsson, L. Malerba, A.V. Barashev, Characterization of dislocation loops and chromium-rich precipitates in ferritic iron–chromium alloys as means of void swelling suppression, Journal of Nuclear Materials. 362 (2007) 167–173. https://doi.org/10.1016/j.jnucmat.2007.01.069.

[91] C.S. Becquart, R. Ngayam Happy, P. Olsson, C. Domain, A DFT study of the stability of SIAs and small SIA clusters in the vicinity of solute atoms in Fe, Journal of Nuclear Materials. 500 (2018) 92–109. https://doi.org/10.1016/J.JNUCMAT.2017.12.022.

[92] H. Wiedersich, P.R. Okamoto, N.Q. Lam, A theory of radiation-induced segregation in concentrated alloys, Journal of Nuclear Materials. 83 (1979) 98–108. https://doi.org/10.1016/0022-3115(79)90596-8.

[93] G.E. Dieter, Mechanical metallurgy, 3rd ed., McGraw-Hill, New York, 1986.

[94] J.W. Christian, Some surprising features of the plastic deformation of body-centered cubic metals and alloys, Metallurgical Transactions A. 14 (1983). https://doi.org/10.1007/BF02664806.

[95] F. Kroupa, V. Vítek, Splitting of dislocations in b.c.c. metals on {110} planes, Czechoslovak Journal of Physics. 14 (1964) 337–346. https://doi.org/10.1007/BF01689142.

[96] G.B. Olson, M. Cohen, A general mechanism of martensitic nucleation: Part II. FCC → BCC and other martensitic transformations, Metallurgical Transactions A. 7 (1976) 1905–1914. https://doi.org/10.1007/BF02659823.

[97] S.J. Wang, M.L. Sui, Y.T. Chen, Q.H. Lu, E. Ma, X.Y. Pei, Q.Z. Li, H.B. Hu, Microstructural fingerprints of phase transitions in shock-loaded iron, Sci Rep. 3 (2013) 1086–1086. https://doi.org/10.1038/srep01086.

[98] L.M. Barker, R.E. Hollenbach, Shock wave study of the α ⇄ ε phase transition in iron, J Appl Phys. 45 (1974) 4872–4887. https://doi.org/10.1063/1.1663148.

[99] K.J. Caspersen, A. Lew, M. Ortiz, E.A. Carter, Importance of shear in the bcc-to-hcp transformation in iron, Phys Rev Lett. 93 (2004). https://doi.org/10.1103/PhysRevLett.93.115501.

[100] Y. Matsukawa, I. Okuma, H. Muta, Y. Shinohara, R. Suzue, H.L. Yang, T. Maruyama, T. Toyama, J.J. Shen, Y.F. Li, Y. Satoh, S. Yamanaka, H. Abe, Crystallographic analysis on atomic-plane parallelisms between bcc precipitates and hcp matrix in recrystallized Zr-2.5Nb alloys, Acta Mater. 126 (2017) 86–101. https://doi.org/10.1016/j.actamat.2016.12.053.

[101] M. Rhee, H.M. Zbib, J.P. Hirth, H. Huang, T. de la Rubia, Models for long-/short-range interactions and cross slip in 3D dislocation simulation of BCC single crystals, Model Simul Mat Sci Eng. 6 (1998) 467–492. https://doi.org/10.1088/0965-0393/6/4/012.

[102] C.M. van der Walt, Slip in the B.C.C. metals, Acta Metallurgica. 17 (1969) 393–395. https://doi.org/10.1016/0001-6160(69)90019-4.

[103] P.J. Jackson, The role of cross-slip in the plastic deformation of crystals, Materials Science and Engineering. 57 (1983) 39–47. https://doi.org/10.1016/0025-5416(83)90025-3.

[104] M.J. Swenson, C.K. Dolph, J.P. Wharry, The effects of oxide evolution on mechanical properties in proton- and neutron-irradiated Fe-9%Cr ODS steel, Journal of Nuclear Materials. 479 (2016). https://doi.org/10.1016/j.jnucmat.2016.07.022.

[105] G.E. Lucas, The evolution of mechanical property change in irradiated austenitic stainless steels, Journal of Nuclear Materials. 206 (1993) 287–305. https://doi.org/10.1016/0022-3115(93)90129-M.

[106] W.C. Oliver, G.M. Pharr, An improved technique for determining hardness and elastic modulus using load and displacement sensing indentation experiments, J Mater Res. 7 (1992) 1564–1583. https://doi.org/10.1557/JMR.1992.1564.

[107] A.C. Fischer-Cripps, Nanoindentation, 1st ed. 2002., Springer New York, New York, NY, 2002. https://doi.org/10.1007/978-0-387-22462-6.

[108] E. Getto, B. Tobie, E. Bautista, A.L. Bullens, Z.T. Kroll, M.J. Pavel, K.S. Mao, D.W. Gandy, J.P. Wharry, Thermal Aging and the Hall–Petch Relationship of PM-HIP and Wrought Alloy 625, JOM (1989). 71 (2019) 2837–2845. https://doi.org/10.1007/s11837-019-03532-6.

[109] R. Kasada, Y. Takayama, K. Yabuuchi, A. Kimura, A new approach to evaluate irradiation hardening of ion-irradiated ferritic alloys by nano-indentation techniques, Fusion Engineering and Design. 86 (2011) 2658–2661. https://doi.org/10.1016/J.FUSENGDES.2011.03.073.

[110] M. Saleh, Z. Zaidi, M. Ionescu, C. Hurt, K. Short, J. Daniels, P. Munroe, L. Edwards, D. Bhattacharyya, Relationship between damage and hardness profiles in ion irradiated SS316 using nanoindentation – Experiments and modelling, Int J Plast. 86 (2016) 151–169. https://doi.org/10.1016/j.ijplas.2016.08.006.

[111] K.H. Yano, IN SITU TEM MECHANICAL TESTING OF IRRADIATED OXIDE DISPERSION STRENGTHENED ALLOYS, Purdue University Graduate School, 2019. /articles/thesis/In_Situ_TEM_Mechanical_Testing_of_Irradiated_Oxide_Dispersion_Strengthened_Alloys/8041817/1.

[112] M. Monavari, M. Zaiser, Annihilation and sources in continuum dislocation dynamics, Materials Theory. 2 (2018) 1–30. https://doi.org/10.1186/s41313-018-0010-z.

[113] Application of STEM characterization for investigating radiation effects in BCC Fe-based alloys, United States. Dept. of Energy. Office of Science, Washington, D.C, 2015.

[114] David. Brandon, Microstructural Characterization of Materials, 2nd ed., Wiley, Hoboken, 2008.

[115] H.S. Nalwa, Handbook of Surfaces and Interfaces of Materials, Five-Volume Set, Elsevier Science & Technology, Saint Louis, 2001.

[116] R. Kasada, Y. Takayama, K. Yabuuchi, A. Kimura, A new approach to evaluate irradiation hardening of ion-irradiated ferritic alloys by nano-indentation techniques, Fusion Engineering and Design. 86 (2011) 2658–2661. https://doi.org/10.1016/J.FUSENGDES.2011.03.073.

[117] M.S. Duesbery, V. Vitek, Plastic anisotropy in b.c.c. transition metals, Acta Mater. 46 (1998) 1481–1492. https://doi.org/10.1016/S1359-6454(97)00367-4.

[118] C.K. Dolph, D.J. da Silva, M.J. Swenson, J.P. Wharry, Plastic zone size for nanoindentation of irradiated Fe–9%Cr ODS, Journal of Nuclear Materials. 481 (2016) 33–45. https://doi.org/10.1016/j.jnucmat.2016.08.033.

[119] H.E. Karaca, I. Karaman, D.C. Lagoudas, H.J. Maier, Y.I. Chumlyakov, Recoverable stress-induced martensitic transformation in a ferromagnetic CoNiAl alloy, Scr Mater. 49 (2003) 831–836. https://doi.org/10.1016/S1359-6462(03)00470-6.

[120] C. Celada-Casero, H. Kooiker, M. Groen, J. Post, D. San-Martin, In-Situ Investigation of Strain-Induced Martensitic Transformation Kinetics in an Austenitic Stainless Steel by Inductive Measurements, Metals (Basel). 7 (2017) 271. https://doi.org/10.3390/met7070271.

[121] C. Caër, E. Patoor, S. Berbenni, J.S. Lecomte, Stress induced pop-in and pop-out nanoindentation events in CuAlBe shape memory alloys, Materials Science and Engineering: A. 587 (2013) 304–312. https://doi.org/10.1016/J.MSEA.2013.08.052.

[122] V. Domnich, Y. Gogotsi, Phase transformations in silicon under contact loading, Reviews on Advanced Materials Science. 3 (2002) 1–36.

[123] E. Meslin, C.-C. Fu, A. Barbu, F. Gao, F. Willaime, Theoretical study of atomic transport via interstitials in dilute Fe − P alloys, Phys Rev B Condens Matter Mater Phys. 75 (2007). https://doi.org/10.1103/PhysRevB.75.094303.

[124] C. Domain, C.S. Becquart, Ab initio calculations of defects in Fe and dilute Fe-Cu alloys, Phys Rev B Condens Matter. 65 (2001). https://doi.org/10.1103/PhysRevB.65.024103.

[125] K. Fukuya, S. Nakahigashi, S. Ozaki, S. Shima, Effects of phosphorus, silicon and sulphur on microstructural evolution in austenitic stainless steels during electron irradiation, Journal of Nuclear Materials. 179 (1991) 1057–1060. https://doi.org/10.1016/0022-3115(91)90274-B.

[126] E.A. Little, D.R. Harries, The Correlation of Radiation-Hardening with Interstitial Nitrogen Content in Mild Steels, Metal Science Journal. 4 (1970) 195–200. https://doi.org/10.1179/msc.1970.4.1.195.

[127] C. Domain, C.S. Becquart, J. Foct, Ab initio study of foreign interstitial atom (C, N) interactions with intrinsic point defects in α -Fe, Phys Rev B Condens Matter Mater Phys. 69 (2004). https://doi.org/10.1103/PhysRevB.69.144112.

[128] T. Hamaoka, Y. Satoh, H. Matsui, One-dimensional motion of interstitial clusters in iron-based binary alloys observed using a high-voltage electron microscope, Journal of Nuclear Materials. 433 (2013). https://doi.org/10.1016/j.jnucmat.2012.09.007.

[129] Y. Satoh, T. Yoshiie, I. Ishida, M. Kiritani, Defect structure development in electron-irradiated Cu-based Si, Ge and Sn binary alloys, Philosophical Magazine. A, Physics of Condensed Matter. Defects and Mechanical Properties. 80 (2000) 2567–2590. https://doi.org/10.1080/01418610008216493.

[130] P. Xiu, Y.N. Osetsky, L. Jiang, G. Velisa, Y. Tong, H. Bei, W.J. Weber, Y. Zhang, L. Wang, Dislocation loop evolution and radiation hardening in nickel-based concentrated solid solution alloys, Journal of Nuclear Materials. 538 (2020). https://doi.org/10.1016/j.jnucmat.2020.152247.

[131] Y. Abe, T. Suzudo, S. Jitsukawa, T. Tsuru, T. Tsukada, Effects of Carbon Impurity on Microstructural Evolution in Irradiated α-Iron, Fusion Science and Technology. 62 (2012) 139–144. https://doi.org/10.13182/FST12-A14126.

[132] V. JANSSON, M. CHIAPETTO, L. MALERBA, The nanostructure evolution in Fe-C systems under irradiation at 560 K, Journal of Nuclear Materials. 442 (2013) 341–349. https://doi.org/10.1016/j.jnucmat.2013.09.017.

[133] H. Watanabe, A. Hiragane, S. Shin, N. Yoshida, Y. Kamada, Effect of stress on radiation-induced hardening of A533B and Fe-Mn model alloys, Journal of Nuclear Materials. 442 (2013). https://doi.org/10.1016/j.jnucmat.2013.04.029.

[134] P.R. Okamoto, L.E. Rehn, Radiation-induced segregation in binary and ternary alloys, Journal of Nuclear Materials. 83 (1979) 2–23. https://doi.org/10.1016/0022-3115(79)90587-7.

[135] J.C. Han, J.B. Seol, M. Jafari, J.E. Kim, S.J. Seo, C.G. Park, Competitive grain boundary segregation of phosphorus and carbon governs delamination crack in a ferritic steel, Mater Charact. 145 (2018) 454–460. https://doi.org/10.1016/J.MATCHAR.2018.08.060.

[136] Z. Lu, R.G. Faulkner, P.E.J. Flewitt, The role of irradiation-induced phosphorus segregation in the ductile-to-brittle transition temperature in ferritic steels, Materials Science and Engineering: A. 437 (2006) 306–312. https://doi.org/10.1016/J.MSEA.2006.07.114.

[137] S.K. Ray, S. Mishra, O.N. Mohanty, TEM study of carbide precipitation in a phosphorus-bearing low-carbon steel, Scripta Metallurgica. 16 (1982) 43–47. https://doi.org/10.1016/0036-9748(82)90400-8.

[138] S.K. Ray, S. Mishra, O.N. Mohanty, Magnetic aging characteristics of a phosphorous-bearing low carbon steel, Scripta Metallurgica. 15 (1981) 971–973. https://doi.org/10.1016/0036-9748(81)90236-2.

[139] M. Bachhav, G. Robert Odette, E.A. Marquis, α′ precipitation in neutron-irradiated Fe–Cr alloys, Scr Mater. 74 (2014) 48–51. https://doi.org/10.1016/J.SCRIPTAMAT.2013.10.001.

[140] G. Bonny, D. Terentyev, L. Malerba, D. van Neck, Early stages of α − α ′ phase separation in Fe-Cr alloys: An atomistic study, Phys Rev B Condens Matter Mater Phys. 79 (2009). https://doi.org/10.1103/PhysRevB.79.104207.

[141] Q. Lu, W. Xu, S. van der Zwaag, Designing new corrosion resistant ferritic heat resistant steel based on optimal solid solution strengthening and minimisation of undesirable microstructural components, Comput Mater Sci. 84 (2014) 198–205. https://doi.org/10.1016/j.commatsci.2013.12.009.

[142] F.B. Pickering, Physical metallurgy and the design of steels, Applied Science Publishers, London, 1978.

[143] R.W. Cahn, P. Haasen, Physical metallurgy, 4th ed., North-Holland Pub. Co., Amsterdam, 1996.

[144] W.J. Dan, S.H. Li, W.G. Zhang, Z.Q. Lin, The effect of strain-induced martensitic transformation on mechanical properties of TRIP steel, Mater Des. 29 (2008) 604–612. https://doi.org/10.1016/J.MATDES.2007.02.019.

[145] R. Saha, W.D. Nix, Effects of the substrate on the determination of thin film mechanical properties by nanoindentation, Acta Mater. 50 (2002) 23–38. https://doi.org/10.1016/S1359-6454(01)00328-7.

[146] C. Heintze, F. Bergner, S. Akhmadaliev, E. Altstadt, Ion irradiation combined with nanoindentation as a screening test procedure for irradiation hardening, Journal of Nuclear Materials. 472 (2016) 196–205. https://doi.org/10.1016/J.JNUCMAT.2015.07.023.

[147] C. Yin, G. Bonny, D. Terentyev, Anisotropy in the hardness of single crystal tungsten before and after neutron irradiation, Journal of Nuclear Materials. 546 (2021) 152759. https://doi.org/10.1016/j.jnucmat.2020.152759.

[148] C.A. Brookes, J.B. O'Neill, B.A.W. Redfern, Anisotropy in the Hardness of Single Crystals, Proc R Soc Lond A Math Phys Sci. 322 (1971) 73–88. https://doi.org/10.1098/rspa.1971.0055.

[149] T. Khvan, L. Noels, D. Terentyev, F. Dencker, D. Stauffer, U.D. Hangen, W. van Renterghem, C. Cheng, A. Zinovev, High temperature nanoindentation of iron: Experimental and computational study, Journal of Nuclear Materials. 567 (2022) 153815. https://doi.org/10.1016/J.JNUCMAT.2022.153815.

[150] W.Z. Yao, J.H. You, Berkovich nanoindentation study of monocrystalline tungsten: a crystal plasticity study of surface pile-up deformation, Philos Mag (Abingdon). 97 (2017) 1418–1435. https://doi.org/10.1080/14786435.2017.1299237.

[151] S. Jakob, A. Leitner, A. Lorich, M. Eidenberger-Schober, W. Knabl, R. Pippan, H. Clemens, V. Maier-Kiener, Influence of crystal orientation and Berkovich tip rotation on the mechanical characterization of grain boundaries in molybdenum, Mater Des. 182 (2019) 107998. https://doi.org/10.1016/J.MATDES.2019.107998.

[152] Z. Wang, X. Shi, X.S. Yang, W. He, S.Q. Shi, X. Ma, Atomistic simulation of martensitic transformations induced by deformation of α-Fe single crystal during the mode-I fracture, J Mater Sci. 56 (2021). https://doi.org/10.1007/s10853-020-05401-z.

[153] R.E. Schramm, R.P. Reed, Stacking fault energies of seven commercial austenitic stainless steels, Metallurgical Transactions A. 6 (1975) 1345–1351. https://doi.org/10.1007/BF02641927.

[154] R.E. Stoltz, J.B. Sande, The effect of nitrogen on stacking fault energy of Fe-Ni-Cr-Mn steels, Metall. Trans., A; (United States). 11 (1980) 1033–1037. https://doi.org/10.1007/BF02654717.

[155] Y. Kawahara, R. Teranishi, C. Takushima, J. Hamada, K. Kaneko, Effect of Nitrogen Addition on the Stacking-Fault Energies in Si-added Austenitic Stainless Steel, Tetsu to hagane. 106 (2020) 816–825. https://doi.org/10.2355/tetsutohagane.TETSU-2020-021.

[156] J.P. Wharry, K.S. Mao, The role of irradiation on deformation-induced martensitic phase transformations in face-centered cubic alloys, J Mater Res. 35 (2020) 1660–1671. https://doi.org/10.1557/jmr.2020.80.

[157] I.A. Yakubtsov, A. Ariapour, D.D. Perovic, Effect of nitrogen on stacking fault energy of f.c.c. iron-based alloys, Acta Mater. 47 (1999) 1271–1279. https://doi.org/10.1016/S1359-6454(98)00419-4.

[158] T.-H. Lee, E. Shin, C.-S. Oh, H.-Y. Ha, S.-J. Kim, Correlation between stacking fault energy and deformation microstructure in high-interstitial-alloyed austenitic steels, Acta Mater. 58 (2010) 3173–3186. https://doi.org/10.1016/j.actamat.2010.01.056.

[159] P. Müllner, C. Solenthaler, P. Uggowitzer, M.O. Speidel, On the effect of nitrogen on the dislocation structure of austenitic stainless steel, Fundamental Aspects of Dislocation Interactions. (1993) 164–169. https://doi.org/10.1016/B978-1-4832-2815-0.50022-X.

[160] T.H. Ahn, C.S. Oh, D.H. Kim, K.H. Oh, H. Bei, E.P. George, H.N. Han, Investigation of strain-induced martensitic transformation in metastable austenite using nanoindentation, Scr Mater. 63 (2010) 540–543. https://doi.org/10.1016/J.SCRIPTAMAT.2010.05.024.

[161] X. Chen, S. Lu, Y. Zhao, T. Fu, C. Huang, X. Peng, Molecular dynamic simulation on nano-indentation of NiTi SMA, Materials Science and Engineering: A. 712 (2018) 592–602. https://doi.org/10.1016/J.MSEA.2017.11.030.

[162] J.Y. Lee, Y.M. Koo, S. Lu, L. Vitos, S.K. Kwon, The behaviour of stacking fault energy upon interstitial alloying, Sci Rep. 7 (2017). https://doi.org/10.1038/s41598-017-11328-4.

[163] P.J. Doyle, K.M. Benensky, S.J. Zinkle, Modeling of dislocation channel width evolution in irradiated metals, Journal of Nuclear Materials. 499 (2018) 47–64. https://doi.org/10.1016/J.JNUCMAT.2017.10.063.

[164] E. Asadi, M.A. Zaeem, A. Moitra, M.A. Tschopp, Effect of vacancy defects on generalized stacking fault energy of fcc metals, Journal of Physics. Condensed Matter. 26 (2014) 115404–115404. https://doi.org/10.1088/0953-8984/26/11/115404.

[165] K.S. Mao, C. Sun, C.-H. Shiau, K.H. Yano, P.D. Freyer, A.A. El-Azab, F.A. Garner, A. French, L. Shao, J.P. Wharry, Role of cavities on deformation-induced martensitic transformation pathways in a laser-welded, neutron irradiated austenitic stainless steel, Scr Mater. 178 (2020) 1–6. https://doi.org/10.1016/j.scriptamat.2019.10.037.

[166] R. Tewari, N.K. Sarkar, D. Harish, B. Vishwanadh, G.K. Dey, S. Banerjee, Intermetallics and Alloys for High Temperature Applications, Materials Under Extreme Conditions: Recent Trends and Future Prospects. (2017) 293–335. https://doi.org/10.1016/B978-0-12-801300-7.00009-7.

[167] C. Yang, J.P. Wharry, Role of point defects in stress-induced martensite transformations in NiTi shape memory alloys: A molecular dynamics study, Phys Rev B. 105 (2022). https://doi.org/10.1103/PhysRevB.105.144108.

[168] Y. Matsukawa, T. Suda, S. Ohnuki, C. Namba, Microstructure and mechanical properties of neutron irradiated TiNi shape memory alloy, Journal of Nuclear Materials. 271–272 (1999) 106–110. https://doi.org/10.1016/S0022-3115(98)00700-4.